POLYPUBLIE
Polytechnique Montréal

POLYTECHNIQUE MONTRÉAL
UNIVERSITÉ D'INGÉNIERIE

Titre: Title:	Development of a Multibody Model for Quantification of Muscle Forces at Upper Limb as a Design Tool for Exoskeleton Synthesis
Auteur: Author:	Guillaume Gaudet
Date:	2022
Type:	Mémoire ou thèse / Dissertation or Thesis
Référence: Citation:	Gaudet, G. (2022). Development of a Multibody Model for Quantification of Muscle Forces at Upper Limb as a Design Tool for Exoskeleton Synthesis [Thèse de doctorat, Polytechnique Montréal]. PolyPublie. https://publications.polymtl.ca/10569/

Document en libre accès dans PolyPublie
Open Access document in PolyPublie

URL de PolyPublie: PolyPublie URL:	https://publications.polymtl.ca/10569/
Directeurs de recherche: Advisors:	Maxime Raison, & Sofiane Achiche
Programme: Program:	PhD.

Ce fichier a été téléchargé à partir de PolyPublie, le dépôt institutionnel de Polytechnique Montréal
This file has been downloaded from PolyPublie, the institutional repository of Polytechnique Montréal

https://publications.polymtl.ca

POLYTECHNIQUE MONTRÉAL

affiliée à l'Université de Montréal

Development of a multibody model for the quantification of muscle forces at the upper limb as a design tool for exoskeleton synthesis

GUILLAUME GAUDET

Département de génie mécanique

Thèse présentée en vue de l'obtention du diplôme de *Philosophiæ Doctor*

Génie mécanique

Octobre 2022

© Guillaume Gaudet, 2022.

POLYTECHNIQUE MONTRÉAL

affiliée à l'Université de Montréal

Cette thèse intitulée :

Development of a multibody model for the quantification of muscle forces at the upper limb as a design tool for exoskeleton synthesis

Présentée par **Guillaume GAUDET**

en vue de l'obtention du diplôme de *Philosophiæ Doctor*

a été dûment acceptée par le jury d'examen constitué de :

David SAUSSIÉ, président
Maxime RAISON, membre et directeur de recherche
Sofiane ACHICHE, membre et codirecteur de recherche
Abolfazl MOHEBBI, membre
Ilmar Ferreira SANTOS, membre externe

ACKNOWLEDGEMENTS

I would like to thank my research directors, Pr. Maxime Raison, and Pr. Sofiane Achiche, for giving me the opportunity to work on this research project. I also thank them for their continuous support in the last 8+ years: first as a research intern, then as a master student, and, finally, as a Ph.D. student. In the last years, I lost the count how many times I considered quitting, but you always managed to motivate me through these rough patches to reach the finish line.

I would also like to thank all my colleagues and other students/interns with whom I have spent a lot of time during all these years at Polytechnique Montreal and Marie Enfant Rehabilitation Center. Thanks to everyone for all the enriching conversations on our respective projects and the great working atmosphere. A special thanks to my colleague and now friend Olivier, who has been an awesome support to help me finalize this Ph.D. through our countless conversations.

Finally, I keep my biggest thanks for my love and life partner, Vassilia. You have been by my side for the past 12 years, supporting me through all my studies at Polytechnique. My Ph.D. journey has been filled with ups and downs (mostly downs) and I could always feel your love, support, and encouragement to help me keep moving forward. I cannot wait to close this chapter and see what life has in store for us !

RÉSUMÉ

Les exosquelettes d'assistance sont considérés comme une solution prometteuse pour apporter un soutien continu aux personnes atteintes d'un diagnostic qui entrave les mouvements des bras. Cependant, la fonctionnalité, la sécurité et l'acceptation de ces dispositifs pourraient être améliorées par un dimensionnement basé sur l'anatomie et la physiologie de l'utilisateur. Dans ce contexte, l'objectif principal de cette recherche est de développer un outil de conception pour valider, par simulation, les performances d'un exosquelette basé sur la quantification des forces musculaires. L'outil développé est appliqué au mouvement de flexion-extension du coude (E.FE) comme cas de référence et réalisé en trois étapes.

Premièrement, un système multicorps musculosquelettique du membre supérieur a été développé. Pour ce faire, les quatre principaux muscles responsables de l'E.FE ont été intégrés à un modèle ostéoarticulaire existant. Les muscles ont été modélisés par une méthode de via-points. Le modèle proposé a ensuite été validé en comparant les longueurs musculo-tendineuses et les bras de levier musculaires avec les valeurs de référence de la littérature. L'erreur quadratique moyenne relative (rRMSE) pour les longueurs musculo-tendineuses était inférieure à 2.3 % pour tous les muscles. La rRMSE pour les bras de levier musculaires a atteint respectivement 14.5 % et 21.4 % pour le brachialis et le triceps brachii. Cette erreur élevée s'explique par l'absence d'objets enveloppants dans le modèle proposé et n'a été observée que lorsque le coude est entièrement fléchi ou en extension. Le rRMSE sur les bras de levier musculaires pour les autres muscles était inférieur à 7.0 %.

Deuxièmement, le modèle musculosquelettique nouvellement développé a été utilisé pour quantifier les forces musculaires avec une méthode non basée sur l'électromyographie. Cela a été fait avec trois fonctions coût différentes, à savoir Crowninshield, Forster et Wen, en formulant le processus d'optimisation comme un problème de contrôle optimal. Les forces musculaires quantifiées différaient en fonction de la fonction coût utilisée. La fonction coût de Crowninshield a donné lieu aux forces musculaires les plus faibles dans l'ensemble, tandis que celles de Forster et de Wen étaient plus élevées, car elles incluent toutes deux la co-contraction musculaire dans leur formulation. Le rRMSE entre le couple E.FE issu de la dynamique inverse et le couple E.FE calculé à partir des forces musculaires était inférieur à 5 % pour le mouvement E.FE. Le rRMSE était plus élevé pendant les tâches fonctionnelles mais restait inférieur à 10 %.

Troisièmement, un exosquelette a été intégré au modèle musculosquelettique pour valider ses performances par simulation. L'exosquelette était capable de compenser 80 % du couple E.FE de l'utilisateur produit par les muscles. Cependant, la réduction du couple articulaire ne s'est pas traduite par une réduction des forces musculaires réelles. En effet, les forces musculaires quantifiées ont montré une augmentation avec l'exosquelette. Cette augmentation des forces musculaires quantifiées se produit très probablement pour compenser les forces ou les couples parasites introduits par le désalignement de l'exosquelette au niveau de l'articulation du coude.

Pour conclure, cette recherche a introduit un nouveau modèle musculosquelettique du membre supérieur pour la quantification des forces musculaires qui peut être utilisé comme outil de validation pour la synthèse d'exosquelettes. Cette approche est importante car elle permet d'identifier rapidement les faiblesses de l'architecture d'un exosquelette. Les travaux futurs devraient se concentrer sur l'intégration des muscles de l'épaule et de l'avant-bras au modèle afin qu'il puisse être utilisé sur un plus large éventail de mouvements du membre supérieur et d'articulations de l'exosquelette.

ABSTRACT

Assistive exoskeletons are emerging as a promising solution to provide continuous support for people affected by a diagnosis that impairs arm movements. However, functionality, safety and acceptance of these devices could be improved with a sizing based on the user's anatomy and physiology. In this context, the main objective of this research is to develop a design tool to validate, through simulation, the performance of an exoskeleton based on the quantification of muscle forces. The developed tool is applied to the movement of elbow flexion-extension (E.FE) as a benchmark-case and achieved through three steps.

Firstly, a musculoskeletal multibody system of the upper limb was developed. This was achieved by integrating the four main muscles responsible for E.FE to an existing osteoarticular model. The muscles were modeled with a via-points method. The proposed model was then validated by comparing the musculo-tendinous lengths and muscle moment-arms with reference values from the literature. The relative root mean square error ($rRMSE$) for musculo-tendinous lengths was below 2.3 % for all muscles. The $rRMSE$ for muscle moment arms reached respectively 14.5 % and 21.4 % for the brachialis and the triceps brachii. This high error is explained by the absence of wrapping objects in the proposed model and was only observed when the elbow is fully flexed or extended. The $rRMSE$ on muscle moment arms for the other muscles was below 7.0 %.

Secondly, the newly developed musculoskeletal model was used to quantify the muscle forces with a non-electromyography-based method. This was done with three different cost functions, namely Crowninshield, Forster, and Wen, by formulating the optimization process as an optimal control problem. The quantified muscles forces differed depending on the cost function used. Crowninshield cost function resulted in the lowest muscle forces overall while Forster and Wen were higher since they both include muscle co-contraction in their formulation. The $rRMSE$ between the E.FE torque from inverse dynamics and the E.FE torque computed from muscle forces was below 5 % for the E.FE movement. The $rRMSE$ was higher during functional tasks but stayed below 10 %.

Thirdly, an exoskeleton was integrated to the musculoskeletal model to validate its performance through simulation. The exoskeleton was able to compensate for 80 % of the user's E.FE torque produced by the muscles. However, the reduction of the joint torque did not translate into a reduction of the actual muscle forces. Indeed, the quantified muscle forces showed an increase with

the exoskeleton. This increase in the quantified muscle forces is most likely happening to compensate for the spurious forces or torques introduced by the exoskeleton's misalignment at the elbow joint.

To conclude, this research introduced a new musculoskeletal model of the upper limb for muscle forces quantification that can be used as a validation tool for exoskeleton synthesis. This approach is important as it helps to rapidly identify weaknesses in the exoskeleton architecture. Future work should focus on integrating shoulder and forearm muscles to the model so it can be used on a wider range of upper limb movements and exoskeleton joints.

TABLE OF CONTENTS

ACKNOWLEDGEMENTS III

RÉSUMÉ IV

ABSTRACT VI

TABLE OF CONTENTS VIII

LIST OF TABLES XII

LIST OF FIGURES XV

LIST OF BOXES XXI

LIST OF SYMBOLS AND ABBREVIATIONS XXII

LIST OF APPENDICES XXIV

CHAPTER 1 INTRODUCTION 1

1.1 Motivation 1

1.2 Overview of thesis 2

CHAPTER 2 THEORETICAL BACKGROUND AND LITERATURE REVIEW 4

2.1 Anatomy and physiology of the upper limb 4

2.1.1 Anatomic referential system 4

2.1.2 Biomechanics of the upper limb 5

2.1.3 Upper limb impairments 12

2.2 Upper limb exoskeletons 14

2.2.1 Definition and historic 14

2.2.2 Passive exoskeletons 19

2.2.3 Active exoskeletons 19

2.2.4 Limitations and challenges 19

2.3 Quantification of individual muscle forces 22

2.3.1 Muscle redundancy problem 22
2.3.2 Electromyography-based quantification 23
2.3.3 Non-electromyography-based quantification 27
2.4 Human modeling in biomechanics 31
2.4.1 Open-loop and closed-loop systems 32
2.4.2 ROBOTRAN formalism 34
2.5 Multibody system dynamics applied to exoskeletons 39
2.5.1 Human-exoskeleton interactions 39
2.5.2 Inverse dynamics problem 40
2.5.3 Exoskeleton optimization problem 41
2.6 Optimal control 43
2.6.1 Formalism 43
2.6.2 Solving an optimal control problem 45
2.7 Thesis rationale 51
2.7.1 Problem 51
2.7.2 Research objectives 52
CHAPTER 3 MUSCULOSKELETAL MULTIBODY MODEL OF THE UPPER LIMB 53
3.1 Methodology 53
3.1.1 Data acquisition 53
3.1.2 Osteoarticular model 54
3.1.3 Muscles modeling 55
3.1.4 Literature-based verification of the model 59
3.2 Results 60
3.3 Discussion 62

CHAPTER 4 QUANTIFICATION OF MUSCLE FORCES 63

4.1 Methodology 63

4.1.1 Optimal control problem definition 63

4.1.2 Optimal weights selection for the objective function 65

4.1.3 Muscle force quantification on functional tasks 70

4.2 Results 71

4.2.1 Optimal weights for $\boldsymbol{pT}$ and $\boldsymbol{pQ}$ 71

4.2.2 Optimal weight for $\boldsymbol{pMu}$ 77

4.2.3 Muscle force quantification 86

4.3 Discussion 92

4.3.1 Optimal weights for $\boldsymbol{pT}$, $\boldsymbol{pQ}$, and $\boldsymbol{pMu}$ 92

4.3.2 Muscle force quantification 93

CHAPTER 5 VALIDATION OF AN EXOSKELETON PERFORMANCE 95

5.1 Preliminary work 95

5.1.1 Integration of the exoskeleton 96

5.1.2 Geometric customization 97

5.1.3 Dynamic sizing 99

5.1.4 Results & discussion 101

5.2 Methodology 102

5.3 Results 103

5.4 Discussion 106

CHAPTER 6 GENERAL DISCUSSION 108

6.1 Musculoskeletal model of the upper limb 108

6.2 Quantification of muscle forces 109

6.3 Validation of the exoskeleton performance 110

6.4 Research contributions 111

6.5 Limits of the project and future work 111

CHAPTER 7 CONCLUSION 113

REFERENCES 115

APPENDICES 130

LIST OF TABLES

Table 2.1 Synovial joints and their respective number of prismatic (translation) or rotational degrees of freedom (DoF) 6

Table 2.2 Passive assistive exoskeletons developed between 2010 and 2022 17

Table 2.3 Active assistive exoskeletons developed between 2010 and 2022 18

Table 2.4 List of the main cost function for quantification of individual muscle forces 29

Table 3.1 Muscles characteristics of the arm and muscles model: number of via-points, number of muscle segments, peak force, physiological cross-sectional area (PCSA). Reference values [99] for optimal fiber length, tendon slack length, pennation angle, and moment arm are also presented.....58

Table 3.2 $RMSE$ of the musculo-tendinous lengths between the arm and muscles model and the reference model for each muscle as well as the $rRMSE$.....60

Table 3.3 $RMSE$ of the muscle moment arms between the arm and muscles model and the reference model for each muscle as well as the $rRMSE$. 61

Table 4.1 Face-centered central composite design of the final design space for pT and pQ and the experimental results for trajectory error ($RMSEtraj$) and number of iterations ($iter$). Experimental results are computed after solving the optimal control problem. 72

Table 4.2 ANOVA for quadratic model of each of the final design space for pT and pQ. Significant variables (p-value < 0.05) are highlighted in bold. 73

Table 4.3 Coefficient of determination ($R2$**)** and adjusted $R2$ for the final quadratic models.....74

Table 4.4 Predicted response values from desirability functions and experimental values from OCP with estimated optimal values for pT $(6.3 \cdot 103)$ and pQ $(1.6 \cdot 10 - 5)$. 74

Table 4.5 Estimated optimal value for pT and pQ by GA and their respective response variables. 76

Table 4.6 Identification of the initial design space upper bound for pMu.Weights pT and pQ are set respectively to $6.3 \cdot 103$ and $1.6 \cdot 10 - 5$, while $pMuMu \geq (pQQ = 2.8 \cdot 10 - 4)$ ..77

Table 4.7 Face-centered central composite design of the final design space for pT, pQ, and pMu and the experimental results for trajectory error ($RMSEtraj$), number of iterations ($iter$), and muscle torque error ($rRMSEQ$). Experimental results are computed after solving the optimal control problem with Crowninshield (Cr) cost function. 78

Table 4.8 Face-centered central composite design of the final design space for pT, pQ, and pMu and the experimental results for trajectory error ($RMSEtraj$), number of iterations ($iter$), and muscle torque error ($rRMSEQ$). Experimental results are computed after solving the optimal control problem with Forster (Fo) cost function. 79

Table 4.9 Face-centered central composite design of the final design space for pT, pQ, and pMu and the experimental results for trajectory error ($RMSEtraj$), number of iterations ($iter$), and muscle torque error ($rRMSEQ$). Experimental results are computed after solving the optimal control problem with Wen cost function. 80

Table 4.10 Coefficient of determination ($R2$) and adjusted $R2$ for the final quadratic models of each muscle cost function 81

Table 4.11 Constant, linear, interaction, and quadratic term coefficient of the second-order models for Cr, Fo, and Wen cost function. Significant variables are highlighted in bold. 82

Table 4.12 Predicted response values from desirability functions and experimental values from OCP with estimated optimal values for pT, pQ, and pMu. 86

Table 4.13 Optimal values for pT, pQ and pMu. 86

Table 4.14 $rRMSFM$ during E.FE movement for each muscle cost function 87

Table 4.15 Experimental values from OCP with optimal values of pT, pQ, and pMu for each functional movement (ES, ZC, AR) and each muscle cost function (Cr, Fo, Wen) 89

Table 4.16 $rRMSFM$ during ES, ZC, and AR functional movement for each muscle cost function. 90

Table 5.1 Experimental design for the dynamic sizing of the exoskeleton (Adapted from [196]). 100

Table 5.2 Impact of the integration of the exoskeleton on the human elbow torque $QH, E.FE$ during the functional tasks. 103

Table 5.3 *User torque ratio C* for each functional movement (ES, ZC, AR) and muscle cost function (Cr, Fo, Wen). 104

Table 6.1 Research contributions and their associated specific objective (SO).....111

LIST OF FIGURES

Figure 2.1 Representation of the anatomical neutral position with the corresponding anatomical reference planes: Frontal, Sagittal, and Transverse (Image adapted from [23]). 5

Figure 2.2 Anatomy of the upper limb illustrating the three principal upper limb complex and their respective bones: the shoulder, the elbow, and the wrist (Image adapted from [27]). 6

Figure 2.3 Types of synovial (diarthrosis) joints in the human body: A. Pivot joint; B. Hinge joint; C. Saddle joint; D. Plane joint; E. Condyloid joint; F. Ball-and-socket joint (Image adapted from [28]). 7

Figure 2.4 Rotational degrees of freedom of the shoulder joint: Flexion-Extension (sagittal plane), Abduction-Adduction (frontal plane), and Internal-External Rotation (transverse plane) (Image adapted from [29]). 8

Figure 2.5 Scapulothoracic degrees of freedom: Elevation-Depression, Protraction-Retraction, and Upward-Downward Rotation (Image adapted from [30]).....8

Figure 2.6 Flexion-Extension of the elbow (sagittal plane) [31]. 9

Figure 2.7 Pronation-Supination of the forearm (transverse plane) [31]. 9

Figure 2.8 Muscles of the upper arm, with elbow extensors and flexors highlighted in purple: A. Triceps brachii, posterior view; B. Biceps brachii, anterior view; C. Brachialis, anterior view; D. Brachioradialis, anterior view (Image adapted from [34]).....11

Figure 2.9 Degrees of freedom at the wrist [31]: Flexion-Extension (sagittal plane) and Abduction-Adduction (frontal plane). 12

Figure 2.10 The Hardiman exoskeleton prototype, developed by General Electric [54].....14

Figure 2.11 Evolution of the Hybrid Assistive Limb: HAL-1, HAL-3, and HAL-5 [56].....15

Figure 2.12 Example of an exoskeleton for A. Augmentation (BLEEX [57]), B. Rehabilitation (ChARMin [58]), and C. Assistance (WREX [59]) 16

Figure 2.13 An example of soft actuators used for a hand exoskeleton prototype for assistance [79]. 20

Figure 2.14 Illustration of the four main muscles actuating the elbow: triceps brachii (*TRI*), biceps brachii (*BIC*), brachialis (*BRA*), brachioradialis (*BRD*) (Image adapted from [92]). 23

Figure 2.15 Steps in an electromyography-based quantification of muscle forces. 1. Record raw EMG signal; 2. Signal rectification; 3. Signal normalization and low-pass filtering; 4. Muscle excitation signal; 5. Muscle activation signal; 6. Normalized muscle force computation (Image adapted from [19]).....24

Figure 2.16 Representation of the Hill-type muscle model [100]. A muscle consists of three elements: a series element (SE), a contractile element (CE), and a passive element (PE). Pennation angle α separates the tendon (LT) from the muscle ($LM\cos\alpha$).....26

Figure 2.17 Representation of two multibody kinematic chains [132]: A. Open-loop system. B. Closed-loop system 32

Figure 2.18 Schematic of A. an open-loop and B. a closed-loop model of the forearm. Illustrated in the schematic are the elbow flexion-extension (FE) and forearm pronation-supination (PS) axis, as well as humeroulnar (HU), humeroradial (HR), radioulnar (RU), and radiocarpal (RC) joints (Image adapted from [27]). 33

Figure 2.19 Schematic representation of two kinematics constraints for multibody system loop closure [132]: A. Body cut. B. Ball cut. 37

Figure 2.20 Simplified representation of the human-exoskeleton interaction with the variables of interest: the user's joint generalized positions $\boldsymbol{qH}$, the user's joint generalized torques $\boldsymbol{QH}$, the exoskeleton joint generalized positions $\boldsymbol{qE}$, the exoskeleton joint generalized torques $\boldsymbol{QE}$, and the exoskeleton dimensions $\boldsymbol{lE}$ (Image adapted from [144]). 39

Figure 2.21 Driving a car as an example of an OCP. Find the controls (acceleration, wheel steer) to follow a defined trajectory (bold line) given the state of the car (position, orientation, speed). 43

Figure 2.22 The continuous Optimal Control Problem [155]: Find the optimal state $\boldsymbol{xt}$ and control $\boldsymbol{ut}$ trajectory on the time interval [0, T], subject to path constraints $\boldsymbol{cx}, \boldsymbol{u} \geq \boldsymbol{0}$. 44

Figure 2.23 Optimal control problem with unsatisfied dynamic constraints [155]. The decision variables are the states at discretized points and the piecewise constant control variables. ..46

Figure 2.24 Representation of a Pareto optimal set (dashed blue line) for a multi-objective optimization with two objective functions ($F1$ and $F2$) [177].....48

Figure 2.25 Four phases for a successful use of response surface methods: screening, characterization, optimization, and verification (Image reproduced from [178]).....49

Figure 3.1 Kinematic chain of the human multibody model [27]. Sternoclavicular (SC) joint, acromioclavicular (AC) joint, glenohumeral (GH) joint, humeroulnar (HU) joint, radioulnar (RU) joint, virtual center of rotation (CoR), humeroradial (HR) joint, ball cut, and radiocarpal (RC) joint.....54

Figure 3.2 Modeling of the first two segments of the lateral head of the triceps brachii in ROBOTRAN with the via-points method. The via-points are represented by the green circles, defined as anchor points in ROBOTRAN. Each segment consists of a massless rigid body segment (TRI_lat_P1 and TRI_lat_P2) that has three degrees of freedom (R1, R3, and T2). A ball cut allows to “close the loop” between two via-points for each muscle segment by introducing three geometrical constraints. 55

Figure 3.3 Representation in 3D of the arm and muscles model from ROBOTRAN. The elbow muscles are modeled with a via-points method. The global reference frame is included in the model: X (red), Y (green), and Z (blue).....57

Figure 3.4 Muscle length representation 59

Figure 3.5 Musculo-tendinous length for each muscle computed from the arm and muscles model (AMM) and extracted from the literature (Holzbaur). 60

Figure 3.6 Moment arms for each muscle computed from the arm and muscles model (AMM) and extracted from the literature (Holzbaur).....61

Figure 4.1 Process to obtain optimal objective function weights in an optimal control problem (OCP) using response surface methodology (RSM) 66

Figure 4.2 Face-centered central composite design for 2 factors. "cube" points (blue circles), axial points (red circles), and center point (green circle).....66

Figure 4.3 Face-centered central composite design for 3 factors. "cube" points (blue circles), axial points (red circles), and center point (green circle).....70

Figure 4.4 Normal probability plot of residuals (top line) and predicted vs residuals values plot (bottom line) for $RMSEtraj$ (left column) and $iter$ (right column).....72

Figure 4.5 Profiles for predicted values and desirability function for $RMSEtraj$ and $iter$. Coded variables X1 and X2 are respectively for weights pT and pQ. Right column shows the desirability function for $RMSEtraj$ and $iter$. Red and blue line respectively indicate variable optimal value and predicted value at optimum. 75

Figure 4.6 Simulated (blue) position of the hand during the E.FE movement with the estimated optimal values for pT and pQ. Experimental position is also shown (purple dashed). 76

Figure 4.7 Profiles for predicted values and desirability function for $RMSEtraj$, $iter$, and $rRMSEQ$ with the Crowninshield cost function. Coded variables X1, X2, and X3 are respectively for weights pT, pQ, and pMu. Right column shows the desirability function for $RMSEtraj$, $iter$, and $rRMSEQ$. Red and blue line respectively indicate variable optimal value and predicted value at optimum. 83

Figure 4.8 Profiles for predicted values and desirability function for $RMSEtraj$, $iter$, and $rRMSEQ$ with the Forster cost function. Coded variables X1, X2, and X3 are respectively for weights pT, pQ, and pMu. Right column shows the desirability function for $RMSEtraj$, $iter$, and $rRMSEQ$. Red and blue line respectively indicate variable optimal value and predicted value at optimum. 84

Figure 4.9 Profiles for predicted values and desirability function for $RMSEtraj$, $iter$, and $rRMSEQ$ with the Wen cost function. Coded variables X1, X2, and X3 are respectively for weights pT, pQ, and pMu. Right column shows the desirability function for $RMSEtraj$, $iter$, and $rRMSEQ$. Red and blue line respectively indicate variable optimal value and predicted value at optimum. 85

Figure 4.10 **A.** Computed E.FE torque with Crowninshield (light blue), Forster (purple), and Wen (red) cost function during E.FE movement. Elbow torque from inverse dynamics is plotted as reference (dashed line). Individual muscle forces estimated with **B.** Crowninshield, **C.** Forster, and **D.** Wen cost function 88

Figure 4.11 Simulated (blue) position of the hand during the **A.** ES, **B.** ZC, and **C.** AR functional task with the optimal values for pT, pQ, and pMu. Experimental position is also shown (purple dashed). 89

Figure 4.12 **A.** Computed E.FE torque with Crowninshield (light blue), Forster (purple), and Wen (red) cost function during ES functional task. Elbow torque from inverse dynamics is plotted as reference (dashed line). Individual muscle forces estimated with **B.** Crowninshield, **C.** Forster, and **D.** Wen cost function. 90

Figure 4.13 **A.** Computed E.FE torque with Crowninshield (light blue), Forster (purple), and Wen (red) cost function during ZC functional task. Elbow torque from inverse dynamics is plotted as reference (dashed line). Individual muscle forces estimated with **B.** Crowninshield, **C.** Forster, and **D.** Wen cost function. 91

Figure 4.14 **A.** Computed E.FE torque with Crowninshield (light blue), Forster (purple), and Wen (red) cost function during AR functional task. Elbow torque from inverse dynamics is plotted as reference (dashed line). Individual muscle forces estimated with **B.** Crowninshield, **C.** Forster, and **D.** Wen cost function. 91

Figure 5.1 The exoskeleton model [196] with fourteen (14) generalized coordinates qE. Joints $qE, 5-7,9,14$ are motorized (highlighted in yellow). The kinematics constraints imposed by the body cuts represent the braces that connect the exoskeleton to the user's arm. The ball cut closes the four-bar mechanism. Prismatic and rotational joints are respectively represented by blue and red arrows. The gas tension spring is not represented in the image. (Image adapted from [14]). 96

Figure 5.2 Optimized dimensions $\boldsymbol{lE}$ of the exoskeleton [196]. **A.** Dimensions $lE, 1-4$ (posterior view) **B.** Dimensions $lE, 5-9$ (top view) **C.** Dimensions $lE, 10-17$ (sagittal view). 97

Figure 5.3 Optimized distances $d1-8$ of the human-exoskeleton model (top view) [196]. Two anatomic landmarks on the torso (C7, TS) as well as the center of rotation of the shoulder ($CRGH$) and the elbow ($CRHU$) are shown. 99

Figure 5.4 Illustration of the 3D model of the optimized exoskeleton [196]. The shoulder, elbow, and forearm movements are actuated by a motor. Passive elements are also integrated in the exoskeleton which enables to reduce the size of the required motors. 101

Figure 5.5 **A.** Computed E.FE torque with Crowninshield (Cr, blue), Forster (Fo, purple), and Wen (red) cost function during ES functional task. Actuator torque for each cost function is plotted as a dashed line in its respective color. Elbow torque from inverse dynamics is plotted as reference (dashed black line). Individual muscle forces estimated with **B.** Cr, **C.** Fo, and **D.** Wen. 105

Figure 5.6 **A.** Computed E.FE torque with Crowninshield (Cr, blue), Forster (Fo, purple), and Wen (red) cost function during ZC functional task. Actuator torque for each cost function is plotted as a dashed line in its respective color. Elbow torque from inverse dynamics is plotted as reference (dashed black line). Individual muscle forces estimated with **B.** Cr, **C.** Fo, and **D.** Wen. 105

Figure 5.7 **A.** Computed E.FE torque with Crowninshield (Cr, blue), Forster (Fo, purple), and Wen (red) cost function during AR functional task. Actuator torque for each cost function is plotted as a dashed line in its respective color. Elbow torque from inverse dynamics is plotted as reference (dashed black line). Individual muscle forces estimated with **B.** Cr, **C.** Fo, and **D.** Wen. 106

LIST OF BOXES

Box 2.1 Anatomy & physiology of the upper limb: take home message.....13

Box 2.2 Upper limb exoskeletons: take home message 21

Box 2.3 Quantification of individual muscle forces: take home message 30

Box 2.4 Human modeling in biomechanics: take home message 38

Box 2.5 Multibody systems dynamics applied to exoskeletons: take home message.....42

Box 2.6 Optimal control: take home message.....50

LIST OF SYMBOLS AND ABBREVIATIONS

AA	Abduction-adduction
ADL	Activities of daily living
AMC	Arthrogryposis multiplex congenita
AMM	Arm and muscles model
AOM	Arm only model
AoR	Axis of rotation
AR	Arm frontal reach
BBD	Box-Behnken design
BIC	Biceps brachii
BPP	Brachial plexus palsy
BRA	Brachialis
BRD	Brachioradialis
CoR	Center of rotation
CP	Cerebral palsy
Cr	Crowninshield
DAE	Differential algebraic equation
DoF	Degrees of freedom
E	Elbow
EMG	Electromyography
ES	Eat with spoon
FCD	Face-centered central composite design
FE	Flexion-extension
FEA	Finite element analysis

Fo	Forster
GA	Genetic algorithm
MBS	Multibody system dynamics
MD	Muscular dystrophy
MS	Multiple sclerosis
NLP	Non-linear problem
OCP	Optimal control problem
PCSA	Physiological cross-sectional area
PS	Pronation-supination
RMS	Root mean square
RMSE	Root mean square error
RoM	Range of motion
rRMSE	Relative root mean square error
RSD	Relative standard deviation
RSM	Response surface methodology
S	Shoulder
ZC	Zip your coat

LIST OF APPENDICES

Appendix A Electromyography fundamentals 130

Appendix B Hill-type model force components 131

Appendix C Spatial parameters of the upper limb muscles 133

Appendix D Musculoskeletal-exoskeleton multibody model in ROBOTRAN 135

CHAPTER 1 INTRODUCTION

1.1 Motivation

Every biological system is subject to loads, motion, stress and strain that affect its movement, size, shape, and structure. The understanding of these mechanical interactions within a biological system and its environment has been an area of interest for years and is known today as biomechanics.

Biomechanics is particularly useful to understand how the musculoskeletal system works. Indeed, the bones, ligaments, cartilage, tendons, and muscles composing the musculoskeletal system give shape to our body and allow us to interact with our environment. Despite the impressive abilities of this system, it is subject to a variety of musculoskeletal disorders that impair its functionality.

This thesis focuses on impairments at the upper limb, for its crucial role in numerous basic needs such as eating, bathing, and getting dressed [1], [2]. It is also needed for multiple practical tasks like lifting objects and using tools. A disorder or an injury at the upper limb can limit the capacity to lift the arm properly, which will generally lead to a decrease in quality of life. This is particularly concerning for people suffering from a disorder that leads to progressive and irreversible deterioration of upper limb functions.

Fortunately, emerging treatments and devices are available to maintain or improve upper limb functions. Aquatic therapy [3], functional electric stimulation [4], and corticosteroids injection [5] are treatment options for musculoskeletal disorders. However, they only allow to slow down the progression of the disease [6]. In contrast, mechanical and robotic aid, such as self-feeding devices [7] and assistive robotic arms (eg. JACO from Kinova Robotics [8]), provide direct support in activities of daily living (ADL). Nonetheless, they do not act directly on upper limb function and can only restore limited autonomy, since their usability is restricted to specific tasks.

Nowadays, exoskeletons are considered as a promising approach to improve or recover upper limb function [9], [10]. Exoskeletons are articulated systems whose joints are generally aligned with the user's joint. This allows for targeted and personalized assistance. Exoskeletons are generally developed for one of the following application domain [11]:

- Augmentation: Increase human performance of healthy users.

- Rehabilitation: Enhancement of the motor function for partial or full recovery.
- Assistance: Continuous support of the user, lowering the efforts required to accomplish ADL.

In general, assistive exoskeletons are considered the most appropriate for increasing the autonomy in ADL. These devices are either passive, i.e., elastic elements, or active, i.e., motorized elements. Passive exoskeletons are simpler but are not usable in a variety of ADL since the assistance level is hard to adjust dynamically [12], [13]. Active exoskeletons can support a wide range of tasks but are complex to design due to the high number of degrees of freedom (DoF) and the added bulkiness of active components and their power source [2].

Emerging approaches propose procedures to determine the right geometric and dynamic parameters to help the synthesis of active assistive exoskeleton [14]. These methods size dynamic elements through an optimisation problem that minimizes the user's joint torques [15], energy consumption [16] or muscle forces [17]. While there is no consensus on the best objective function to minimize, the use of muscle forces is promising since it could provide a more anatomically and physiologically realistic reduction of the user's effort [14].

The quantification of muscle forces is an ongoing challenge for scientists since it requires to solve the muscle redundancy problem [18], [19]. Indeed, numerous muscles work together during motion, generating an infinite number of possible solutions for muscle force repartition. Two main approaches are available to solve the redundancy, either the electromyography (EMG)-based [20] and non-EMG-based method [18]. EMG measures the electrical activity produced by a muscle. EMG-based methods are considered more physiologically coherent than non-EMG-based methods for muscle force estimations. However, they require expensive equipment and are harder to implement. Indeed, EMG-based methods require to initialize multiple parameters that are hard to identify, which can lead to abnormal muscle forces [21]. Recent developments in non-EMG-based methods could allow for a quantification of muscle forces that is coherent with EMG data, while being easier to implement.

1.2 Overview of thesis

This thesis is part of the general objective of facilitating the quantification of muscle forces to bring a new tool in the dynamic synthesis process of exoskeletons. Following this introductory chapter,

chapter 2 presents the theoretical background and a critical literature review necessary to understand this project. First, a description of the upper limb anatomy and physiology is presented. It is followed by a summary of diagnoses that can impair upper limb movements. A review on upper limb exoskeletons is then presented. The review concludes with ongoing challenges and limitations to improve the design and acceptance of exoskeletons. Next, the overactuation problem of muscle force quantification is explained. An accurate quantification of muscle forces could improve the design of exoskeletons, allowing to adjust its dynamic components to the user's needs. Then, the main methods for human and exoskeleton modeling are presented. An emphasis is given to multibody system dynamics, which is chosen for this thesis. Optimal control theory is presented as a solution to solve the overactuation problem of muscle forces and human-exoskeleton interactions. The challenge of identifying optimal weights for the objective function of the optimal control problem is presented. Chapter 2 concludes with the problem formulation and the research objectives of this thesis.

The musculoskeletal model of the upper limb is presented in chapter 3. The methodology to add muscles to a previously developed osteoarticular model is presented, followed by the validation of the model by a comparison with a reference model available in the literature.

Chapter 4 presents the approach to identify the optimal weights for the objective function of the optimal control problem. Two different methods are explored, based respectively on design of experiments and evolutionary algorithms. The identified optimal weights are then used for the quantification of muscle forces during three functional tasks.

Next, chapter 5 presents a previously developed procedure for geometric and dynamic synthesis of exoskeletons. Improvements on the procedure are described. The impact of the exoskeleton on muscle forces is then investigated.

Finally, chapter 6 presents a general discussion of the results obtained with the musculoskeletal model developed during this thesis. This chapter concludes by presenting the limitations of the model, needed improvements and future applications.

CHAPTER 2 THEORETICAL BACKGROUND AND LITERATURE REVIEW

This chapter presents the necessary theoretical background and literature review to put forward the relevance of this research project. Section 2.1 summarizes the biomechanics of the upper limb, by presenting the main articular groups and their role as well as some musculoskeletal disorders that impair upper limb movements and autonomy in activities of daily living. Section 2.2 reviews the recent developments in upper limb exoskeletons, which are promising to restore independence, and highlights the actual design and usability challenges. Section 2.3 introduces two approaches to quantify individual muscle forces and, hence, solve the muscle redundancy problem. Section 2.4 briefly reviews methods for human modeling and focuses on the multibody system dynamics (MBS) and their use in biomechanics. Section 2.5 presents human-exoskeleton interactions and design approaches in MBS. Section 2.6 reviews the fundamentals of optimal control and different optimization procedures. Finally, Section 2.7 concludes this chapter with the problem formulation and the research objectives of this thesis.

It is worth noting that a take home message is available as an orange box at the end of each section, which briefly summarizes the important aspects addressed.

2.1 Anatomy and physiology of the upper limb

2.1.1 Anatomic referential system

The anatomical neutral position and the three anatomical reference planes, i.e. frontal, sagittal and transverse, are presented in Figure 2.1. They will be referred to throughout this thesis when describing some arm movements.

The frontal plane separates the body into anterior (front) and posterior (back) sections and is used to describe side bending movements as well as abduction (limb away) or adduction (limb towards) [22]. An example of a movement in the frontal plane is the abduction-adduction (AA) of the shoulder. The sagittal plane separates the body into left and right sections and is used to describe forward or backward movements, as well as flexion (bending) or extension (straightening) [22]. The flexion-extension (FE) of the elbow and the shoulder are examples of movements in the sagittal plane. Finally, the transverse plane separates the body into superior (top) and inferior (bottom)

sections and is used to describe twisting movements as well as limb rotation [22]. In the anatomical neutral position, the pronation-supination (PS) of the forearm is a movement in the transverse plane.

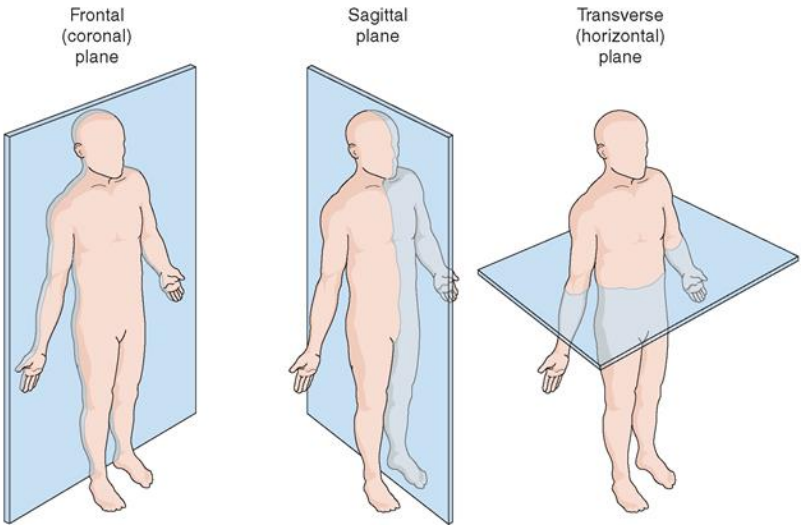

Figure 2.1 Representation of the anatomical neutral position with the corresponding anatomical reference planes: Frontal, Sagittal, and Transverse (Image adapted from [23]).

2.1.2 Biomechanics of the upper limb

The role of the upper limb in ADL is essential [24]. Indeed, it is needed to eat, bathe, and get dressed, as well as carry objects of different sizes and weights. To understand how the upper limb can move the hand around the body in ADL, it is important to know its biomechanics. There are four principal structures composing the upper limb that join the bones together (Figure 2.2): the shoulder, the elbow, the wrist, and the hand/fingers.

Each structure is composed of bones that are held together by several ligaments. Bones are also linked together by multiple muscles, the ends of which are called tendons [25]. The interface between two or more bones is called an articulation. The type of articulation influences the general motion of the bones.

In the human body, synovial joints, also known as diarthrosis, are the articulations that provide most movement and are characterized by a great range of motion (RoM) [26]. The synovial joints found in the human body are summarized in Figure 2.3. In addition, Table 2.1 lists the corresponding number of prismatic (translational) and rotational DoF for each joint.

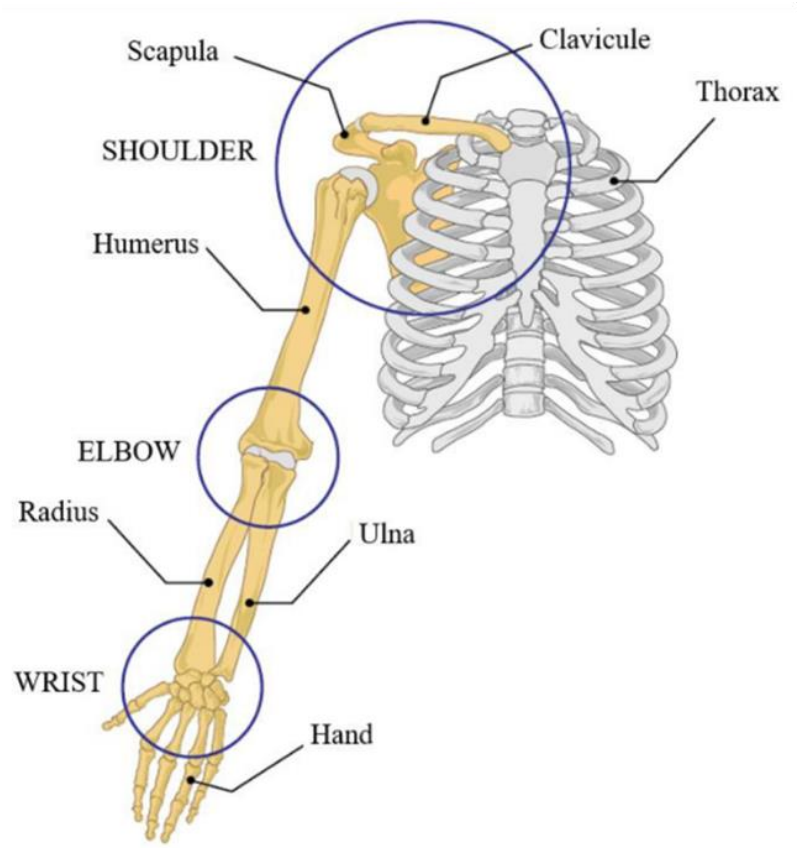

Figure 2.2 Anatomy of the upper limb illustrating the three principal upper limb complex and their respective bones: the shoulder, the elbow, and the wrist (Image adapted from [27]).

Table 2.1 Synovial joints and their respective number of prismatic (translation) or rotational degrees of freedom (DoF)

Joint Type	**Prismatic DoF**	**Rotational DoF**
Pivot	0	1
Hinge	0	1
Saddle	0	2
Plane	2	0
Condyloid	0	2
Ball-and-socket	0	3

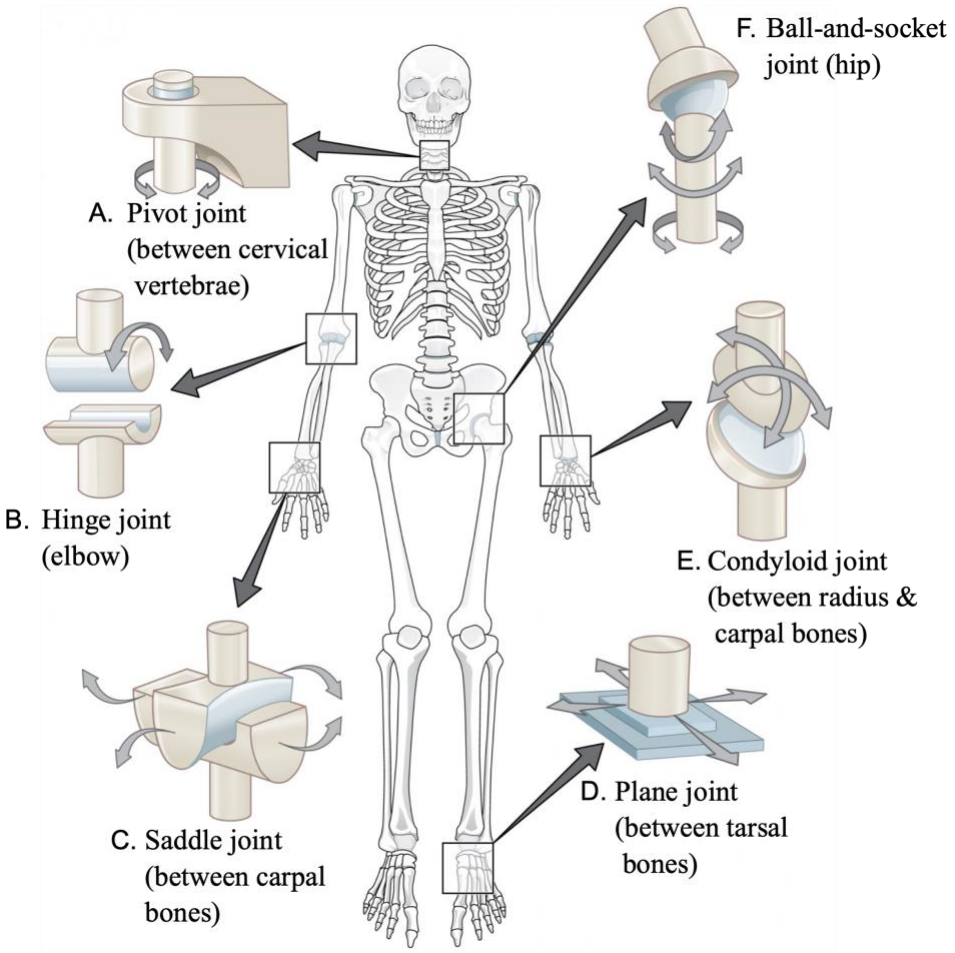

Figure 2.3 Types of synovial (diarthrosis) joints in the human body: A. Pivot joint; B. Hinge joint; C. Saddle joint; D. Plane joint; E. Condyloid joint; F. Ball-and-socket joint (Image adapted from [28]).

For the remainder of this thesis, the notation "*joint or segment abbreviation.DoF*" is used when referring to a particular upper limb movement. The letters S, E, F, and W respectively abbreviates the shoulder, the elbow, the forearm, and the wrist. For instance, the shoulder and elbow FE will respectively abbreviate as S.FE and E.FE.

2.1.2.1 The shoulder complex

The shoulder complex allows for a wide RoM of the upper limb. Composed of four articulations (glenohumeral, acromioclavicular, sternoclavicular, and scapulothoracic) and three bones (clavicle, scapula, and humerus), the shoulder is often kinematically simplified as a ball-and-socket joint. This type of joint allows three DoF, namely FE (sagittal plane), AA (frontal plane), and

internal-external rotation (transverse plane) (Figure 2.4). However, this simplification does not consider the complex interaction of the scapula and the clavicle with the thorax, which allows for three additional DoF: protraction-retraction, elevation-depression, and upward-downward rotation (Figure 2.5). These DoF are essential to enable the arm to be raised above a certain level.

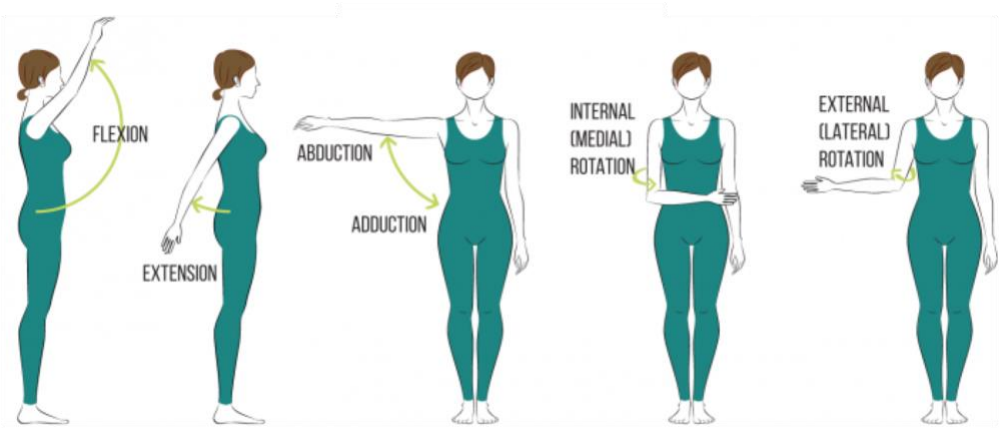

Figure 2.4 Rotational degrees of freedom of the shoulder joint: Flexion-Extension (sagittal plane), Abduction-Adduction (frontal plane), and Internal-External Rotation (transverse plane) (Image adapted from [29]).

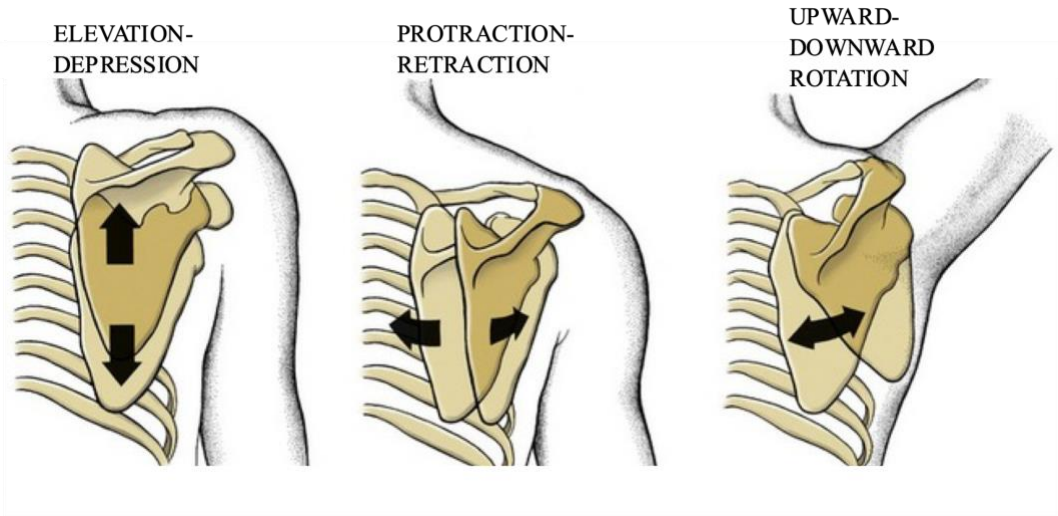

Figure 2.5 Scapulothoracic degrees of freedom: Elevation-Depression, Protraction-Retraction, and Upward-Downward Rotation (Image adapted from [30]).

2.1.2.2 The elbow complex

The elbow complex allows for two DoF, namely elbow FE (sagittal plane) (Figure 2.6) and forearm PS (transverse plane) (Figure 2.7). The combination of these movements is primordial since they allow the hand (and what it holds) to be brought back at head level for visual examination or feeding. Composed of three articulations (humeroulnar, humeroradial, radioulnar) and three bones (humerus, ulna, radius), the elbow is often kinematically represented as a hinge and a pivot joint, respectively for E.FE and F.PS. However, using a single pivot joint to represent F.PS is a simplification of the real interaction between the forearm bones. Indeed, the radius and ulna articulate with each other both proximally and distally, which allows for F.PS of the forearm. This complex interaction should be included in biomechanical analysis to ensure optimal accuracy [27].

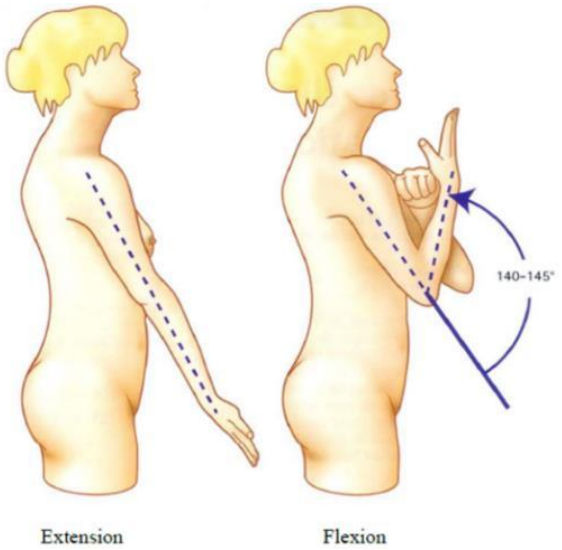

Figure 2.6 Flexion-Extension of the elbow (sagittal plane) [31].

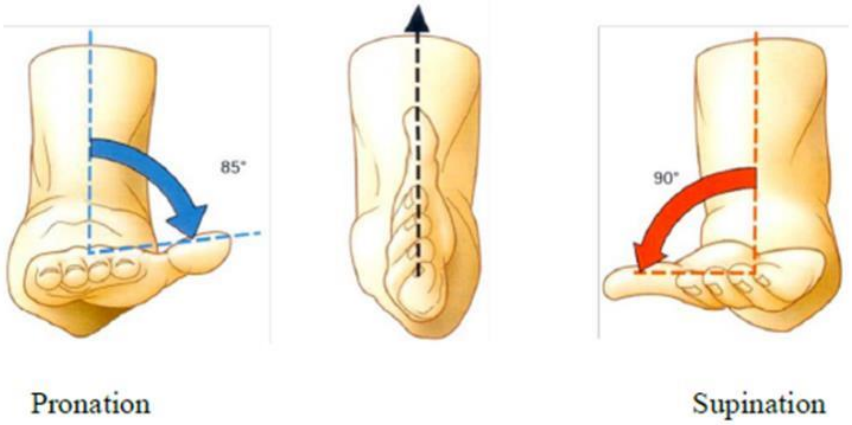

Figure 2.7 Pronation-Supination of the forearm (transverse plane) [31].

A focus of this thesis is around the movement of E.FE, for its importance in self-feeding. Therefore, the main muscles responsible for E.FE are presented thereafter (Figure 2.8):

- The **triceps brachii** is the principal elbow extensor. The triceps brachii is in the posterior compartment of the arm and has three heads, namely long (TRI_{long}), lateral (TRI_{lat}), and medial (TRI_{med}) head. The long head originates from the scapula while both the lateral and medial head originate from the humerus. All three heads converge into a single tendon that inserts into the ulna [32].
- The **biceps brachii** is the principal elbow flexor. The biceps brachii is in the anterior compartment of the arm and has two heads, namely long (BIC_{long}) and short (BIC_{short}) head. Both head originate from the scapula and converge into a single tendon that inserts into the radius [32].
- The **brachialis** is also an elbow flexor. The brachialis (*BRA*) is in the anterior compartment of the arm and has only one head. It originates from the humerus and inserts into the ulna [32].
- The **brachioradialis** is another elbow flexor. The brachioradialis (*BRD*) is in the posterior compartment of the forearm and has only one head. It originates from the humerus and inserts into the radius [32].

The anconeus is another elbow muscle that is considered as an elbow extensor. However, it was not included in this research project since it contributes mainly as a joint stabilizer and does not significantly contribute to elbow kinematics and kinetics [33].

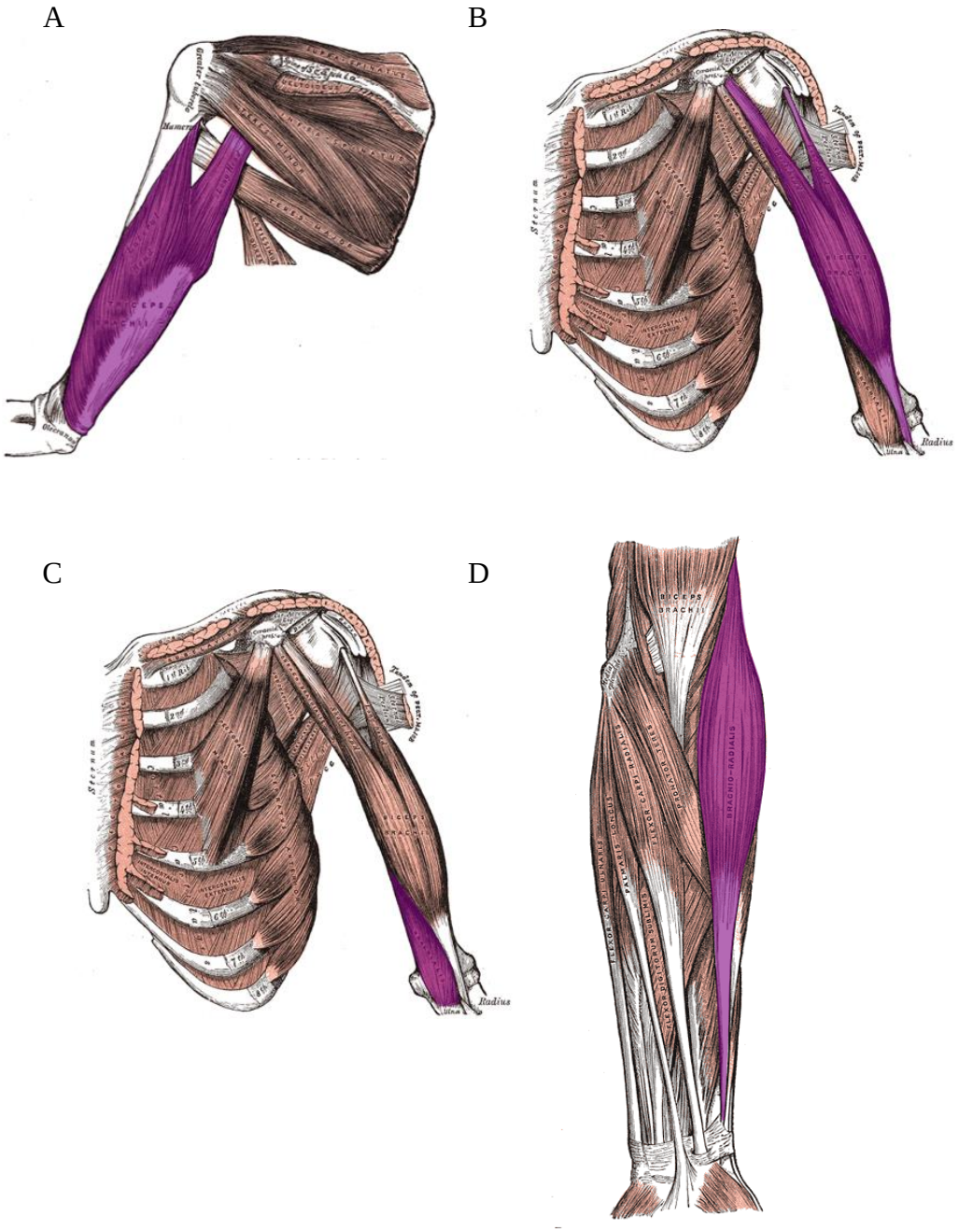

Figure 2.8 Muscles of the upper arm, with elbow extensors and flexors highlighted in purple: A. Triceps brachii, posterior view; B. Biceps brachii, anterior view; C. Brachialis, anterior view; D. Brachioradialis, anterior view (Image adapted from [34]).

2.1.2.4 The wrist complex and the hand

The wrist complex allows for two DoF, namely FE and AA (Figure 2.9). The radiocarpal articulation (radius, carpal bones) is responsible for these movements. The rotation axes of these movements can generally be assumed coincident [35]. Finally, the hand and fingers allow for grasping different objects and ensure dexterity for a multitude of tasks through FE of all fingers and AA of the thumb.

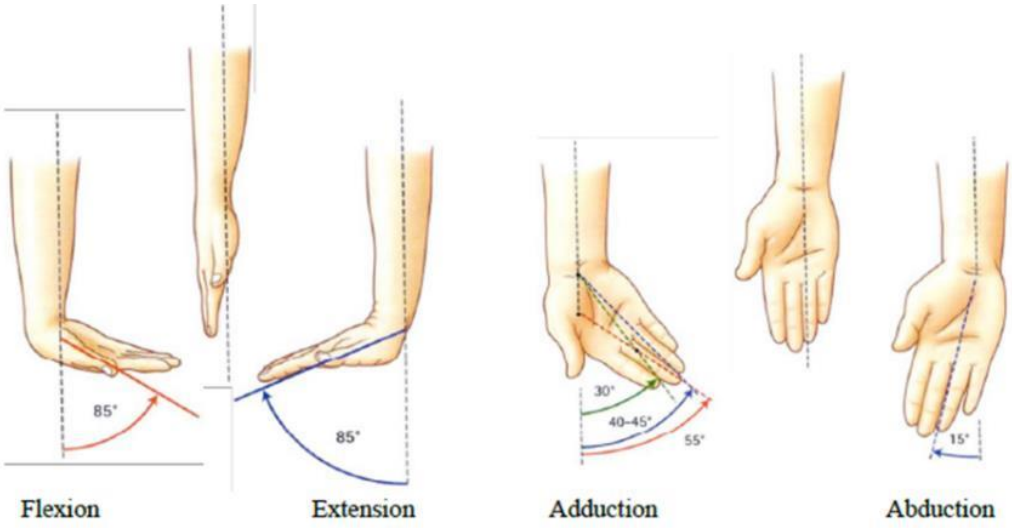

Figure 2.9 Degrees of freedom at the wrist [31]: Flexion-Extension (sagittal plane) and Abduction-Adduction (frontal plane).

2.1.3 Upper limb impairments

There are numerous diagnoses that impair upper limb movements, which generally result in lack of force or reduced motor function at the upper limb [36], limiting autonomy in ADL. Some diagnoses are known at birth, such as muscular dystrophy (MD) [37], spinal muscular atrophy [38], cerebral palsy [39], arthrogryposis multiplex congenita (AMC) [40], and brachial plexus palsy [41]. The prevalence varies from 1 in 500 to 1 in 10,000 live births depending on the diagnosis. Upper limb impairments can also appear in adulthood because of stroke, spinal cord injury, multiple sclerosis (MS), or repetitive strain injury [42]–[44].

This thesis focuses on diagnoses that lead to progressive and irreversible deterioration of motor physical function, such as MD, AMC, and some types of MS [42], [45], [46]. Therefore, it is of the

utmost importance to provide treatments and tools that will slow down the symptoms progression and allow to maintain social participation as well as independence in ADL. Traditional treatments include strength training and aquatic therapy, as well as neuromuscular electrical stimulation and corticosteroids injection. The efficiency of these treatments to slow down the symptoms progression relies on the frequency and intensity at which they are provided [47]. Moreover, the treatment quality and its benefits often rely on the availability of specialized therapists or equipment. However, it is almost impossible to ensure sufficient hours or appropriate equipment for everyone with an upper limb impairments [48].

The progressive deterioration of motor function will eventually lead to a point where traditional treatments are no longer helping. Therefore, in the long term, approaches that reduce the effort needed to perform ADL are preferred [49]. Mobile arm supports are an example of assistive technology that can assist the upper limb in ADL. These mechanical devices are generally mounted to a wheelchair, or a tabletop [50]. They mostly support E.FE, which limits their use in complex ADL that require support for multiple DoF [51]. A promising approach lies in the development of exoskeletons, which can be directly worn by the user. Moreover, they can provide continuous support to multiple joints for people with an upper limb impairment, allowing participation in complex ADL [51].

Box 2.1 Anatomy & physiology of the upper limb: take home message

- The upper limb is fundamental in multiple activities of daily living (ADL) such as eating, washing, and interacting the environment. The movement of flexion-extension (FE) of the elbow is particularly important, as it is essential for self-feeding.
- There are four main muscles that actuate the elbow during FE. The biceps brachii, brachialis, and brachioradialis are responsible for elbow flexion, while the triceps brachii is responsible of extension.
- There exist multiple diseases that can impair upper limb movements. Their origin varies, but most lead to progressive and irreversible deterioration of upper limb function. Exoskeletons are a promising tool to help people with an upper limb impairment maintain independence in ADL.

2.2 Upper limb exoskeletons

2.2.1 Definition and historic

An upper body exoskeleton is a device that resembles the structure of the human upper limb and whose joints are aligned to the user's joints. An exoskeleton can be used to augment, enhance, or support the user motor function [11]. The concept of exoskeleton for mobility assistance dates to 1883 [52]. However, it took close to 80 years to see a successful prototype, named the Hardiman [53]. Based on a master-slave configuration, the Hardiman was developed for military purposes, with the final objective to enhance the user's strength and performance (Figure 2.10). The master-slave configuration of the Hardiman involved two overlapping exoskeletons. The inner one (master) followed the user's movement while the outer one (slave) reproduced a powered version of the movement performed by the inner exoskeleton.

Figure 2.10 The Hardiman exoskeleton prototype, developed by General Electric [54].

The second generation of exoskeletons appeared around 1990, with the idea of physical human-robot interaction presented by Kazerooni et al. [55], which allows a direct transfer of mechanical

power to the user, without using a master-slave approach. Work on the Hybrid Assistive Limb (HAL) started in these years and went through multiple cycles of development (Figure 2.11) [56]. Nowadays, HAL is an assistive suit for everyday motion (lower limb) and is now commercially available.

Figure 2.11 Evolution of the Hybrid Assistive Limb: HAL-1, HAL-3, and HAL-5 [56]

Early work on exoskeletons mainly focused on the lower limb to help with walking. Nonetheless, the interest for upper limb exoskeletons has seen a continuous growth since the early 2000s. Nowadays, there are about 20 different upper limb exoskeletons commercially available, and more than 40 exoskeletons are still in the research and development phase [10]. To help potential users and their therapists identify the right exoskeleton among multiple options, classification methods are used to categorize exoskeletons based on shared characteristics. A common method of classification is based on the intended application domain of the exoskeleton [11], i.e. augmentation, rehabilitation, assistance (Figure 2.12). An augmentation exoskeleton's primary purpose is to increase human strength and endurance [53]; they are generally developed for the military end. The main purpose of rehabilitation exoskeletons is to enhance or restore motor function by allowing partial or full recovery of the impairment. They are generally available in a clinical setting and used during therapy. Assistive exoskeletons, for their part, support the motor function by facilitating the movements of the upper limb. They are generally available to use in

everyday life to provide support in ADL. Assistive exoskeletons can also have a rehabilitation purpose. However, they are mainly aimed for diagnoses that cannot be improved.

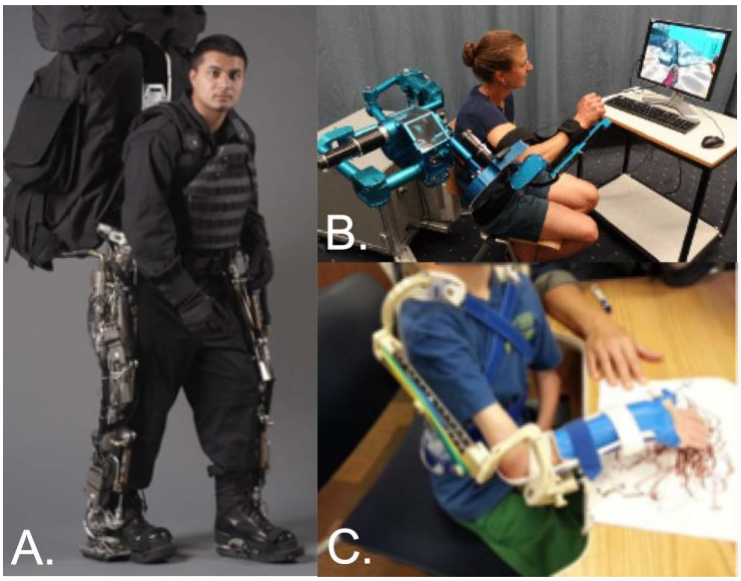

Figure 2.12 Example of an exoskeleton for A. Augmentation (BLEEX [57]), B. Rehabilitation (ChARMin [58]), and C. Assistance (WREX [59])

Section 2.1.3 Upper limb impairments presented numerous upper limb impairments that lead to progressive and irreversible deterioration, which are the focus of this thesis. For people with a severe upper limb impairment due to MD, AMC or MS, assistive exoskeletons remain the best option available since they allow to support upper limb movements in ADL.

Assistive exoskeletons developed between 2010 and 2022 were reviewed for this thesis. Each exoskeleton was classified regarding its motorization solution, i.e., passive, or active. Table 2.2 and Table 2.3 respectfully present the reviewed passive and active assistive exoskeletons. For each exoskeleton, details on the articulation(s) supported, its main feature, and the targeted population(s) are available. The following references should be consulted for a more exhaustive review on upper limb exoskeletons: Gull et al. [10], Gopura et al. [11], Qassim and Wan Hasan [60], Rehmat et al. [61], Gupta et al. [9]. For a review focused on pediatric exoskeletons, one can refer to the work published by the author [48].

Table 2.2 Passive assistive exoskeletons developed between 2010 and 2022

Name	Articulations supported	Feature(s)	Targeted Population
Airframe [62]	Shoulder	Lowers exertion levels by up to 80%	Professional and skilled trade workers
Mate [63]	Shoulder	Reduces muscular effort by 30% at shoulder level	Overhead workers
Paexo Shoulder [64]	Shoulder	Relieves physical stress by more than 50%	Overhead workers
ShoulderX [65]	Shoulder	Compatible with LegX and BackX	Overhead workers
Skelex 360-XFR [66]	Shoulder	Reduces fatigue up to 79%	Overhead workers
Vex [67]	Shoulder	Exerts a force up to 5 kg	Overhead workers
EVO (EksoVest) [68]	Shoulder	Exerts a force up to 6.8 kg	Overhead workers
WREX [69]	Shoulder, Elbow	Enhances functionality in some ADL	DMD, AMC, CP, SMA
P-WREX [70]	Shoulder, Elbow	Improves reaching ability at hip and chest level	AMC, BPP, Other
Playskin Lift [13]	Shoulder	Increases functionality during play time	AMC, BPP, Other
Playskin Air [71]	Shoulder	Lifts a human arm up to 90°	AMC, BPP, Other
Yumen Arm [45]	Shoulder	Increases range of motion	SMA, DMD

Abbreviations: ADL: Activities of daily living, DMD: Duchenne muscular dystrophy, AMC: Arthrogryposis, CP: Cerebral Palsy, SMA: Spinal muscular atrophy, BPP: Brachial plexus palsy

Table 2.3 Active assistive exoskeletons developed between 2010 and 2022

Name	**Articulation supported**	**Feature(s)**	**Targeted Population**
Myopro [72]	Elbow, wrist, hand	Only marketed medical device that may restore independence in ADL	Stroke, BPP, Cerebral palsy, Multiple Sclerosis
SPEXO [2]	Shoulder, elbow, wrist	Provides a self-reliant method for eating or drinking	Stroke and spinal cord injury
RUPERT [73]	Shoulder, elbow, wrist	Enhances motor function of paretic arm in stroke patients	Stroke
Carbonhand [74]	Hand	Improves hand grip strength and function	Stroke and injury leading to hand disability

Abbreviations: ADL: Activities of daily living, BPP: brachial plexus palsy, DMD: Duchenne muscular dystrophy, AMC: Arthrogryposis

2.2.2 Passive exoskeletons

Passive exoskeletons consist of unpowered systems that can store energy from the human movements and release it when needed. This is achieved by integrating springs, or dampers into the design of the exoskeleton. Table 2.2 lists passive assistive exoskeletons developed between 2010 and 2022.

2.2.3 Active exoskeletons

Active exoskeletons consist of powered actuators that enhance the user's function, thus reducing the effort necessary to accomplish a particular ADL. The integrated actuators can be of different natures, such as electric motors, cable-driven systems, or pneumatic actuators. Table 2.3 lists active assistive exoskeletons developed between 2010 and 2022.

2.2.4 Limitations and challenges

One of the most important challenges for assistive exoskeletons is to make them light and compact so that they are comfortable to wear for a long period of time [52]. This challenge is easier to meet for passive than active exoskeletons. Indeed, the gravity compensation mechanisms in passive exoskeletons work with elastic machine elements, such as springs or rubber bands. These elements are lightweight and mostly compact. In contrast, active exoskeletons rely on actuators that need a power source. These elements add additional weight and bulkiness to the device that can be significant. Soft actuators could eventually revolutionize active exoskeletons (Figure 2.13). These actuators are lightweight, power-efficient, and safe for human-robot interaction [75]. However, efficient control of soft actuators is an ongoing challenge so their safe implementation in exoskeleton could take time [76], [77]. Nevertheless, the important number of commercially available passive exoskeletons in comparison to active exoskeletons shows that there are still important challenges for the latter to achieve consistent commercial use.

Excellent wearability often comes at the cost of lower functionality [13]. Indeed, passive exoskeletons are known to be wearable, but they are limited in the number of supported articulations. Moreover, there is generally no means to dynamically adapt the level of the power assistance of the device according to the user's need [78]. Hence, the support provided by the exoskeleton to the user will only be optimal for the ADL that it was specifically configured for.

Figure 2.13 An example of soft actuators used for a hand exoskeleton prototype for assistance [79].

To illustrate this limitation, let's take the example of eating a meal at the table. Generally, the exoskeleton will be adjusted so that the shoulder is flexed and internally rotated with the forearm pronated. This shoulder position will allow an E.FE in a horizontal plane (not against gravity) and will facilitate self-feeding. When the meal is done, the exoskeleton adjustments will keep the shoulders flexed around the chest level. The user will need to either produce a continuous force to lower his arms along his body or get the help of someone to adjust the exoskeleton support.

The above-mentioned example is not relevant for active exoskeletons. Indeed, it is possible for an actuated system to self-adjust to the user's need. Moreover, there exists active exoskeletons that can support most, if not all, articulations of the upper limb [2], [73]. However, a reliable interpretation of the user's intention is required to ensure optimal functionality of the exoskeleton. This is possible through efficient control of the exoskeleton [80]. Fast and accurate control of exoskeleton is an ongoing challenge, but important progress have been made in the last years thanks to breakthrough in signal processing and artificial intelligence [81].

The sizing of dynamic components in active exoskeletons is primordial. Indeed, if the dynamic components are too weak, the exoskeleton might be unable to support the user's arm weight. In contrast, if the dynamic components are too strong, the exoskeleton might injure the users by moving too fast or producing high contact forces. Therefore, the dynamic components should be custom-sized to the user's condition [82]. This customization is preferred to ensure optimal support and to minimize the risk of injury.

The customization process should consider the user's anatomy and physiology to account the heterogenicity of people with upper limb impairments. Indeed, both children and adults can benefit

the use of an exoskeleton. There are however major differences in anthropometry and the level of assistance needed for these two groups. A precise geometric sizing will ensure alignment of the exoskeleton joints with the user's articulation. This is important as misalignment produces spurious forces and torques on the user, which causes discomfort and can lead to injury [83]. The dynamic sizing will adapt the support in terms of joint torque needed by the user. This sizing is important since joint torques are significantly different between children, teenager, and adults [84]–[86]. Dynamic sizing of an exoskeleton based on joint torques has been successful [14], [87]. However, customization based on muscle forces could provide a more accurate solution when specific muscles are impaired [17]. For example, this is the case for people suffering from AMC, where elbow flexors are generally more impaired than the elbow extensors [46].

Box 2.2 Upper limb exoskeletons: take home message

- Exoskeletons are used either for rehabilitation, assistance, or human augmentation. Assistive exoskeletons are better suited for impairments that lead to irreversible deterioration of the upper limb function since they can provide continuous support in activities of daily living.
- Assistive exoskeletons are either passive or active. Passive exoskeletons use elastic elements to support the upper limb while active exoskeletons use actuators. Passive exoskeletons are lightweight, but only aid one or two movements. In contrast, active exoskeletons are bulkier and heavier, but can support all upper limb movements.
- There is a need for better sizing of active exoskeletons to optimize functionality and safety. This sizing must be based on the user's anatomy and physiology, i.e., age, diagnosis, muscle forces, segment lengths, etc.

2.3 Quantification of individual muscle forces

The knowledge of muscle forces could help the sizing of the dynamics of exoskeletons to ensure optimal support. Indeed, knowledge of muscle force distribution could improve treatments in rehabilitation [88], enhance sports performance [89], and reduce the risk of injury [90]. Nowadays, the quantification of joint efforts is possible thanks to the measurement of kinematics and external efforts. However, the additional step of going from joint effort to muscle force distribution is challenging since most joints are over-actuated, which gives rise to the muscle redundancy problem.

2.3.1 Muscle redundancy problem

The number of muscles in the human body is way higher than the number of joints. Indeed, there is on average 2.6 muscles for each DoF of the human body [91]. As presented in Section 2.1.2, this research project considers 4 muscles that are responsible for elbow actuation. These muscles can either act in synergy or co-contract during elbow movement. Synergistic muscles work together to create a movement, i.e., *BIC*, *BRA*, and *BRD* for elbow flexion. Co-contraction happens when two or more muscles around a joint act in opposite directions during a movement, i.e., *BIC* and *TRI* during E.FE.

The presence of synergy and co-contraction in muscles creates what is called an undetermined system. Mathematically, it means that there are fewer equations than unknown for the system. Physiologically, it means that there is an infinity of combinations of muscle forces to produce the same resulting joint effort. Figure 2.14 illustrates the undetermined system for E.FE.

There are four actuators involved in this system. The flexor set (or agonist) is composed of the BIC_{long}, BIC_{short}, *BRA*, and *BRD*. The extensor set (or antagonist) is composed of the TRI_{long}, TRI_{lat}, and TRI_{med}.

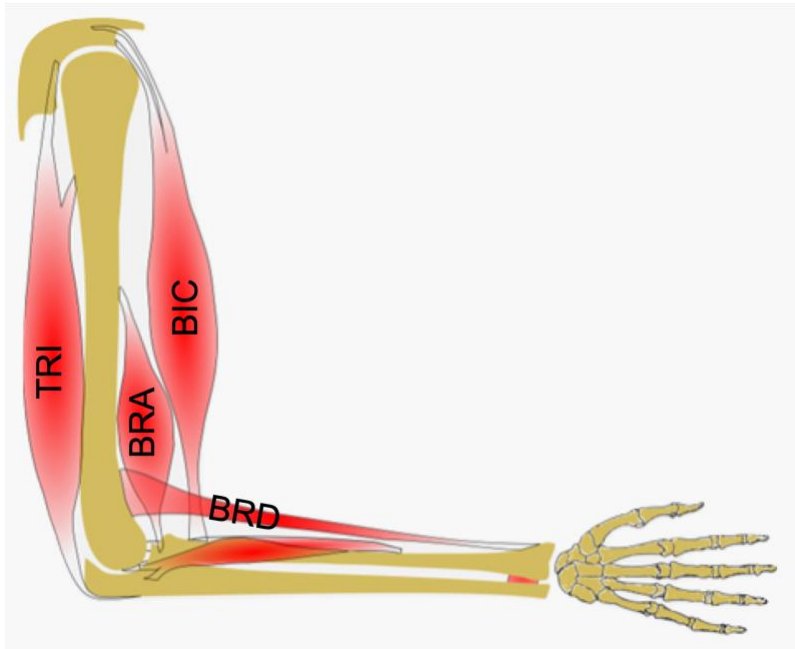

Figure 2.14 Illustration of the four main muscles actuating the elbow: triceps brachii (*TRI*), biceps brachii (*BIC*), brachialis (*BRA*), brachioradialis (*BRD*) (Image adapted from [92]).

The mathematical formulation of the E.FE redundancy is as follows:

$$\boldsymbol{Q_{H,E}} = \sum_{i=1}^{N} \boldsymbol{d_i} \cdot \boldsymbol{F_{m_i}} \tag{2.1}$$

where $\boldsymbol{Q_{H,E}}$ is the resultant human joint torque vector at the elbow and can be computed by inverse dynamics, $\boldsymbol{d_i}$ is the moment arm vector of the ith muscle for i = 1, …, N, and $\boldsymbol{F_{m_i}}$ is the muscle force vector produced by the ith muscle. The following sections (2.3.2 & 2.3.3) present two different approaches to solve the muscle redundancy problem.

2.3.2 Electromyography-based quantification

Electromyography-based quantification aims to predict the individual muscle forces by recording the muscle activity with electromyography (EMG). The reader can refer to Appendix A – Electromyography fundamentals for additional theory on EMG. The many steps required to obtain muscle force from raw EMG will be briefly presented here and are illustrated in Figure 2.15. It is important to keep in mind that most researchers use a subset of these steps, which allows for a variety of EMG-based models. In short, from raw EMG signals, muscle activation is obtained through a model of muscle activation dynamics. Then, muscle activation is transformed to muscle

forces through a model of muscle contraction dynamics. The computation of muscle activation dynamics and muscle contraction dynamics is not a trivial task.

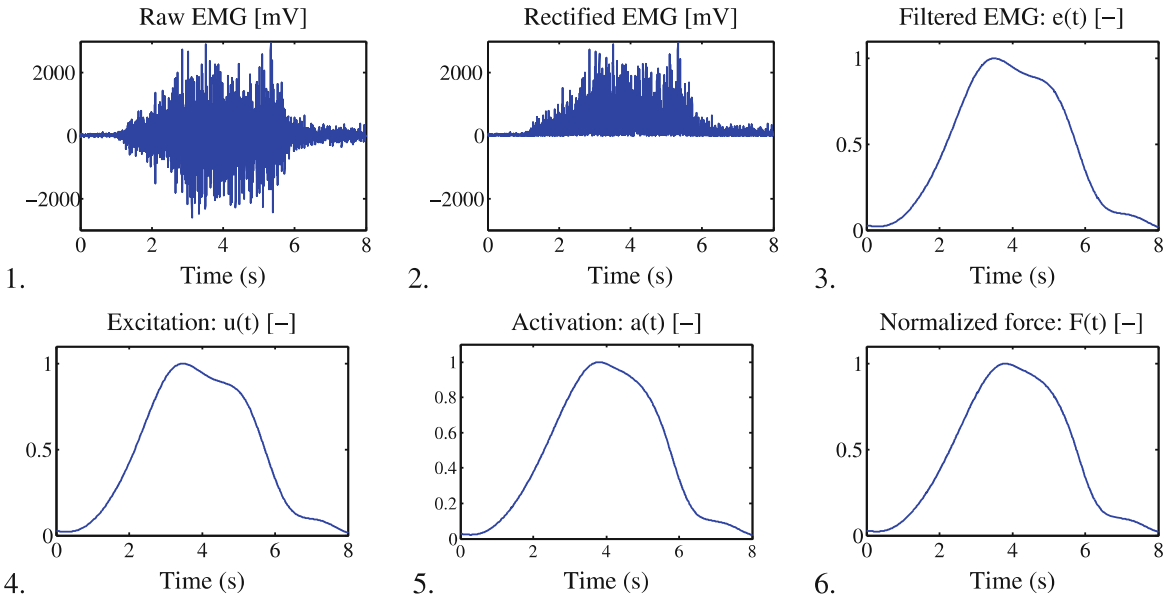

Figure 2.15 Steps in an electromyography-based quantification of muscle forces. 1. Record raw EMG signal; 2. Signal rectification; 3. Signal normalization and low-pass filtering; 4. Muscle excitation signal; 5. Muscle activation signal; 6. Normalized muscle force computation (Image adapted from [19]).

2.3.2.1 Muscle activation dynamics

Muscle activation dynamics [93] transforms the raw EMG signal, which is a voltage both positive and negative, to muscle activation, which is expressed as a number between 0 and 1. It is the first step towards muscle force quantification. First, any offset is removed from the raw EMG (Figure 2.15A) before the signal is rectified (Figure 2.15B). The rectified EMG is then low-pass filtered to obtain its envelope. The signal is finally normalized with respect to its maximal value to obtain the filtered EMG, $e(t)$, a value between 0 and 1 (Figure 2.15C). The normalization step requires additional recording of maximal voluntary isometric contraction to obtain an EMG maximal value [94]. Since there is a delay between the time at which the motor unit is triggered and the muscle contracts, the excitation signal, $u(t)$ (Figure 2.15D), is obtained from the filtered EMG using the following first order differential equation [95]:

$$\tau_{ne}\dot{e} + e = u \tag{2.2}$$

where τ_{ne} is the excitation time constant [19].

The muscle activation, $a(t)$ (Figure 2.15E), is finally obtained from the muscle excitation signal by resolving another first-order differential equation [96]:

$$\tau_{a,j}(a_j, u_j)\dot{a}_j + a_j = u_j \tag{2.3}$$

where $\tau_{a,j}(a_j, u_j)$ is a time constant which varies with activation level and whether the muscle activation level is increasing or decreasing [96]:

$$\tau_{a,j}(a_j, u_j) = \begin{cases} \tau_{act,j}(0.5 + 1.5a_j) & if\ u_j \geq a_j \\ \dfrac{\tau_{deact,j}}{0.5 + 1.5a_j} & if\ u_j < a_j \end{cases} \tag{2.4}$$

where $\tau_{act,j}$ and $\tau_{deact,j}$ are respectively the activation and deactivation time constant. $\tau_{act,j}$ and $\tau_{deact,j}$ are set respectively to 0.015 and 0.050 [97].

2.3.2.2 Muscle contraction dynamics

The contraction dynamics transforms the muscle activation signal, $a(t)$, to musculo-tendinous force, $F(t)$ (Figure 2.15F), based on physiological models. One of the most physiologically reliable models in the literature is the Huxley-type model [98]. However, Huxley-type model is governed by multiple differential equations that need to be numerically integrated. This makes the model computationally time-consuming and almost impossible to use for modeling multiple muscle forces [20]. For this reason, most researchers use the well-known Hill-type model [97].

In Hill-type models (Figure 2.16), each musculo-tendon unit is composed of:

- The tendon, generally modeled as a passive wire: an elastic *Series Element* (SE).
- The muscle, generally modeled as the contractile element: an active *Contractile Element* (CE) in parallel with a *Passive Element* (PE).

Further, the musculo-tendinous force, $F(t)$, is computed with the following equation:

$$F(t) = \left(\underbrace{a(t)\tilde{F}_l^{CE}(\tilde{l}_m)\tilde{F}_v^{CE}(\tilde{v}_m)}_{active} + \underbrace{\tilde{F}_l^{PE}(\tilde{l}_m)}_{passive} + \underbrace{b_m\tilde{v}_m}_{damping} \right) \tag{2.5}$$

where:

- $a(t)$ is the muscle activation signal obtained from Eq. 2.4, a number between 0 and 1.

- $\tilde{F}_l^{CE}(\tilde{l}_m)$, $\tilde{F}_v^{CE}(\tilde{v}_m)$, and $\tilde{F}_l^{PE}(\tilde{l}_m)$ are respectively the *force-length*, *active force-velocity*, and *passive force-length* relations [95]–[97]. The sign $\sim$ above the variables means that they are normalized, i.e., $\tilde{F}_l^{CE}$, $\tilde{F}_v^{CE}(\tilde{v}_m)$, and $\tilde{F}_l^{PE}(\tilde{l}_m)$ are normalized with respect to F_{max}, the muscle length $\tilde{l}_m$ is normalized with respect to the optimal muscle fiber length L_m^{opt} (from [99], and the muscle velocity $\tilde{v}_m$ is normalized with respect to the muscle maximal contraction velocity v_{max} (from [99]).

The *force-length*, *active force-velocity*, and *passive force-length* relations are defined in Appendix B – Hill-type model force components.

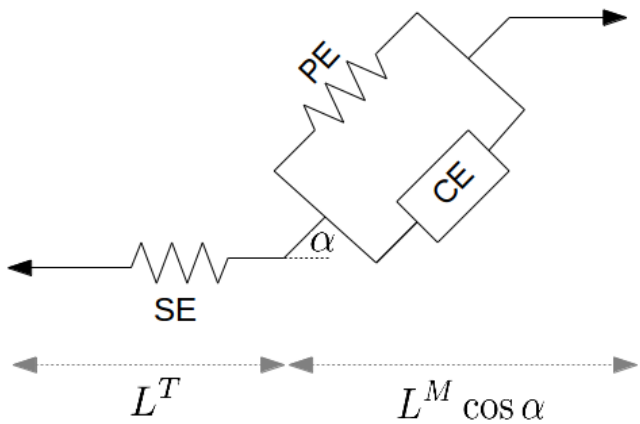

Figure 2.16 Representation of the Hill-type muscle model [100]. A muscle consists of three elements: a series element (SE), a contractile element (CE), and a passive element (PE). Pennation angle α separates the tendon (L^T) from the muscle ($L^M \cos\alpha$)

The musculo-tendinous force $F(t)$ is also a value between 0 and 1. To obtain a value in Newton, $F(t)$ must be multiplied by F_{max}, the maximal isometric force that the muscle can produce:

$$F_{mt}(t) = F_{max} \cdot F(t) \tag{2.6}$$

F_{max} is either taken from tables [99] or is calibrated individually [94].

Even though the contraction dynamics based on Hill-type models are widely spread [19], [20], [94], [101], [102], there are still some limitations and challenges to its use. First, its implementation needs the resolution of differential equations, which can be computationally time-consuming for models with numerous muscles. Secondly, most equations are based on factors given by statistical tables, which have not been revisited for numerous years and do not account for subject variability

(kids vs adult, female vs male, healthy vs impaired). Finally, evaluation of musculo-tendinous force relies on the recording of raw EMG data. Ensuring quality of EMG signals can be challenging since the signal varies due to numerous factors. Factors affecting EMG reliability are either causative (e.g., electrode placement and skin resistance), intermediate (e.g., signal crosstalk), or deterministic (e.g., number of active motor units). Moreover, recording EMG requires generally expensive equipment, that is not always easily accessible.

2.3.3 Non-electromyography-based quantification

Non-electromyography-based quantification aims to predict the individual force distribution without the need of a direct measurement on the muscle such as EMG. This is mainly possible with the help of cost functions[1]. The idea of using a cost function to solve the redundancy problem of the muscles originated from Weber and Weber [103]. Since then, numerous cost functions have been proposed. Table 2.4 lists and comments the evolution of the existing cost functions.

Among the cost functions presented in Table 2.4, the maximum-endurance, criterion proposed by Crowninshield and Brand [104], is the most widely accepted and commonly used in the literature [105]–[107]. However, the cost function proposed by Crowninshield and Brand underestimates antagonist activity, as it does not account for muscle co-contraction [107]. The cost function proposed by Forster et al. [108] tried to tackle the problem of co-contraction by introducing a shift parameter for the optimization criterion. Nevertheless, the authors stated that the constant co-contraction factor should vary for different muscles and could change temporarily, without providing any tools to help its estimation. This difficulty to identify a good co-contraction factor value limits its practical use.

The recent cost function developed by Wen et al. [18] proposed a novel approach to non-EMG-based quantification. The proposed cost function introduces a co-contraction factor for elbow muscles that is calibrated on EMG data during E.FE. The calibration step allowed for the formulation of an empirical formula that defines co-contraction based on or derived from kinematic data:

---

[1] In this thesis, the term “cost function” is associated to the evaluation of muscle forces, while the term “objective function” is associated to the optimization problem of the OCP.

$$x_s = 6.67 \cdot Q_{H,E} + 7.57 \tag{2.7}$$

where x_s is the co-contraction factor, and $Q_{H,E}$ is the elbow joint torque obtained from inverse dynamics. Results obtained by the authors showed that the quantification of muscle forces are more coherent with EMG-driven models than other cost functions [18]. Even though EMG data was required to formulate the co-contraction relationship, it is no longer needed for quantification of muscle forces. Indeed, the empirical formula defining co-contraction is only dependent of the user's joint torque. Therefore, this cost function has the advantage of being easier to use than EMG-based quantification methods, while allowing for physiologically coherent quantification of muscle forces.

Table 2.4 List of the main cost function for quantification of individual muscle forces

Authors	Years	Cost function	Comments
Weber and Weber [103]	1836	-	Initial proposition of the problem, without any cost function
Seireg and Arvikar [109]	1973	$\Omega = \sum_{k=1}^{M} F_{m_k}$	Simple force sum criterion
Penrod et al. [110]	1974	$\Omega = \sum_{k=1}^{M} \gamma_i \cdot F_{m_k}$ γ_i : weighting factors	Weighted force sum criterion. No details on how one should specify weighting factors
Crowninshield and Brand [104]	1981	$\Omega = \sqrt[n]{\sum_{k=1}^{M} \left(\frac{F_{m_k}}{PCSA_k}\right)^n}$ n : power, usually set to 2 or 3, depending on the experimental data	Maximum-endurance criterion. Broadly used today, but does not account for-co-contraction
Dul et al. [111]	1984	$\Omega = \sum_{k=1}^{M} \left(\frac{F_{m_k}}{PCSA_k}\right)$	Minimum-fatigue criterion. Emphasize the importance of PCSA in optimization.
Forster et al. [108]	2004	$\Omega = \sum_{k=1}^{M} \left(\frac{F_{m_k}}{F_{max_k}} - x_s\right)^2$ x_s: constant co-contraction factor	Minimum-force sum criterion with co-contraction factor.
Wen et al. [18]	2018	$\Omega = \sqrt[3]{\sum_{k=1}^{M} \left(\frac{F_{m_k} - x_s(Q_{H_i})}{PCSA_k}\right)^3}$ x_s : variable co-contraction factor, dependent of torque at joint Q_{H_i}	Maximum-endurance criterion with co-contraction factor. Co-contraction factor is calibrated on EMG data.

Abbreviations: F_{m_k} : Force of the kth muscle; M,: Total number of considered muscles; $PCSA_k$: Physiological cross-sectional area of the kth muscle; F_{max_k} : Maximum voluntary force of the kth muscle; Q_{H_i}: Human joint torque at joint i, actuated by M muscles.

Box 2.3 Quantification of individual muscle forces: take home message

- Quantification of individual muscle forces is not trivial since it requires solving the muscle redundancy problem. Indeed, there are more muscles than degrees of freedom for most human joints. Therefore, there is an infinity of combinations of muscle forces to produce the same resulting joint effort. Electromyography (EMG) and non-EMG-based methods exist to tackle this problem.
- EMG-based models quantify muscle forces based on a Hill-type representation of muscles, which transforms the raw EMG signal to muscle force. Implementation of Hill-type models requires EMG measurements, factors from statistical tables, and data from musculoskeletal models. Recording reliable EMG data and customizing the different parameters to the user can be difficult and limits the use of EMG-based models.
- Non-EMG-based models quantify muscle forces using a cost function in an optimization procedure. The Crowninshield cost function is widely used and accepted in the literature, but it does not account for muscle co-contraction. The Forster cost function accounts for co-contraction, but the co-contraction factor can vary and is difficult to identify, limiting its practical use.
- The recent cost function proposed by Wen is calibrated on EMG data to estimate the co-contraction factor, which makes it physiologically more coherent with muscle activation and easier to implement than EMG-based models.

2.4 Human modeling in biomechanics

Biomechanical analyzes are important to better understand the underlying mechanics of injury/disease and thus improve diagnosis, prevention and treatment [112]. The use of digital human models to simulate body movements has increased the number of possible analyzes, since real subjects are no longer required [113]. There are two principal approaches to human modeling for biomechanical analysis: multibody system dynamics (MBS) or finite element analysis (FEA).

In MBS, a system is represented as a series of rigid bodies, i.e., non-elastic and of constant mass, connected by joints. MBS is used in the field of ergonomics [114], [115], rehabilitation [116], [117], and sports [118], [119] for its ability to study complex articular movements and their associated internal forces.

In FEA, a system is subdivided into multiple smaller and simpler parts that are called finite elements. This method is mostly used in biomechanics to quantify the deformations or constraints undergone by the human body in quasi-static. FEA are commonly used in orthopaedics to improve the design and performance of bone-implant systems [120].

It is also possible to combine MBS and FEA to create flexible MBS. Flexible MBS are mostly used to study systems that present both highly dynamic movements and body deformations. An example of such system is the prediction of spine treatment for scoliosis patients [121], [122]. However, both FEA and flexible MBS are computationally expensive and tedious to implement, which limits their use [123].

Multiple software programs are available to model or analyze human biomechanics: Adams (MSC Software, USA) [124], AnyBody Modeling System (AnyBody Technology, Denmark) [125], MapleSim (MapleSoft, Canada) [126], OpenSim (SimTK, USA) [127], RBDL [128], ROBOTRAN (UCLouvain, Belgium) [129], and Simscape Multibody (Mathworks, USA) [130]. For this research project, MBS was chosen to model the human body as the focus of this research project is about upper limb movements and their associated internal forces rather than deformations. Moreover, the assumption of rigid body in MBS simplifies the study of the human body since the classical laws of mechanics can be applied. This project is built around ROBOTRAN for its ease of use, its interface with MATLAB, and the expertise available in the

research team [14], [18], [27], [82], [94], [131]. Despite the previous work realized by the research team, there is currently no available upper limb model in ROBOTRAN that includes muscles.

2.4.1 Open-loop and closed-loop systems

The first step to model the human body in MBS is to build the kinematic chain that describes its behavior. A kinematic chain is a succession of rigid bodies linked by joints which describe the DoF between each body. In biomechanics, the bones or body segments are generally modeled as the rigid bodies, while the articular complex are represented by one or multiple joints. Joints can be revolute (rotation) or prismatic (translation) and have a maximum of 6 DoF, i.e., 3 rotations and 3 translations. In MBS, these joints are considered ideal, i.e., force or torque are transferred without loss between each body [129].

Kinematic chains are either an open-loop or closed-loop system, illustrated in Figure 2.17. Good examples of an open-loop system are cranes or serial robots. In contrast, a four-bar mechanism, is a good example of a closed-loop system.

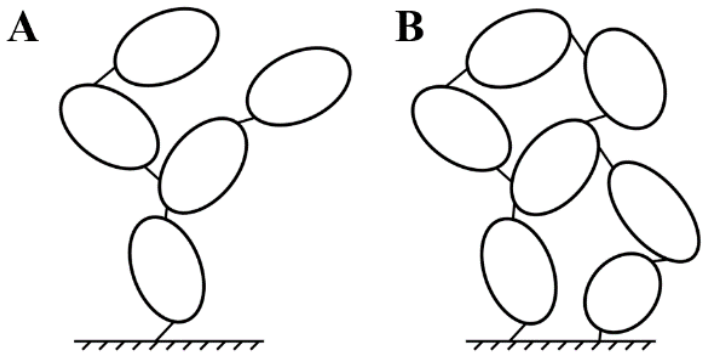

Figure 2.17 Representation of two multibody kinematic chains [132]: A. Open-loop system. B. Closed-loop system

For the modeling of osteoarticular systems, i.e., bones and articulations, both open and closed-loop systems can be used. However, it was shown that using closed-loop systems to model shoulder [133], [134] and forearm movements [27], [135] increases the biofidelity of the model. A model is defined as biofidelic if it provides a realistic representation of human motion. Biofidelity allows for a better quantification of joint kinematics and dynamics, which is needed for an accurate quantitative assessment in biomechanics [27]. Taking the forearm as an example, an open-loop

system will consider the forearm as a single rigid body while a closed-loop system will consider both the radius and ulna (Figure 2.18). When adding muscles to the model, the closed-loop system will be more biofaithful since it will allow to model each muscle insertion on its respective bone. Moreover, closed-loop systems allow for a better definition of joint axis of rotation, thus improving the quantification precision of internal efforts [27].

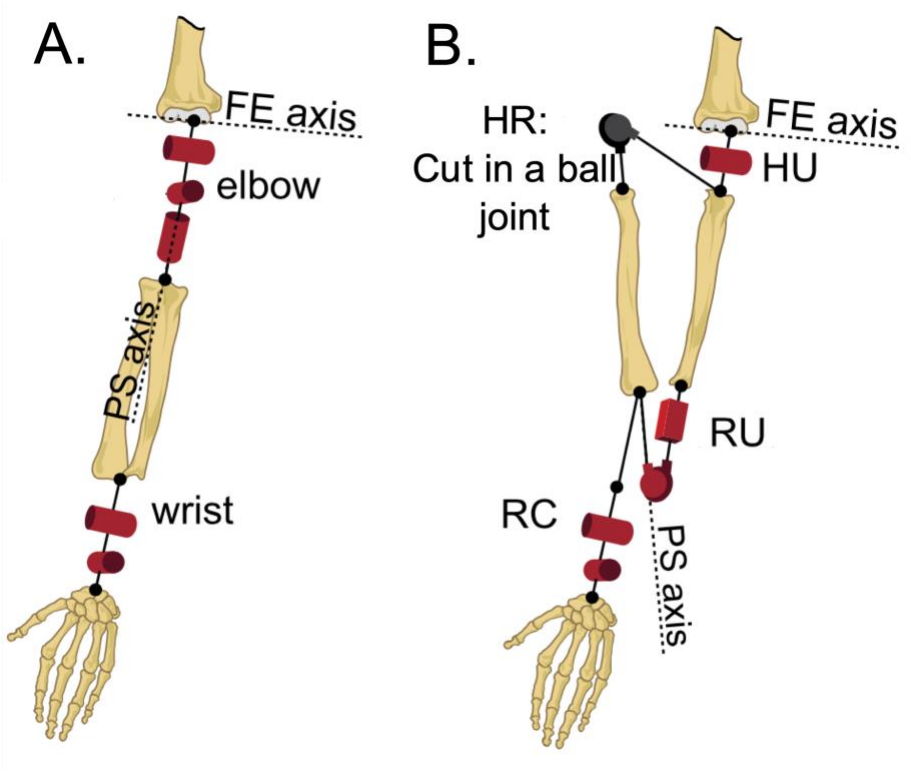

Figure 2.18 Schematic of A. an open-loop and B. a closed-loop model of the forearm. Illustrated in the schematic are the elbow flexion-extension (FE) and forearm pronation-supination (PS) axis, as well as humeroulnar (HU), humeroradial (HR), radioulnar (RU), and radiocarpal (RC) joints (Image adapted from [27]).

2.4.1.1 Muscle modeling

To obtain musculoskeletal models, muscles must be added to osteoarticular models. The common approach to attach muscles to an osteoarticular model [136], [137] is to model them as closed-loop systems. The geometrical path of the muscle defines its length and moment arm, which will affect muscle force and moment production capacity [138]. A muscle path is generally composed of its origin and insertion, as well as via-points. Starting from the muscle's origin, it passes through the via-points like a thread through the eye of a needle to reach its insertion. The via-points can be

fixed to a particular bone, or variable in space [139]. Another possible component in muscle paths is wrapping objects. Wrapping objects are obstacles, modeled as geometric forms, which allow for curved-line segments of muscle [139]. While the integration of wrapping objects can improve the estimation of muscle moment arms, they are difficult to scale to subject-specific models since they are defined by multiple geometric parameters, preventing them from a simple scaling [138]. Moreover, the numerous constraints imposed by wrapping objects largely increase the cost of computation during simulations [140], [141]. Therefore, the preferred solution is often to use via-points fixed to a particular bone or pre-processed moment arms [142]. Pre-processed moment arms can be taken from anatomical tables [99] or obtained through a polynomial relationship [142].

2.4.2 ROBOTRAN formalism

This section presents the formalism underlying ROBOTRAN [129], [132]. The two principal formulations describe respectively the direct and inverse dynamics of the system. Direct dynamics calculates motion from known internal forces and/or torques and reaction forces. In contrast, inverse dynamics quantifies the internal forces and/or torques from a known trajectory and external forces.

In ROBOTRAN, the Newton/Euler laws formulated recursively are used to obtain the equations of motion of a tree-like system. The semi-explicit or *direct dynamics* formulation of the equation reads:

$$\boldsymbol{M}(\boldsymbol{q},\boldsymbol{\delta})\ddot{\boldsymbol{q}} + \boldsymbol{c}(\boldsymbol{q},\dot{\boldsymbol{q}}) = \boldsymbol{Q}(\boldsymbol{q},\dot{\boldsymbol{q}}) \tag{2.8}$$

where:

- $\boldsymbol{M}$ is the generalized mass matrix.
- $\boldsymbol{c}$ is the non-linear dynamic vector containing the external, gravity, and gyroscopic forces.
- $\boldsymbol{q}$, $\dot{\boldsymbol{q}}$, and $\ddot{\boldsymbol{q}}$ are respectively the generalized positions, velocities, and accelerations.
- $\boldsymbol{\delta}$ contains the dynamic parameters of the system (body masses, centers of mass location, and body tensors inertia).
- $\boldsymbol{Q}$ is the generalized forces or torques vector.

The implicit or *inverse dynamics* formulation expresses $\boldsymbol{Q}$ as a function of the system kinematics $\boldsymbol{q}$, $\dot{\boldsymbol{q}}$, $\ddot{\boldsymbol{q}}$ and $\boldsymbol{\delta}$**.** The equation reads:

$$\boldsymbol{Q}(\boldsymbol{q}, \dot{\boldsymbol{q}}) = \boldsymbol{\Phi}(\boldsymbol{q}, \dot{\boldsymbol{q}}, \ddot{\boldsymbol{q}}, \boldsymbol{\delta}) \tag{2.9}$$

When working with a closed-loop system, the generalized joint positions $\boldsymbol{q}$ must satisfy geometric loop constraints $\boldsymbol{h_l}(\boldsymbol{q}) = 0$. The loop constraints available in ROBOTRAN are presented in Section 2.4.2.1 Loop constraints. The loop closure is also needed at the velocity and acceleration level, requiring first- and second-time derivatives of the loop constraints $\boldsymbol{h_l}$. The additional forces created by the constraints are introduced via the Lagrange multipliers technique. The updated formulation for respectively direct and inverse dynamics is:

$$\boldsymbol{M}(\boldsymbol{q}, \boldsymbol{\delta})\ddot{\boldsymbol{q}} + \boldsymbol{c}(\boldsymbol{q}, \dot{\boldsymbol{q}}) = \boldsymbol{Q}(\boldsymbol{q}, \dot{\boldsymbol{q}}) + \boldsymbol{J^T}\boldsymbol{\lambda} \tag{2.10}$$

$$\boldsymbol{\Phi}(\boldsymbol{q}, \dot{\boldsymbol{q}}, \ddot{\boldsymbol{q}}, \boldsymbol{\delta}) = \boldsymbol{Q}(\boldsymbol{q}, \dot{\boldsymbol{q}}) + \boldsymbol{J^T}\boldsymbol{\lambda} \tag{2.11}$$

The loop constraints and their time derivatives are:

$$\boldsymbol{h_l}(\boldsymbol{q}) = 0 \tag{2.12}$$

$$\dot{\boldsymbol{h}}_{\boldsymbol{l}} = \boldsymbol{J}(\boldsymbol{q})\dot{\boldsymbol{q}} = 0 \tag{2.13}$$

$$\ddot{\boldsymbol{h}}_{\boldsymbol{l}} = \boldsymbol{J}(\boldsymbol{q})\ddot{\boldsymbol{q}} + \dot{\boldsymbol{J}}\dot{\boldsymbol{q}}(\boldsymbol{q}, \dot{\boldsymbol{q}}) = 0 \tag{2.14}$$

where $\boldsymbol{h_l}$ are the loop closure geometrical constraints, $\boldsymbol{J}$ is the Jacobian matrix of the system, $\dot{\boldsymbol{J}}\dot{\boldsymbol{q}}$ is the quadratic term of the constraints at acceleration level and $\boldsymbol{\lambda}$ represents the Lagrange multipliers associated with the constraints. In ROBOTRAN, this differential algebraic equation (DAE) system is solved with the Coordinate Partitioning Method [143]. This index reduction method transforms an index-3 system to an index-0 system. Overall, the method creates a partition of independent and dependent generalized coordinates and separates the constraint Jacobian accordingly:

$$\boldsymbol{q} = \begin{pmatrix} \boldsymbol{q_u} \\ \boldsymbol{q_v} \end{pmatrix}; \boldsymbol{J} = \begin{pmatrix} \boldsymbol{J_u} & \boldsymbol{J_v} \end{pmatrix} \tag{2.15}$$

Then, the reduction is performed by simple matrix permutations and operations. The details of these final matrix operations are available in [129]. Finally, the Newton Raphson algorithm is used to solve the algebraic constraints $\boldsymbol{h_l}(\boldsymbol{q})$, which are generally non-linear. The algorithm expresses $\boldsymbol{q_v}$, the dependent coordinates, for given $\boldsymbol{q_u}$, the independent coordinates, through successive iterations of $\boldsymbol{q_v}$.

2.4.2.1 Loop constraints

ROBOTRAN proposes three types of geometric constraints $\boldsymbol{h_l}$ to deal with closed-loop systems. These so-called *cutting* methods allow to re-create a tree-like MBS system:

- Cut of a body.
- Cut in a ball joint.
- Cut of a connecting rod.

Body cuts and ball cuts are the commonly used in biomechanics and are detailed hereafter. Rod cuts are used to replace a connecting rod with negligible mass and inertia. They can be seen in vehicle suspension and steering mechanisms MBS systems.

A body cut, shown in Figure 2.19A, separates a body in two parts, the *original* body, and its *shadow*. The mass and inertia of the initial body is distributed between the two new bodies. There are six constraints involved in a body cut:

- Three translational constraints, imposing the position of points P_o and P_{sh} to coincide in the global reference frame $\{\hat{X}^0\}$.
- Three rotational constraints, imposing the body frame $\{\hat{X}^0\}$ and $\{\hat{X}^{sh}\}$ to align at any time.

A ball cut, shown in Figure 2.19B, is used when the loop contains a ball joint that is considered ideal, i.e., no torque is transmitted through. For this type of cut, only three constraints are needed:

- Three translational constraints, imposing the position of points P_P and P_S, which are located at the ball joint center, to coincide at any time. Points P_P and P_S are respectively attached to body points p and s.

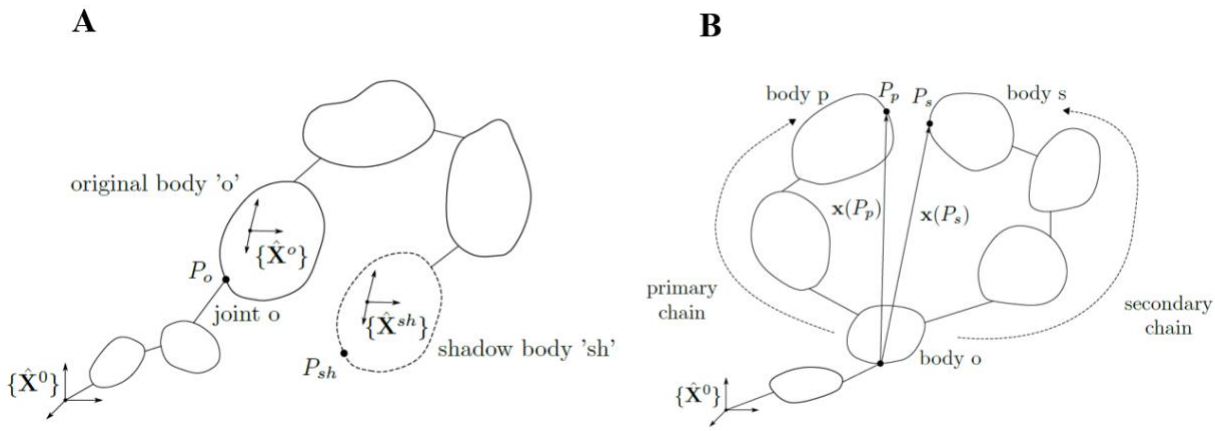

Figure 2.19 Schematic representation of two kinematics constraints for multibody system loop closure [132]: A. Body cut. B. Ball cut.

Box 2.4 Human modeling in biomechanics: take home message

- The most popular methods for human modeling in biomechanics are multibody system dynamics (MBS) and finite element analysis (FEA). A combination of these methods, flexible MBS, is also used. However, both FEA and flexible MBS are computationally expensive and tedious to implement.
- The assumption of rigid bodies is chosen for this research project, given that the deformation of the bodies is not a research objective. ROBOTRAN software was chosen to develop the MBS for its ease of use, its interface with MATLAB, and the expertise in the research team.
- The human body is generally modeled as a closed-loop system to increase the biofidelity and performance of the model. Geometric constraints, such as body or ball cut, are used to deal with closed-loop systems, to re-create tree-like systems, which are easier to analyze.
- Via-points are commonly used to model muscle paths. While the addition of wrapping objects can increase the accuracy of muscle architecture and moment arms, they are computationally expensive to implement and are difficult to scale for subject-specific models. Therefore, they are often ignored in musculoskeletal models.
- In MBS, direct dynamics calculates motion from known internal forces and/or torques and reaction forces. In contrast, inverse dynamics quantifies the internal forces and/or torques from a known trajectory and external forces.

2.5 Multibody system dynamics applied to exoskeletons

2.5.1 Human-exoskeleton interactions

An exoskeleton can be seen a collaborator to human motion. For the collaboration to be efficient, it is important to understand and to model the human-exoskeleton interactions properly. This can be realized with MBS. Moreover, digital models are great tools to test and validate ideas in early stages of exoskeleton design. Figure 2.20 illustrates a simplified model of an upper limb-exoskeleton system. The variables $\boldsymbol{q_H}$ and $\boldsymbol{Q_H}$ are respectively the user's generalized position and torques while $\boldsymbol{q_E}$ and $\boldsymbol{Q_E}$ are respectively the exoskeleton generalized position and torques. The exoskeleton dimensions are represented by the variable $\boldsymbol{l_E}$.

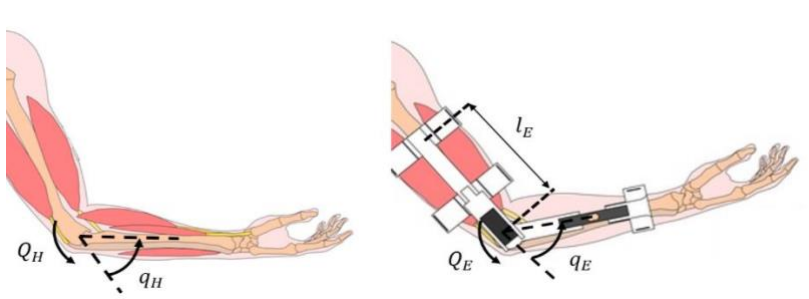

Figure 2.20 Simplified representation of the human-exoskeleton interaction with the variables of interest: the user's joint generalized positions $\boldsymbol{q_H}$, the user's joint generalized torques $\boldsymbol{Q_H}$, the exoskeleton joint generalized positions $\boldsymbol{q_E}$, the exoskeleton joint generalized torques $\boldsymbol{Q_E}$, and the exoskeleton dimensions $\boldsymbol{l_E}$ (Image adapted from [144]).

In MBS, closed-loop systems are needed to model the kinematic interactions between the limb and the exoskeleton. Therefore, geometric constraints are needed to re-create a tree-like structure. In the literature, body cuts are used to attach solidly to one another the exoskeleton and limb segment [145]–[147]. In practical terms, the body cut is equivalent to a solid brace that is wrapped around the user's arm and does not move relatively to the arm. However, this is impossible for real-life use, considering skin movement and deformation, as well as imperfections in the brace system. To account for these imperfections, it is possible to introduce additional joints, such as a translation, in the exoskeleton kinematic chain [145]. In general, the exoskeleton dimensions $\boldsymbol{l_E}$ will be optimized to satisfy the loop constraints, while minimizing the bulkiness of the device.

2.5.2 Inverse dynamics problem

As stated by the inverse dynamics' formulation, one can obtain the generalized joint forces or torques required to accomplish a known trajectory [129]. When designing an exoskeleton for people with upper limb impairments, the general objective is to reduce the user's joint torque $\boldsymbol{Q_H}$ necessary to move the upper limb along a given trajectory $\boldsymbol{q_H}$. Therefore, the exoskeleton torques $\boldsymbol{Q_E}$ that satisfy this objective must be found.

Exoskeleton's joint are generally aligned with the user's joint to minimize the spurious forces or torques at the human-exoskeleton interface, which can lead to discomfort or injuries [83], [148]. Therefore, the trajectory of the exoskeleton is dependent of the user's trajectory, hence $\boldsymbol{q_E} = f(\boldsymbol{q_H}(\boldsymbol{t}))$. This relationship is equivalent to the partitioning of the generalized coordinates (Section 2.4.2) where $\boldsymbol{q_H} = \boldsymbol{q_u}$, the independent variables, and $\boldsymbol{q_E} = \boldsymbol{q_v}$, the dependent variables.

The kinematic loop constraints, imposed by the exoskeleton and described by Eq. 2.12-2.14, introduce the constraints forces ($\boldsymbol{J^T\lambda}$) to the differential algebraic equation (DAE) system. Using the partitioning, it is possible to formulate the inverse dynamics of the problem as follows:

$$\boldsymbol{Q}_{\mathrm{u}} = \boldsymbol{\Phi_u} + \boldsymbol{B^T}_{\boldsymbol{vu}}(\boldsymbol{Q_v} - \boldsymbol{\Phi_v}) \tag{2.16}$$

where $\boldsymbol{Q_u}$ and $\boldsymbol{Q_v}$ are respectively the generalized independent and dependent joint forces and torques, $\boldsymbol{\Phi_u}$ and $\boldsymbol{\Phi_v}$ are respectively the implicit functions of the kinematics and dynamics parameters (mass, CoM, Inertia), and $\boldsymbol{B_{vu}} = -(\boldsymbol{J_v})^{-1}\boldsymbol{J_u}$. In our simplified example, $\boldsymbol{Q_u} = \boldsymbol{Q_H}$ and $\boldsymbol{Q_v} = \boldsymbol{Q_E}$. To find the actuation needed at the joint, generalized forces and torques must be separated in their active and passive component. The active component corresponds to the motorization of the joint while the passive component comes from friction, external forces, spring elements, etc. Therefore, one can reformulate Eq. 2.16 as follows:

$$\boldsymbol{Q_{u,a}} = \boldsymbol{\Phi_u} - \boldsymbol{Q_{u,p}} + \boldsymbol{B^T}_{\boldsymbol{vu}}(\boldsymbol{Q_{v,p}} - \boldsymbol{\Phi_v}) \tag{2.17}$$

where $\boldsymbol{Q_{u,a}}$ and $\boldsymbol{Q_{u,p}}$ are respectively the active and passive component of the independent generalized forces and torques, and $\boldsymbol{Q_{v,p}}$ is the passive component of the dependent generalized forces and torques. It is important to notice that the active component of the dependent generalized forces and torques $\boldsymbol{Q_{v,a}}$ is not included in Eq. 2.17 because this system has a single solution only if the number of independent joints is equal to the number of active joints. However, both active components, i.e., independent ($\boldsymbol{Q_{u,a}}$) and dependent ($\boldsymbol{Q_{v,a}}$), should be considered in human-

exoskeleton systems. As it is the case for muscle force distribution, the problem becomes over-actuated: there is an infinite number of possible solutions to the human-exoskeleton force or torque distribution. Section 2.5.3 presents recent methods used to solve this over-actuation problem.

2.5.3 Exoskeleton optimization problem

This section focuses on the recent optimization procedures to support the design of upper limb exoskeletons.

2.5.3.1 Loop closure and collision avoidance

The loop constraints in human-exoskeleton systems force the exoskeleton to move in symbiosis with the human body. Therefore, loop closure constraints are important for proper trajectory following and effective force transmission. One can choose to optimize loop closure, maximizing the number of closed configurations [149], or to include loop closure as a component of the objective function [150]. The latter is implemented for geometric optimization in this research project since it is very simple to implement and is compatible with gradient-based optimization method. Another important aspect to consider is the risk of collision between the exoskeleton and the user in the operation of tasks. One way to avoid these collisions is to add constraints [147] or collision avoidance algorithms [151].

2.5.3.2 Over-actuation problem

Section 2.5.2 presented the over-actuation problem of human-exoskeleton system with an inverse dynamics formulation. This problem is common in the literature and to mitigate it, optimization problems are defined with objective functions that aim to minimize the user's joint torques [15], energy [16] or muscle forces [17]. There is no consensus regarding the best expression in the design of an exoskeleton. In this work, an objective function using joint torque and muscle forces will be investigated. This approach is chosen since it represents the most direct evaluation of the joint efforts of the user [14].

Finally, the approach for dynamic sizing of exoskeletons varies in the literature. Recent studies [14], [87], [152], [153] managed to combine both active, i.e., motors, and passive, i.e., springs, transmission systems. This combination has proven that the addition of passive elements can reduce the efforts required for the motors. This reduction allows to use smaller motors, which implies a

size and weight reduction of the exoskeleton. The integration of passive elements in an active exoskeleton is included in this research project.

Box 2.5 Multibody systems dynamics applied to exoskeletons: take home message

- In multibody systems dynamics, exoskeletons are modeled as a closed-loop system with the human body. Body cuts are generally used to define the geometrical constraints between the exoskeleton and the body. The exoskeleton dimensions must be optimized to satisfy these constraints.
- Actuated exoskeletons create an over-actuation problem since there is an infinity of possible combinations that solve the inverse dynamics formulation. Therefore, one must define an optimization problem with a precise objective.
- When optimizing the exoskeleton dimensions, it is important to add additional constraints (collision avoidance) to ensure that the exoskeleton does not collide with the human body during motion. Moreover, including loop constraints as a component of the objective function simplifies the optimization problem.
- The exoskeleton's over-actuation problem is solved through the implementation of different objective functions in the optimization problem. The commonly used objective functions aim to minimize the user's joint torque, energy, or muscle forces. However, there is no consensus on the best function to use. Therefore, the final choice for the objective function is up to the researcher.

2.6 Optimal control

Optimal control theory is a branch of mathematical optimization that aims to find a control law for a dynamical system over a specific period [154]. The use of optimal control is widely spread in MBS [155]. An optimal control problem (OCP) is defined by separating variables as control $\boldsymbol{u}$ or state $\boldsymbol{x}$ and by describing the state using dynamic equations.

An easy example to visualize an OCP and understand the meaning of control $\boldsymbol{u}$ and state $\boldsymbol{x}$ variables is one of driving a car (Figure 2.21). In this example, steering the wheel or pushing on the accelerator pedal (controls $\boldsymbol{u}$) dictates the position, orientation, and speed (states $\boldsymbol{x}$) of the car. Control and state variables are usually subject to constraints such as the limit of rotation of the steering wheel for the car. The final element is an objective function, which can be either maximized or minimized while respecting the constraints on control and states variables. For example, one could desire to follow a given trajectory by minimizing the difference between the state variables and a desired trajectory at each point in time [156].

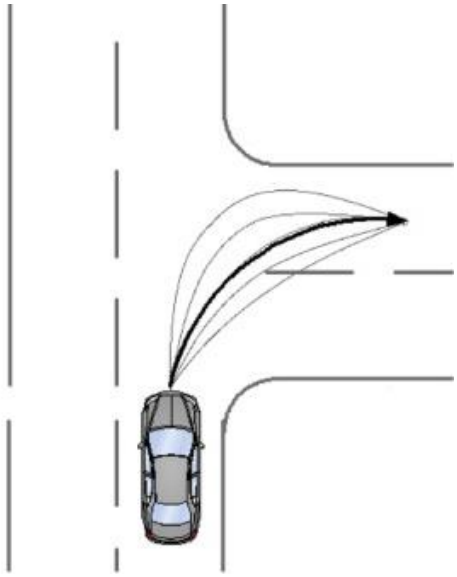

Figure 2.21 Driving a car as an example of an OCP. Find the controls (acceleration, wheel steer) to follow a defined trajectory (bold line) given the state of the car (position, orientation, speed).

2.6.1 Formalism

In the context of MBS, an optimal control problem is formulated as an optimization problem whose goal is to minimize an objective function $\boldsymbol{J}$. The solution to this objective function provides the

control trajectory $\boldsymbol{u}(t)$ and is guided by the state variables $\boldsymbol{x}(t)$ of the multibody system and by the algebraic variables $\boldsymbol{z}(t)$ of a given initial state (Eq. 2.19) to a final state (Eq. 2.20) inside a time horizon T (Figure 2.22). The OCP reads as follows:

$$\min_{\boldsymbol{x}(\boldsymbol{t}),\boldsymbol{u}(\boldsymbol{t}),\boldsymbol{z}(\boldsymbol{t})} J = \int_{\boldsymbol{0}}^{\boldsymbol{T}} \boldsymbol{L}\big(\boldsymbol{x}(t), \boldsymbol{u}(t), \boldsymbol{z}(t)\big) dt \tag{2.18}$$

subject to possible path constraints $\boldsymbol{c}$ such as:

$$\boldsymbol{x}(0) - \boldsymbol{x_i} = 0 \tag{2.19}$$

$$\boldsymbol{x}(T) - \boldsymbol{x_d} = 0 \tag{2.20}$$

$$\boldsymbol{c}(\boldsymbol{x}(t), \boldsymbol{u}(t), \boldsymbol{z}(t)) \geq 0 \tag{2.21}$$

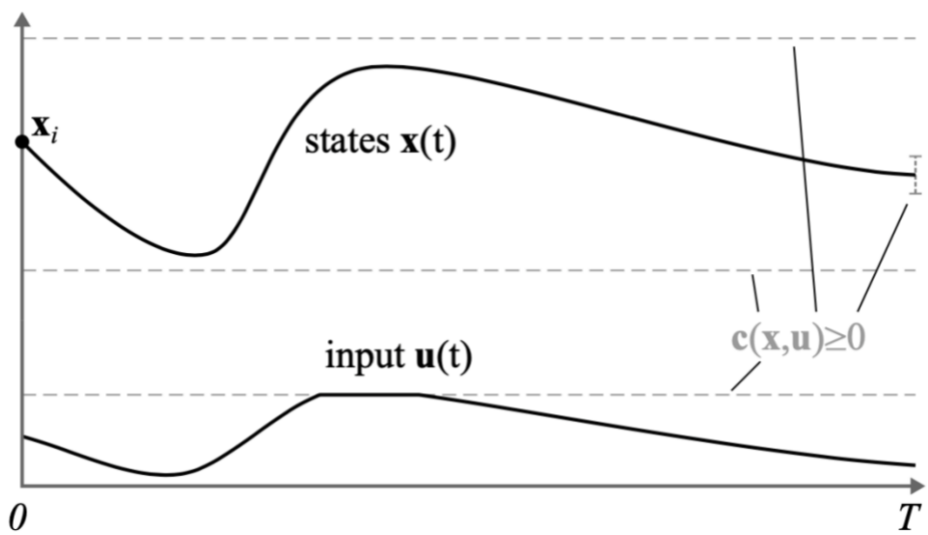

Figure 2.22 The continuous Optimal Control Problem [155]: Find the optimal state $\boldsymbol{x}(\boldsymbol{t})$ and control $\boldsymbol{u}(\boldsymbol{t})$ trajectory on the time interval [0, T], subject to path constraints $\boldsymbol{c}(\boldsymbol{x}, \boldsymbol{u}) \geq \boldsymbol{0}$.

The trajectory $\boldsymbol{x}(t)$, $\boldsymbol{z}(t)$ and the control variables $\boldsymbol{u}(t)$ are subjected to equality constraints $\boldsymbol{g}$, which correspond to the dynamics of the system and expressed as a set of differential algebraic equations (DAE).

$$\boldsymbol{g}\big(\boldsymbol{x}(t), \boldsymbol{u}(t), \boldsymbol{z}(t)\big): \begin{cases} \dot{\boldsymbol{x}} = \boldsymbol{f}(\boldsymbol{x}, \boldsymbol{u}, \boldsymbol{z}) \\ \boldsymbol{a}(\boldsymbol{x}, \boldsymbol{z}) = \boldsymbol{0} \end{cases} \quad t \in [0, T] \tag{2.22}$$

In Eq. 2.22, $\boldsymbol{f}$ and $\boldsymbol{a}$ respectively represent the differential and algebraic equations that describe the physics of the system in terms of the state variables $\boldsymbol{x}$, the algebraic variables $\boldsymbol{z}$, and the control variables $\boldsymbol{u}$. This formalism makes it possible to describe the dynamics of a multibody system as a

system of DAE. In general, no analytical solution exists for the optimization problem defined by Eq. 2.18.-2.22. However, the problem can be solved numerically by a discretization over the time interval [0, T]. The numerical approaches for solving an OCP are presented in the following section.

2.6.2 Solving an optimal control problem

There are three principal methods for numerically solving an OCP: dynamic programming, indirect methods, and direct methods. Among the three, direct methods are easier to implement and well adapted to MBS. In contrast, dynamic programming methods [157] are subject to the curse of dimensionality [158], which refers to a set of problems that arise when working with high-dimensional data. Therefore, it limits their use to small state spaces. Indirect methods [159], for their part, require the computation of the Hamiltonian derivative and are highly sensitive to initial values [160], which makes them difficult to implement.

2.6.2.1 Direct methods

The emergence of state-of-the-art non-linear programming solvers such as IPOPT [161] contributed to the efficiency and popularity of direct methods. IPOPT stands for Interior Point OPTimization and is an open-source software package for large-scale nonlinear optimization.

The direct methods consist in discretizing the time interval of the OCP, reducing it to a non-linear problem (NLP), which can afterwards be solved ("*first discretize, then optimize*"). The time interval $[0, T]$ is discretized into N time intervals $[t_k, t_{k+1}]$ so that $t_0 = 0$, $t_N = T$ and $k \in [0,1,2 \dots N-1]$. The time functions $\boldsymbol{x}(t)$, $\boldsymbol{z}(t)$ and $\boldsymbol{u}(t)$ in Eq. 2.18-2.22 are replaced by a sequence of $N+1$ discretized variables $\boldsymbol{x}_k$, $\boldsymbol{z}_k$ as well as N piecewise constant $\boldsymbol{u}_k$. In its discretized form (Figure 2.23), the OCP variables form the vector of decision variables $\boldsymbol{w} = \{\boldsymbol{x_0}, \boldsymbol{u_0}, \boldsymbol{z_0}, \dots, \boldsymbol{x_k}, \boldsymbol{u_k}, \boldsymbol{z_k}, \dots, \boldsymbol{x_{N-1}}, \boldsymbol{u_{N-1}}, \boldsymbol{z_{N-1}}\}$. The decision vector is used for the numerical approximation of the objective function P:

$$\min_{w} P(w) \tag{2.23}$$

Subject to path constraints reformulated according to the decision vector:

$$x_0 - x_i = 0 \tag{2.24}$$

$$x_N - x_T = 0 \tag{2.25}$$

$$c(w) \geq 0 \tag{2.26}$$

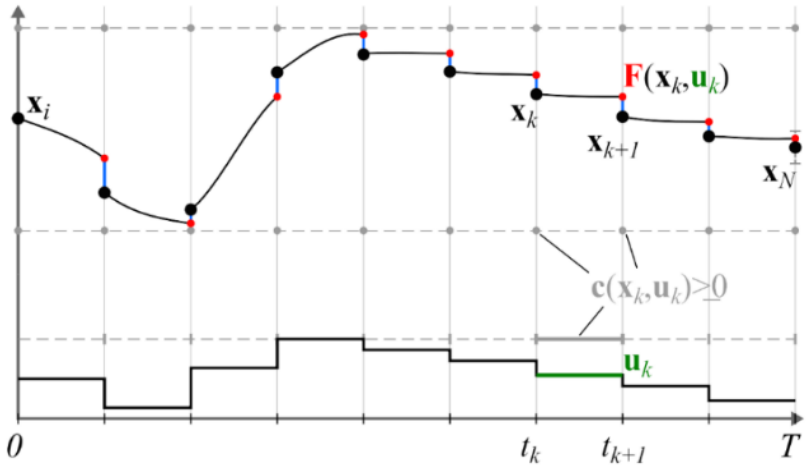

Figure 2.23 Optimal control problem with unsatisfied dynamic constraints [155]. The decision variables are the states at discretized points and the piecewise constant control variables.

To respect the dynamics of the system, the discretized control variable $\boldsymbol{u_k}$ is related to the two adjacent differential state variables $\boldsymbol{x_k}$ and $\boldsymbol{x_{k+1}}$ through an explicit numerical integration $\boldsymbol{F}$ of the continuous dynamics in the time interval $[\boldsymbol{t_k}, \boldsymbol{t_{k+1}}]$:

$$x_{k+1} - F(x_k, u_k, z_k) = 0 \tag{2.27}$$

Moreover, the differential and algebraic states, respectively x_k and z_k, are related to each discrete time step by a series of algebraic equations:

$$a(x_k, z_k) = 0 \tag{2.28}$$

The constraints imposed by Eq. 2.27-2.28 can be answered by single shooting [162], multiple shooting [163] or direct collocation [164]. The direct collocation method was preferred for this research project for its ability to treat unstable systems and handle path and terminal constraints robustly [165]. Moreover, since the human arm has a high number of DoF and its joints movement need to be constrained, the direct collocation is a logic choice.

This direct collocation method involves the definition of collocation points between $[\boldsymbol{t_k}, \boldsymbol{t_{k+1}}]$ where the state variables $\boldsymbol{x_k}$ must satisfy the dynamics of the system. This scheme involves additional variables (polynomial coefficients) and additional constraint equations. Briefly, the direct collocation discretizes the states $\boldsymbol{x}(t)$ and the controls $\boldsymbol{u}(t)$ on a grid of collocation points, which are then respectively approximated by Lagrange polynomials and by a piecewise constant

function [166]. The Radau time grid is used since it provides a collocation point at the start and end of each state [167]. The OCP, including discretization, collocation algorithm, and optimization framework, was implemented with CasADi [168], [169], a symbolic open-source tool for nonlinear optimization and algorithmic differentiation.

2.6.2.2 Weight selection in objective function

Most objective functions used in OCP are multi-objective. For biomechanics applications, this generally translates to a global objective function J that is defined with the weighted sum method:

$$\min_{x} J = \sum_{i=1}^{k} \omega_i F_i(x) \tag{2.29}$$

Where x are the variables of the OCP, k is number of objective functions and ω_i is the ith weight associated to the ith objective function F_i. Objective functions F_i used in OCP are diverse, such as tracking/minimizing the states/controls/forces. Typically, there is no single point that minimizes all objective functions simultaneously. Therefore, a solution point is defined as *Pareto optimal* if it is not possible to move from that point and improve at least one objective function without worsening another one [170]. The set of all *Pareto optimal* points is defined as the *Pareto optimal set* (Figure 2.24).

In the literature, the process that leads to weight selection is often done heuristically [14], e.g. in [163]–[167]. Therefore, one cannot confirm that the chosen weights produce a *Pareto optimal* solution. Moreover, if the weights are varied one at the time or without any methodological approach, one will miss the best weights combination if an interaction exists between the different objective functions [176].

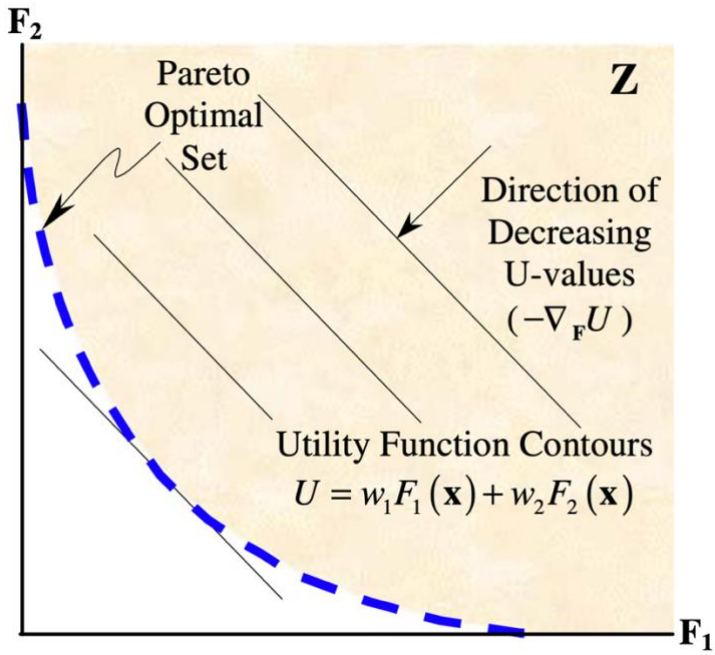

Figure 2.24 Representation of a Pareto optimal set (dashed blue line) for a multi-objective optimization with two objective functions (F_1 and F_2) [177].

A possible approach that can be implemented in weight selection is the response surface methodology (RSM). RSM allows to produce precise maps of a process based on mathematical models to reach peak performance [178]. The now-proven strategy of experimentation behind RSM consists of 4 different phases (Figure 2.25): screening, characterization, optimization, and verification. The screening phase allows to identify the vital few factors that have a significant effect on the process analyzed. In the context of OCP, the screening phase can be ignored since the number of weights, i.e., factors, is low. The characterization phase allows to discover potential interactions between the different factors. A curvature test should be realized in the characterization phase to decide if an optimization is required. If the curvature test is significant, an optimization phase is recommended by applying RSM. The typical tools for RSM are the central composite design (CCD) and Box-Behnken design (BBD). Finally, the verification phase should confirm the model obtained in the optimization phase. This can be done by doing additional experiment at the recommended conditions, i.e., weight selection.

Another interesting approach for weight selection is that of using global optimisation techniques such as Genetic Algorithm (GA). GA is a method for solving optimization problems, either constrained or unconstrained, based on a natural selection process [179]. GA has been used for

numerous applications such as feature selection [180], hyperparameter optimization [181], image reconstruction [182], and decision support systems [1], [2]. In the context of OCP, GA could be used to identify the *Pareto optimal set* of weight that optimize the objective function J.

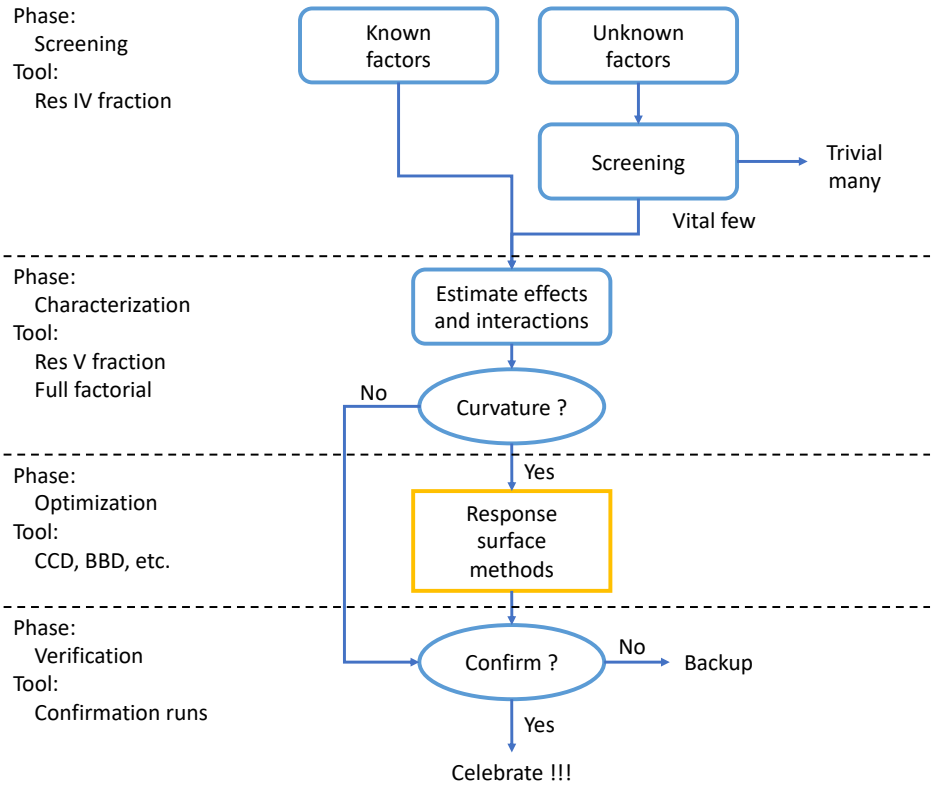

Figure 2.25 Four phases for a successful use of response surface methods: screening, characterization, optimization, and verification (Image reproduced from [178]).

Box 2.6 Optimal control: take home message

- Optimal control theory aims to find a control law for a dynamical system and is commonly used in biomechanics. An optimal control problem (OCP) is defined by separating variables as state or control and by describing the state using dynamic equations.
- Three methods are used to solve OCP: dynamic programming, indirect methods, and direct methods. The latter are widely spread for their ease of implementation, their computation efficiency, and the availability of state-of-the-art nonlinear programming solvers
- Direct methods discretize the OCP, reduce it to a non-linear problem, and then optimize it. In biomechanics, the direct collocation method is preferred for its ability to treat unstable systems and handle path and terminal constraints robustly.
- Most objective functions in OCP are multi-objective and follow a weighted sum formulation. However, there is minimal information in the literature on how to properly set each weight that is not based on trial-and-error. An approach based on response surface methods**,** or genetic algorithms could improve the weight selection process and therefore the performance of the OCP.

2.7 Thesis rationale

2.7.1 Problem

The following elements were highlighted, from the literature review, as gaps in the actual state of the art or needs for research and development:

Section 2.1: Research need: there exist multiple diagnoses that impair the upper limb, which is fundamental in multiple ADL. Since most diagnoses lead to progressive and irreversible deterioration of upper limb function, assistance devices are needed to help maintain independence in ADL.

Section 2.2: Active assistive exoskeletons show better potential for most upper limb impairments since they provide adjustable support in ADL. Nevertheless, their design is challenging due to constraints on size, weight, and functionality. Customization is generally needed to optimize usability and acceptability. A customization based on muscle forces could improve the functionality and safety of exoskeletons.

Section 2.3: The knowledge of muscle force distribution could help customize the dynamic support provided by exoskeletons to the user's need. However, the quantification of muscle forces is challenging since it requires to solve the muscle redundancy problem. While EMG-based methods provide physiologically coherent solutions, they are computationally heavy and require expensive equipment. Therefore, non-EMG-based methods should be preferred since they are easier to implement and do not rely on expensive equipment. Moreover, a recently developed non-EMG-based method show good coherence with EMG data in comparison to the commonly used non-EMG-based methods. However, this method has not yet been tested on dynamic movements of the upper limb.

Section 2.4: MBS are commonly used as a simulation tool in biomechanics. The human body, including its muscles, should be modeled as a closed-loop system to increase the biofidelity and performance of the model. Accurate modeling of muscle paths is important for precise computation of muscle moment arms. ROBOTRAN was chosen to model the upper limb. However, the muscles are not modelled on the available upper limb model from the research team.

Section 2.5: Exoskeletons are generally modeled as a closed-loop system with the human body. Body cuts are used to impose geometrical constraints to the human-exoskeleton system. Active exoskeleton introduces an additional redundancy problem. Different objective functions are used to solve this over-actuated system. The use of an objective function based on muscle forces could provide a more anatomically and physiologically coherent solution.

Section 2.6: Optimal control is widely spread in biomechanics. Most objective functions governing OCP follow a weighted sum formulation for multi-objective optimization. Information on how to set weights is limited and seems to rely on trial-and-error method, which lacks scientific rigor. Therefore, there is a need for a systematic method to identify optimal weights in a multi-objective optimization.

2.7.2 Research objectives

The global objective of this research project is to **develop a design tool to validate, through simulation, the performance of an exoskeleton based on the quantification of muscle forces**. This method was applied to E.FE as a benchmark-case. This general objective will be achieved by completing the following specific objectives (SO):

- **SO1**: Model the muscles on top of an existing osteoarticular multibody system of the upper limb.
- **SO2**: Implement a non-EMG-based method to quantify muscle forces during upper limb movements.
- **SO3**: Validate the performance of an exoskeleton during functional tasks through simulation.

CHAPTER 3 MUSCULOSKELETAL MULTIBODY MODEL OF THE UPPER LIMB

This chapter presents the integration of elbow muscles to an existing osteoarticular model of the upper limb using ROBOTRAN software. The musculoskeletal model is then validated through a comparison with the literature. The work presented demonstrates the achievement of **SO1**: Model the muscles on top of an existing osteoarticular multibody system of the upper limb.

3.1 Methodology

3.1.1 Data acquisition

The data from one healthy male subject (Age: 25, Mass: 90kg, Height: 1.93m) was extracted from the work of Blanchet et al. [14]. Additional subjects were supposed to be recruited for this Ph.D. thesis. However, the recruitment process was canceled due to the COVID-19 pandemic. The data acquisition process summarized in this section includes the extracted data for Chapter 4 and Chapter 5. The whole process is presented once to avoid unnecessary clutter.

Kinematics data were recorded by a 12-camera 3D motion analysis system (T40Sx VICON, Oxford) with a sampling frequency of 100 Hz. Twenty-nine (29) reflective markers were placed on the dominant upper limb of the subject, following the guidelines of Laitenberger et al. [27]. First, the data for the SCoRE and SARA methods were recorded to identify the centers of rotation (CoR) and axis of rotation (AoR) of the subject [183], [184]. Then, a movement of pure E.FE was recorded, as it is used to validate the musculoskeletal model (**SO1**) as well as to calibrate the muscle forces quantification process (**SO2**). Finally, the following 3 functional tasks were selected from the study by Rosen et al. [185]: Eat with a spoon (ES), Zip your coat (ZC), and Arm frontal reach (AR). These tasks were chosen to mimic ADL and to ensure a broad range of amplitudes for each upper limb joint. For each functional task, the muscle forces were quantified (**SO2** - Chapter 4), and the performance of an exoskeleton during these tasks was validated through simulation (**SO3** - Chapter 5). The user's relative coordinates were computed by minimizing the difference between the experimental 3D marker coordinates and the markers obtained by the forward kinematics function of the human multibody system. This kinematics identification process is detailed in [136].

3.1.2 Osteoarticular model

The osteoarticular model of the upper limb used in this study was originally developed in our laboratory by Laitenberger et al. [27] using the multibody modeling software ROBOTRAN [129], [132]. In this model, the forearm is considered as a closed-loop mechanism, which ensures the accuracy of elbow modeling and kinematic compatibility with the exoskeleton. The kinematic chain of the upper limb model (Figure 3.1) is composed of 7 rigid bodies and 23 DoF. The osteoarticular model allows for personalized joint CoR and AoR using the SCoRE and SARA functional methods [183], [184], [186]. This model will be referred as arm-only model (AOM).

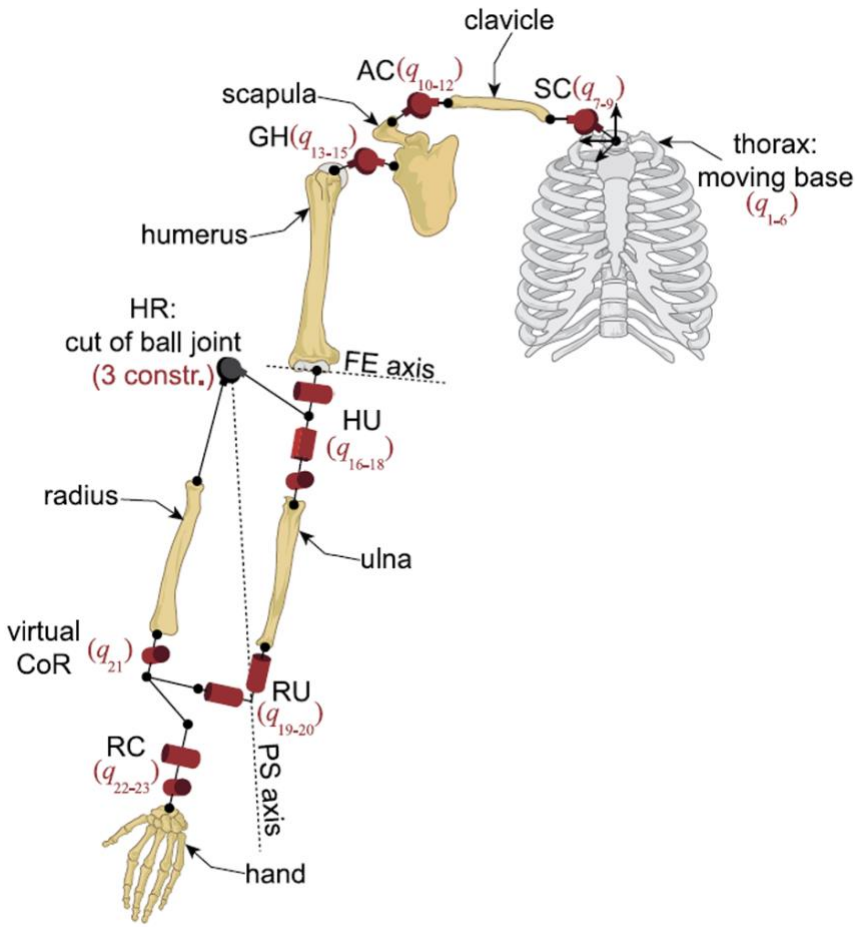

Figure 3.1 Kinematic chain of the human multibody model [27]. Sternoclavicular (SC) joint, acromioclavicular (AC) joint, glenohumeral (GH) joint, humeroulnar (HU) joint, radioulnar (RU) joint, virtual center of rotation (CoR), humeroradial (HR) joint, ball cut, and radiocarpal (RC) joint.

3.1.3 Muscles modeling

The main muscles responsible for E.FE were added to the existing AOM in ROBOTRAN. The BIC_{long}, the BIC_{short}, the *BRA*, and the *BRD* were modeled for their role in elbow flexion. The TRI_{long}, the TRI_{lat}, and the TRI_{med} were modeled for their role in elbow extension. The muscles were modeled following a via-points method [137] based on the anatomical data from Holzbaur et al. [99]. The spatial parameters of each via-points from the reference model were extracted and are available in Appendix C - Spatial parameters of the upper limb muscles.

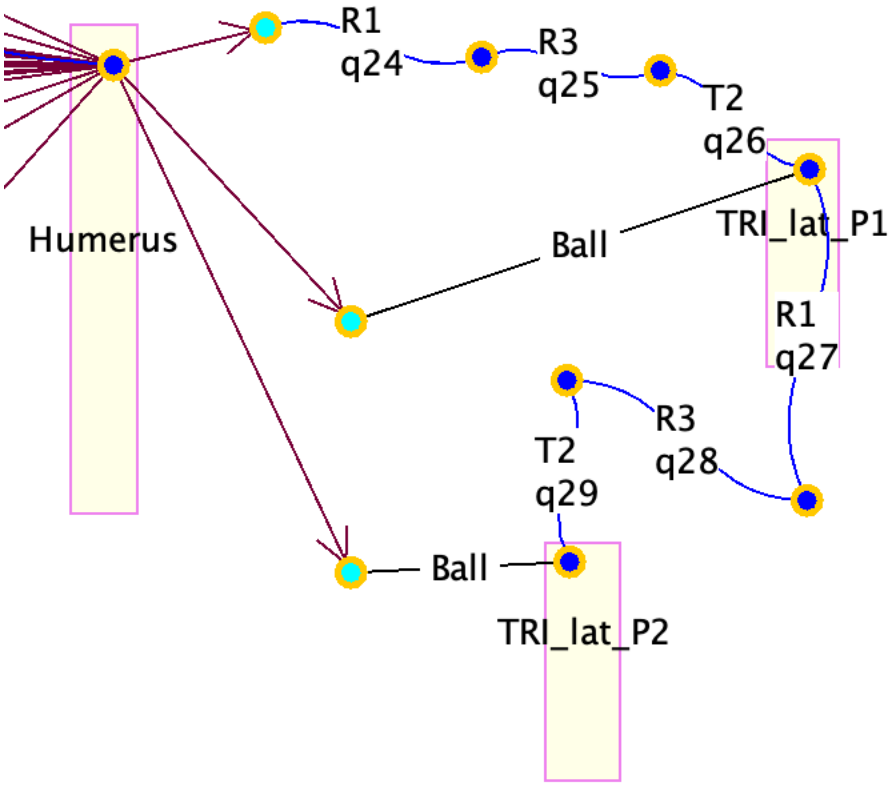

Figure 3.2 Modeling of the first two segments of the lateral head of the triceps brachii in ROBOTRAN with the via-points method. The via-points are represented by the green circles, defined as anchor points in ROBOTRAN. Each segment consists of a massless rigid body segment (TRI_lat_P1 and TRI_lat_P2) that has three degrees of freedom (R1, R3, and T2). A ball cut allows to “close the loop” between two via-points for each muscle segment by introducing three geometrical constraints.

The first step in ROBOTRAN was to model each via-point as an anchor point to the rigid body that represents the reference bone. An example is illustrated in Figure 3.2. The initial spatial parameters of each via-point were set to the values extracted from the reference model. Then, starting at the via-point that consisted of the muscle origin, a first muscle segment was modeled as a massless rigid body with three DoF, namely two rotations and one translation. The two rotations (R1 and R3 in Figure 3.2) allow for muscle orientation in the sagittal and frontal plane, while the translation (T2 in Figure 3.2) connects the muscle segment to the next via-point. A ball cut is used to "close the loop" between two via-points. Additional muscle segments were modeled the same way until all intermediary via-points were crossed and the insertion via-point was reached.

When the musculoskeletal model is used with actual recorded data from a subject, the initial spatial parameters are automatically scaled to match the subject's upper limb dimensions. This scaling step ensures that it will be possible to use the musculoskeletal model with different subjects. However, since the scaling process was tuned on only one subject, it might need some refinement to be used more broadly. Following this scaling step, the initial position of each degree of freedom for each muscle segment must be set manually so that ROBOTRAN is able to successfully "close the loop". Once done, the initial positions are saved to that the process does not need to be repeated. A 3D representation of the proposed model taken from ROBOTRAN is shown in Figure 3.3. This model will be referred as the arm and muscles model (AMM) for the remainder of this thesis.

Table 3.1 summarizes the number of via-points and segments for each upper limb muscle, as well as reference data for peak force, physiological cross-sectional area (PCSA), optimal fiber length, tendon slack length, pennation angle, and moment arm. While some of these physiological parameters are not needed for the quantification of muscle forces with a non-EMG-based method, they were still implemented in the developed model since they are needed when using an EMG-based method. This will allow the proposed model to be compatible with both methods of muscle forces quantification.

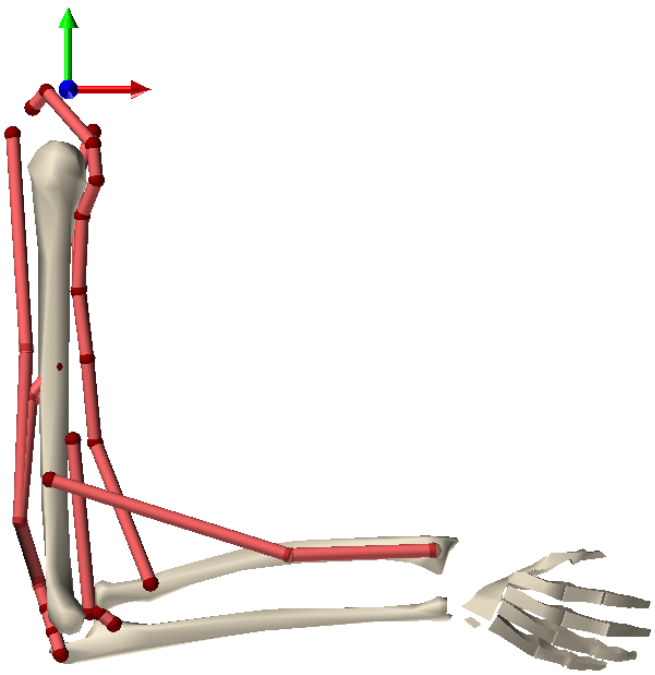

Figure 3.3 Representation in 3D of the arm and muscles model from ROBOTRAN. The elbow muscles are modeled with a via-points method. The global reference frame is included in the model: X (red), Y (green), and Z (blue).

Table 3.1 Muscles characteristics of the arm and muscles model: number of via-points, number of muscle segments, peak force, physiological cross-sectional area (PCSA). Reference values [99] for optimal fiber length, tendon slack length, pennation angle, and moment arm are also presented.

Muscle name	**# Via-points**	**# Segments**	**Peak force (N)**	**PCSA (cm^2)**	**Optimal fiber length (cm)**	**Tendon slack length (cm)**	**Pennation (°)**	**Moment arm (cm)**
Biceps Brachii								
Long head	6	6	624.3	4.5	11.6	27.2	0	3.6
Short head	3	3	436.6	3.1	13.2	19.2	0	3.6
Distal portion	3	2	1060.9*	-	-	-	-	-
Brachialis	4	3	987.3	7.1	8.6	5.4	0	1.8
Brachioradialis	3	2	261.3	1.9	17.3	13.3	0	5.7
Triceps Brachii								
Long head	3	2	798.5	5.7	13.4	14.3	12	-2.1
Lateral head	3	2	624.3	4.5	11.4	9.8	9	-2.1
Medial head	3	2	624.3	4.5	11.4	9.1	9	-2.1
Distal portion	3	2	2047.1*	-	-	-	-	-

*Corresponds to the sum of all head peak forces

3.1.4 Literature-based verification of the model

The AMM is validated by comparing the computed musculo-tendinous (muscle and tendon) lengths and muscle moment arms during a cycle of E.FE with reference values from the literature. The reference model of Holzbaur is available through OpenSim [99]. In the AMM, musculo-tendinous length for each muscle is computed as the sum of all its segments. The muscle moment arm for each muscle in the AMM is computed as the distance from the line of action of the muscle to the axis of E.FE.

In Holzbaur's model, the musculo-tendinous lengths are given as muscle fiber and tendon slack length, with the corresponding pennation angle. Based on the muscle representation of Figure 3.4, the reference musculo-tendinous length is computed as:

$$L^{MT} = L_s^T + L^M \cdot \cos(\alpha) \tag{3.1}$$

where L^{MT} is the musculo-tendinous length, L_s^T is the tendon slack length, L^M is the muscle fiber length, and α is the pennation angle. The reference values for musculo-tendinous lengths were then scaled with respect to the subject's arm length.

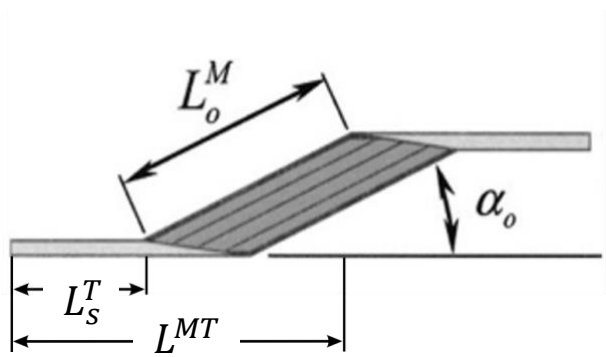

Figure 3.4 Muscle length representation

The muscle moment arms were given as is in the Holzbaur model and were also scaled with respect to the subject's arm length.

3.1.4.1 Performance criteria

The root mean square (RMS) error between the computed values of AMM and Holzbaur model is evaluated, in absolute ($RMSE$) and relative ($rRMSE$) terms [140]. $rRMSE$ is defined as the ratio of the $RMSE$ to RMS value of the computed data from the AMM.

3.2 Results

A visual comparison of the musculo-tendinous lengths between the proposed AMM and the reference model is presented in Figure 3.5. Table 3.2 presents the $RMSE$ on musculo-tendinous lengths as well as the $rRMSE$. The low $rRMSE$ (< 2.3%) for all muscles shows that the musculo-tendinous lengths computed from the AMM are consistent with the reference values from the literature, as seen visually in Figure 3.5. The low $RMSE$ and $rRMSE$ values show that the via-points modeling method in the AMM can accurately represent musculo-tendinous lengths.

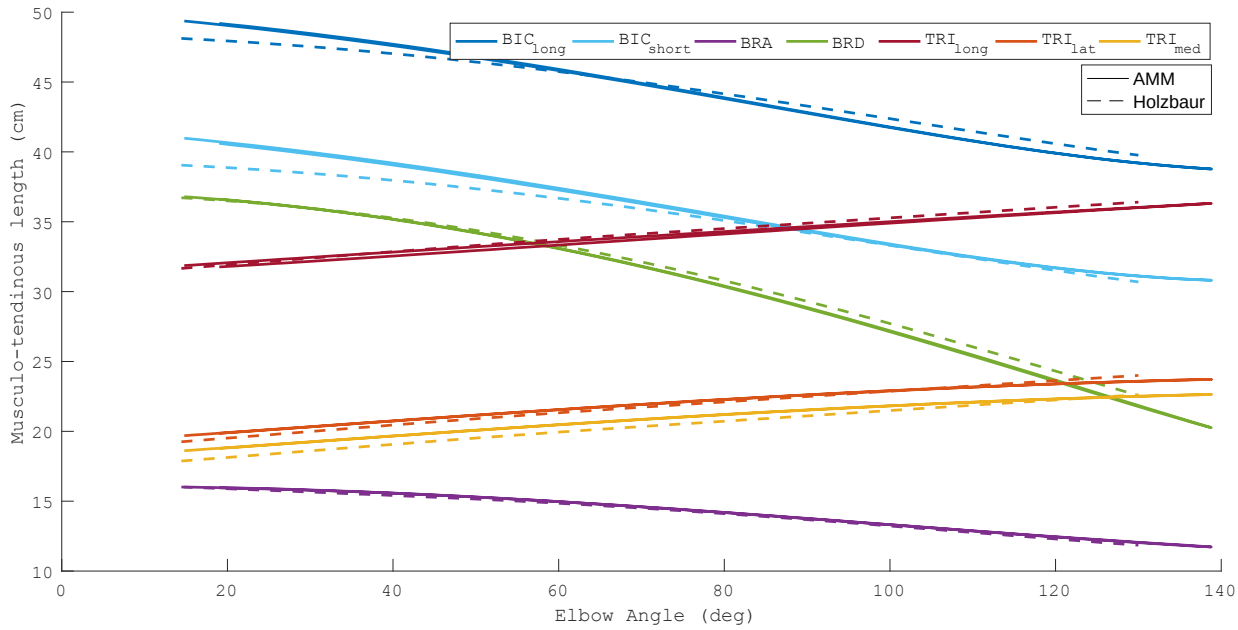

Figure 3.5 Musculo-tendinous length for each muscle computed from the arm and muscles model (AMM) and extracted from the literature (Holzbaur).

Table 3.2 $RMSE$ of the musculo-tendinous lengths between the arm and muscles model and the reference model for each muscle as well as the $rRMSE$.

	$\boldsymbol{RMSE}$ (cm)	$\boldsymbol{rRMSE}$ (%)
BIC_{long}	0.7	1.5
BIC_{short}	0.8	2.3
BRA	0.1	0.8
BRD	0.4	1.4
TRI_{long}	0.3	1.3
TRI_{lat}	0.2	1.1
TRI_{med}	0.5	2.3

A visual comparison of the muscle moment arms between the proposed AMM and the reference model is presented in Figure 3.6. Table 3.3 presents the $RMSE$ on muscle moment arms as well as the $rRMSE$. The $rRMSE$ on moment arms is lower for BIC and *BRD* (< 7.0%) than it is for *TRI* and *BRA* (< 21.4%). The higher $rRMSE$ for *TRI* and *BRA* is due to the presence of a plateau in the muscle moment arms of the reference model for an elbow angle respectively smaller that 40°, and higher than 80° (Figure 3.6). The $rRMSE$ for *BRA* and *TRI* decrease respectively to 2.3% and 3.4% if the values belonging to the plateau are ignored. The low $RMSE$ and $rRMSE$ values means that the muscle moment arms are physiologically coherent, which is important for accurate estimation of E.FE torque produced by the contraction of muscles.

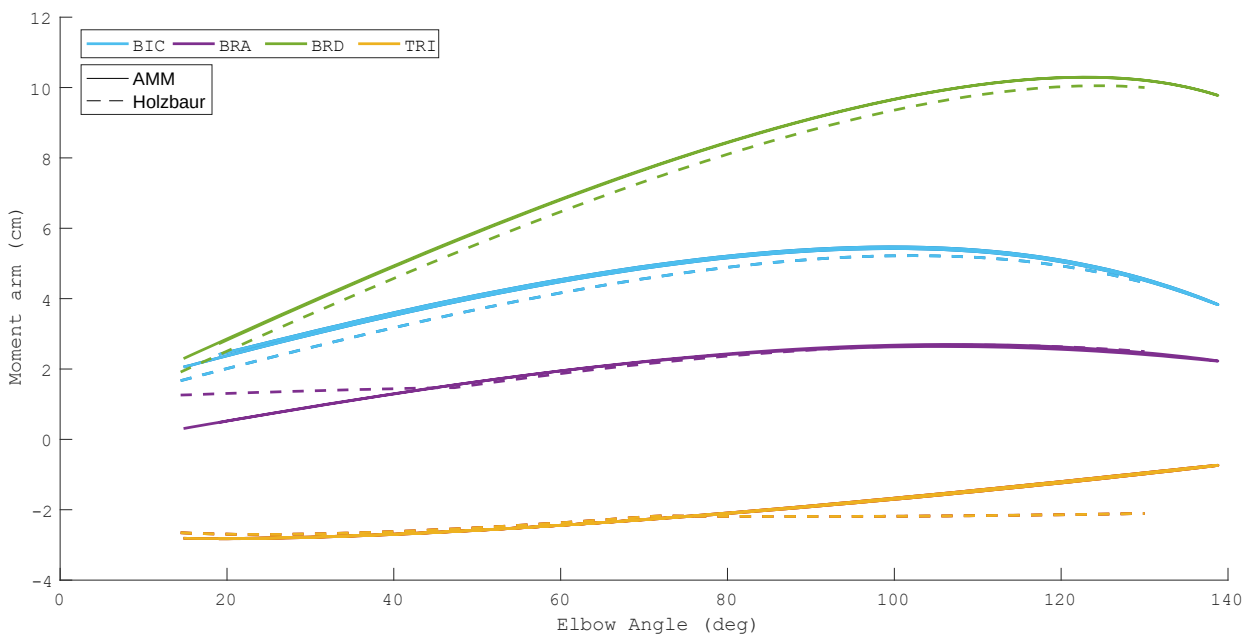

Figure 3.6 Moment arms for each muscle computed from the arm and muscles model (AMM) and extracted from the literature (Holzbaur).

Table 3.3 $RMSE$ of the muscle moment arms between the arm and muscles model and the reference model for each muscle as well as the $rRMSE$.

	$RMSE$ (cm)	$rRMSE$ (%)
BIC	0.3	7.0
BRA	0.3	14.5
BRD	0.3	4.4
TRI	0.5	21.4

3.3 Discussion

The **SO1** was to model the muscles on top of an existing osteoarticular multibody system of the upper limb, focusing on the movement of E.FE. The proposed AMM includes both heads of the *BIC*, the *BRA*, and the *BRD* as elbow flexors. The three heads of the *TRI* are included in the model as the elbow extensors. The geometrical muscle paths were extracted from anatomical data and modeled with a via-points method. The AMM was validated by comparing computed musculo-tendinous lengths and moment arms with data reported in the literature.

The magnitudes of musculo-tendinous lengths and moment arms matched well with the reference model from literature. This result shows that it is not necessary to use complex modeling methods such as wrapping objects to obtain accurate musculo-tendinous lengths. The muscle moment arms for *BRA* and *TRI* showed highest error percentage with the reference model. However, this difference is explained by the presence of wrapping objects at the elbow joint for the Holzbaur model [99], while there are none in the AMM. Indeed, the wrapping objects in the Holzbaur model prevent the muscles from being too close to the elbow joint. This is equivalent to imposing a lower bound on the muscle moment arms, which can be seen in Figure 3.6 as the presence of a plateau for *BRA* and *TRI*.

The $rRMSE$ for musculo-tendinous lengths were all below 2.3%, which is in accordance with [187] who reported $rRMSE$ below 2.9%. The maximum $rRMSE$ for muscle moment arms was 21.4% for *TRI*. Even though this error can be explained by the absence of wrapping objects in the AMM, it is close to the inter-subject variability reported by [188], which can reach 18%. Nonetheless, the $rRMSE$ for moment arms is in accordance with [140] who reported a median $rRMSE$ of 13.3%.

CHAPTER 4 QUANTIFICATION OF MUSCLE FORCES

This chapter presents a method to determine the optimal objective function weights for the quantification of muscle forces. The quantification of muscle forces during three functional tasks is then realized with the determined optimal weights. The work presented demonstrates the achievement of **SO2**: Implement non-EMG-based methods to quantify muscle forces during upper limb movements.

4.1 Methodology

4.1.1 Optimal control problem definition

The overactuation problem introduced by the quantification of muscle forces is tackled with an OCP formulation.

4.1.1.1 Optimization variables

A forward dynamic formulation of the dynamics was used to solve the OCP. The state $\boldsymbol{x}(t)$ and control $\boldsymbol{u}(t)$ vectors are defined as:

$$\boldsymbol{x}(t) = [\dot{\boldsymbol{q}}_{\boldsymbol{u}}\ \boldsymbol{q}_{\boldsymbol{u}}] \tag{4.1}$$

$$\boldsymbol{u}(t) = \begin{cases} [\boldsymbol{Q}_{\boldsymbol{H}}] & (AOM) \\ [\boldsymbol{Q}_{\boldsymbol{H}}\ \boldsymbol{F}_{\boldsymbol{M}}] & (AMM) \end{cases} \tag{4.2}$$

where $\dot{\boldsymbol{q}}_{\boldsymbol{u}}$ and $\boldsymbol{q}_{\boldsymbol{u}}$ are respectively the generalized independent velocities and positions. The generalized torques in the human independent joints $\boldsymbol{Q}_{\boldsymbol{H}}$ are a control variable for both the AOM and AMM while the individual muscle forces actuating the elbow $\boldsymbol{F}_{\boldsymbol{M}}$ are only a control variable for the AMM. The initial values for the state variables $(\dot{\boldsymbol{q}}_{\boldsymbol{u}}, \boldsymbol{q}_{\boldsymbol{u}})$, are obtained by the kinematics identification process. The initial values for the generalized torques $\boldsymbol{Q}_{\boldsymbol{H}}$ are obtained by inverse dynamics. Finally, the initial value for each muscle force $\boldsymbol{F}_{\boldsymbol{M}}$ is assigned to 1% of its peak force (Table 3.1).

4.1.1.2 Objective function of the optimal control problem

The objective function for the optimization included three terms, the Trajectory, the Joint torques and the Muscle forces (Eq. 4.3). The Trajectory and Joint torques terms ensure that the user's joint

produce feasible and intuitive movements. The Muscle forces term allows to estimate the individual muscle forces of the elbow muscles. The global objective function is defined as follows:

$$\min_{Q_H\, F_m} \underbrace{p_T T}_{Trajectory} + \underbrace{p_Q Q}_{Joint\ torques} + \underbrace{p_{Mu} Mu}_{Muscle\ forces} \tag{4.3}$$

where p_T, p_Q, and p_{Mu} are the weighting factors. T is the squared error between the simulated data and the reference generalized positions (Eq. 4.4.), Q is the user's squared joint torques (Eq. 4.5), and Mu is either the Crowninshield (Cr), Forster (Fo), or Wen muscle cost function (Eq. 4.6), and are respectively computed as follows:

$$T = \sum_{j=1}^{N} \int_{t_j}^{t_{j+1}} \sum_{i=1}^{n} \left(\boldsymbol{q}_{u_{i,j_{Sim}}} - \boldsymbol{q}_{u_{i,j_{Ref}}} \right)^2 dt \tag{4.4}$$

$$\begin{aligned} Q &= \beta \sum_{j=1}^{N} \int_{t_j}^{t_{j+1}} \sum_{i=1}^{n} (\boldsymbol{Q}_{H_{i,j}} \cdot \boldsymbol{Q}_{H_{i,j}})\, dt \\ \beta &= \begin{cases} 1000 & if\ i = 9\ (\boldsymbol{Q}_{H,EFE}) \\ 1 & if\ i \neq 9\ (all\ other\ joints) \end{cases} \end{aligned} \tag{4.5}$$

$$Mu = \sum_{j=1}^{N} \int_{t_j}^{t_{j+1}} \Omega\, dt \tag{4.6}$$

where n is the number of independent actuated joints of the human, t_j is the time of collocation interval j, and N is the number of collocation intervals. The weighting factor β in Eq. 4.5 penalizes the use of non-physiological actuators [189] when muscle actuation is allowed. This ensures that the muscles are responsible for the joint movement, rather than the joint itself who could produce a torque. As a reminder, Ω is either defined as:

$$\text{Cr: } \Omega = \sqrt[2]{\sum_{k=1}^{M} \left(\frac{\boldsymbol{F}_{M_{k,j}}}{PCSA_k} \right)^2} \tag{4.7}$$

$$\text{Fo: } \Omega = \sum_{k=1}^{M} \left(\frac{\boldsymbol{F}_{M_{k,j}}}{F_{max_k}} - x_s \right)^2 ;\ x_s = 0.125 \tag{4.8}$$

$$\begin{aligned} \text{Wen: } \Omega &= \sqrt[3]{\sum_{k=1}^{M} \left(\frac{\boldsymbol{F}_{M_{k,j}} - \boldsymbol{x_s}\left(\boldsymbol{Q}_{H_{i,j}}\right)}{PCSA_k} \right)^3} ; \\ \boldsymbol{x_s}\left(\boldsymbol{Q}_{H_{E,j}}\right) &= 6.67 Q_{H_{E,j}} + 7.57 \end{aligned} \tag{4.9}$$

where M is the number of actuated muscles while $F_{\max_k}$ and $PCSA_k$ respectively are the peak force and the PCSA of the kth muscle. x_s is the co-contraction factor and is defined as a constant or as linear relationship with the elbow joint torque $Q_{H_{E,j}}$ for respectively Fo and Wen cost function. The value of the co-contraction factor for Fo cost function ($x_s = 0.125$) was chosen from the proposed values in Forster et al. [108] so that it was inside the range obtained by Wen et al. ($x_s \in [0.028, 0.172]$) [18].

4.1.2 Optimal weights selection for the objective function

The estimation of the optimal weights for the objective function is realized with the E.FE movement. The movement of E.FE is chosen for calibration since Wen cost function was calibrated during this same movement. The weights estimation was realized with a two steps process. In the first step, optimized values for p_T and p_Q are identified and compared with reference values from the literature. The optimization of p_T and p_Q is done with the AOM. Therefore, p_{Mu} is set to 0 since the individual muscle forces are not quantified. In the second step, the AMM is used to identify the optimized value for p_{Mu} for muscle forces quantification.

4.1.2.1 Optimization of p_T and p_Q

The optimization of p_T and p_Q was realized with two methods. Firstly, RSM is presented as a new approach to identify the optimal weights of an objective function with minimum runs instead of proceeding by trial-and-error. Secondly, GA is used as a comparison tool to confirm the validity of the optimal weights identified by RSM.

4.1.2.1.1 Response surface methodology

Figure 4.1 illustrates the process to obtain the optimal objective function weights. In the literature, values for p_T and p_Q vary respectively between [1, 10^9] and [10^{-6}, 1] [171], [173], [174], [190], [191]. Since this range is very large, the optimal weights were found by iterating through smaller design spaces. As a first iteration, the design space was initialized to its lowest values, [1, 10^2] and [10^{-6}, 10^{-4}], for respectively p_T and p_Q. A face-centered central composite design (FCD) with 5 center points is used since the number of factors is lower than 5 [178] (Figure 4.2).

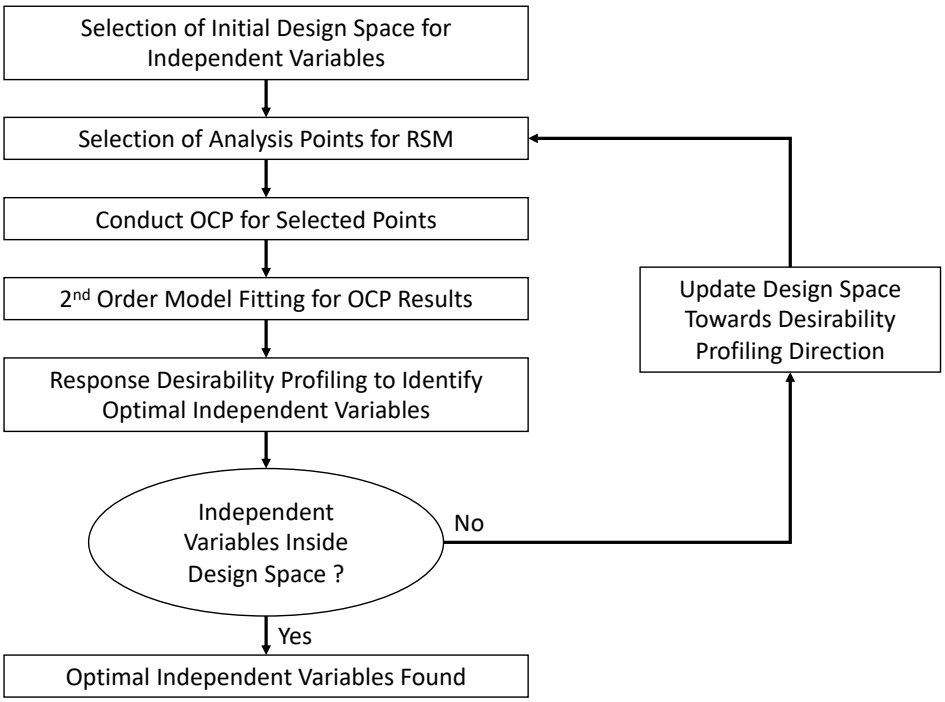

Figure 4.1 Process to obtain optimal objective function weights in an optimal control problem (OCP) using response surface methodology (RSM)

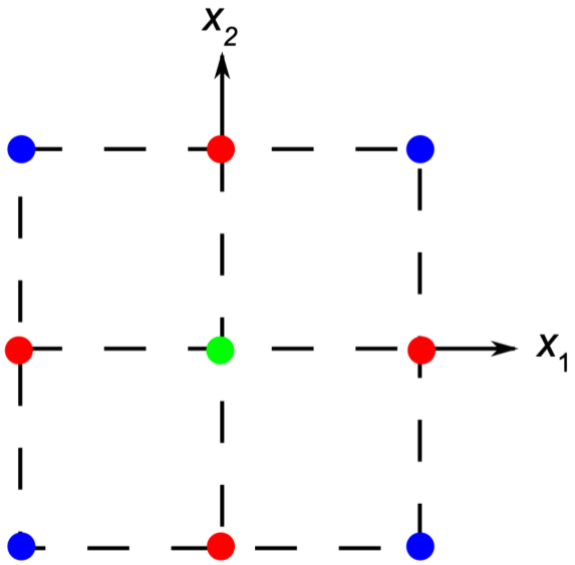

Figure 4.2 Face-centered central composite design for 2 factors. "cube" points (blue circles), axial points (red circles), and center point (green circle).

The analysis points for p_T and p_Q needed for the FCD are computed with Eq. 4.10 as follows:

$$X = \frac{X^* - a}{b - a}(\max X - \min X) + \min X \tag{4.10}$$

where X is the analysis point for p_T or p_Q, X^* is the coded value of p_T or p_Q, either -1, 0, or 1 in a FCD, a and b are respectively the lower and upper bound of the coded value (here ± 1), and $\max X$ and $\min X$ are respectively the upper and lower bound for p_T or p_Q. The OCP was solved for each analysis points. The response variables are the $RMSE$ on the end-effector's trajectory ($Traj$), i.e., the wrist, as well as the number of iterations (*iter*) to solve the OCP. The $RMSE$ is computed as:

$$RMSE_{traj} = RMS\left(\left\|Traj_{Sim} - Traj_{Ref}\right\|\right)\ [mm] \tag{4.11}$$

where *Sim* and *Ref* respectively denote the simulated values (obtained by the OCP), and the reference values (obtained by the kinematic identification). The FCD for the final design space is presented in Table 4.1.

RSM allows the modelling of a second-order equation that describes the OCP. To determine if a relationship exists between the independent and the response variables, the collected data is analyzed statistically using regression analyses. Each response variable is represented by a mathematical equation that correlates the response surface. The response variables are expressed as second-order polynomial equations (Eq. 4.12), where Y is the predicted response ($RMSE_{traj}$ or *iter*); *l* the number of independent variables; X_i the independent variables (p_T or p_Q); β_0 the constant coefficient, and β_i, β_{ij} and β_{ii} the coefficients of linear, interaction and quadratic term, respectively. The coefficient parameters were estimated using a regression analysis employing the software Statistica V14 (TIBCO Software Inc, CA, US).

$$Y = \beta_0 + \sum_{i=1}^{l} \beta_i X_i + \sum_{i=1}^{l} \sum_{j=i+1}^{l} \beta_{ij} X_i X_j + \sum_{i=1}^{l} \beta_{ii} {X_i}^2 \tag{4.12}$$

The regression models are first validated graphically by characterizing the nature of residuals of the models. A residual is defined as the difference between an observed value and its respective fitted value. Two different plots are used: residuals versus the fitted values and normal probability

plot. The second validation is done numerically by calculating the coefficient of determination (R^2) and adjusted R^2 (${R_{adj}}^2$) as shown in Eq. 4.13 and 4.14.

$$R^2 = 1 - \frac{SS_{residual}}{SS_{model} + SS_{residual}} \tag{4.13}$$

$${R_{adj}}^2 = 1 - \frac{n-1}{n-p}(1 - R^2) \tag{4.14}$$

Where SS is the sum of the squares, *n* the number of experiments, and *p* the number of predictors (term) in the model, not counting the constant term. Finally, the ANOVA of the models allow to identify the significant factors of the regression model and test the lack of fit of the models.

The optimal weights for the analyzed design space were estimated using the Response Desirability Profiling function of the software Statistica V14.0 (TIBCO Software Inc, CA, US). The design space of the independent variables was modified based on the following rules:

1. If the estimated optimal weight from Desirability Profiling is inside the design space, it is kept unchanged.
2. If the estimated optimal weight from Desirability Profiling is at a limit of the design space (maximum or minimum), a new design space is defined by multiplying or dividing the current one by a factor 10 respectively when the estimated optimal value is at the maximum or minimum of the design space.
3. However, if the estimated optimal weight is at a limit of the design but the desirability function value is greater than 0.9 for every value of the design space, it is kept unchanged.

When the design space is modified, a new FCD is realized with the updated design spaces. If no updates were made to both design spaces, the OCP is run with the estimated optimal weights from Desirability Profiling and a comparison between the values obtained by the regression models and the OCP is made. The similarity between the experimental and predicted data is calculated using the relative standard deviation (RSD) (Eq. 4.15). Data is considered similar with RSD values < 10 %.

$$\text{RSD} = \frac{Standard\ deviation\ between\ predicted\ and\ experimental\ values}{Mean\ values\ between\ predicted\ and\ experimental\ values} \cdot 100\ [\%] \tag{4.15}$$

4.1.2.1.2 Genetic algorithm

The Global Optimization toolbox in MATLAB is used for optimization using the *gamultiobj* function to identify the set of Pareto optimal solutions. MATLAB's *gamultiobj* function uses a controlled elitist GA (a variant of NSGA-II [192]). Like any other GA, this is based on the evolution of a population of individuals, each of which is a solution to the optimization problem.

The decision variables of the GA are the weighting factors (p_T and p_Q) of the OCP's objective function (Eq. 4.3) while the fitness functions are the previously defined $RMSE_{traj}$ (Eq. 4.11) and number of iterations. The lower and upper bounds of the decision variables p_T and p_Q are respectively set to [1, 10^9] and [10^{-6}, 1], which corresponds to the design space identified in the literature. The population size, generation limit, and stall generation limit are respectively set to 20, 200, and 50. All the other options were kept at their default values. The GA was run on MATLAB R2020b (Windows 10, Intel® Core™ i7-7820X, 3.60 GHz, 48.0 Go RAM).

4.1.2.2 Optimization of p_{Mu}

The optimization of p_{Mu} was realized with RSM instead of GA since RSM allowed to obtain the optimal values for p_T and p_Q way faster, while there was not a significant difference in response performance. For this second step of the weight selection process, the design space for p_T and p_Q is fixed to the final design space obtained in the first step, whereas the design space for p_{Mu} can vary. The process is repeated thrice, one for each muscle cost function: Cr, Fo, and Wen.

The weights p_T, p_Q and p_{Mu} were regarded as three independent variables whereas the previously defined $RMSE_{traj}$ and *iter* were considered as response. One additional response variable was also considered: the $rRMSE$ between the elbow joint torque (from inverse dynamics) and the muscle generated elbow torque (Eq. 4.16).

$$rRMSE_{\mathrm{Q}} = \frac{RMS\left(\boldsymbol{Q}_{H,E.FE} - \sum_{k=1}^{M} \boldsymbol{d}_k \cdot \boldsymbol{F}_{M_k}\right)}{RMS(Q_{H,E.FE})} \cdot 100 \text{ [\%]} \tag{4.16}$$

where $Q_{H,E.FE}$ is the elbow joint torque for FE from inverse dynamics, $\boldsymbol{d}_k$ is the kth muscle moment arm from the AMM, and $\boldsymbol{F}_{M_k}$the computed force for the kth muscle.

The upper bound for the initial design space of p_{Mu} was set as such that the magnitude of $p_{Mu}Mu$ was equal or higher than the observed lower bound of $p_Q Q$ (Eq. 4.3) from the FCD for the final design space of p_T and p_Q. To find the upper bound of p_{Mu}, weights p_T and p_Q were fixed at their estimated optimal value from RSM and p_{Mu} was iterated as a power of 10 until the above-mentioned condition was reached. The lower bound of the design space for p_{Mu} was then obtained by diving the upper bound by 100. A FCD with 5 center points is also used (Figure 4.3). The process from Figure 4.1 was then followed to estimate the optimal value of p_{Mu}.

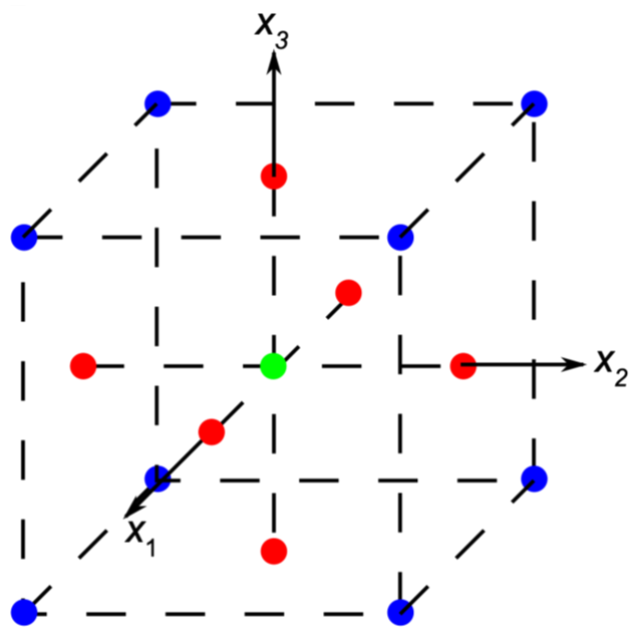

Figure 4.3 Face-centered central composite design for 3 factors. "cube" points (blue circles), axial points (red circles), and center point (green circle).

4.1.3 Muscle force quantification on functional tasks

The estimated optimal weights were used to quantify the muscle forces with each cost function during E.FE as well as the following functional tasks: ES, AR, and ZC. The previously defined response variables, $RMSE_{traj}$, *iter*, and $rRMSE_Q$ are evaluated for each task. The relative RMS of each muscle force ($rRMS_{F_M}$) is computed to show a relative percentage of the muscle activation during the movement. The $rRMS_{F_M}$ is computed as :

$$rRMS_{F_M} = \frac{RMS(\boldsymbol{F}_{M_k})}{F_{max_k}} \cdot 100 \text{ [\%]} \tag{4.17}$$

where F_{M_k} is the computed muscle forces during the movement analyzed and F_{max_k} is the maximum muscle force (Table 3.1) for the kth muscle.

4.2 Results

The following sections present the results of the estimation of optimal weights for p_T and p_Q (Section 4.2.1), and p_{Mu} (Section 4.2.2). Lastly, the muscle force quantification for three functional tasks is presented (Section 4.2.3).

4.2.1 Optimal weights for p_T and p_Q

4.2.1.1 Response surface methodology

The FCD and the results obtained, as well as the validation of the regression model (graphically and numerically) for the initial and intermediate design spaces are available at https://github.com/guigau17/PhD_StatisticaFiles to avoid unnecessary clutter. The analysis of the initial design space for p_T and p_Q, respectively $[10^0, 10^2]$ and $[10^{-6}, 10^{-4}]$, led to an intermediate design space of respectively $[10^1, 10^3]$ and $[10^{-6}, 10^{-4}]$. The final design space analyzed for p_T and p_Q was respectively $[10^2, 10^4]$ and $[10^{-6}, 10^{-4}]$. The FCD and the results obtained for the final design spaces are presented in Table 4.1. The graphical validation of the model for each response variable showed no anomality in the residual analysis (Figure 4.4).

Table 4.1 Face-centered central composite design of the final design space for p_T and p_Q and the experimental results for trajectory error ($RMSE_{traj}$) and number of iterations ($iter$). Experimental results are computed after solving the optimal control problem.

Run	Experimental Design		Results	
	p_T	p_Q	$RMSE_{traj}$ (mm)	$iter$
1	10^2 (-1)	10^{-6} (-1)	0.75	426
2	10^2 (-1)	10^{-4} (1)	0.96	267
3	10^4 (1)	10^{-6} (-1)	0.75	99
4	10^4 (1)	10^{-4} (1)	0.85	106
5	10^2 (-1)	$5.1 \cdot 10^{-5}$ (0)	0.79	108
6	10^4 (1)	$5.1 \cdot 10^{-5}$ (0)	0.83	309
7	$5.1 \cdot 10^3$ (0)	10^{-6} (-1)	0.85	101
8	$5.1 \cdot 10^3$ (0)	10^{-4} (1)	0.75	102
9	$5.1 \cdot 10^3$ (0)	$5.1 \cdot 10^{-5}$ (0)	0.79	99
10	$5.1 \cdot 10^3$ (0)	$5.1 \cdot 10^{-5}$ (0)	0.79	99
11	$5.1 \cdot 10^3$ (0)	$5.1 \cdot 10^{-5}$ (0)	0.79	99
12	$5.1 \cdot 10^3$ (0)	$5.1 \cdot 10^{-5}$ (0)	0.79	99
13	$5.1 \cdot 10^3$ (0)	$5.1 \cdot 10^{-5}$ (0)	0.79	99

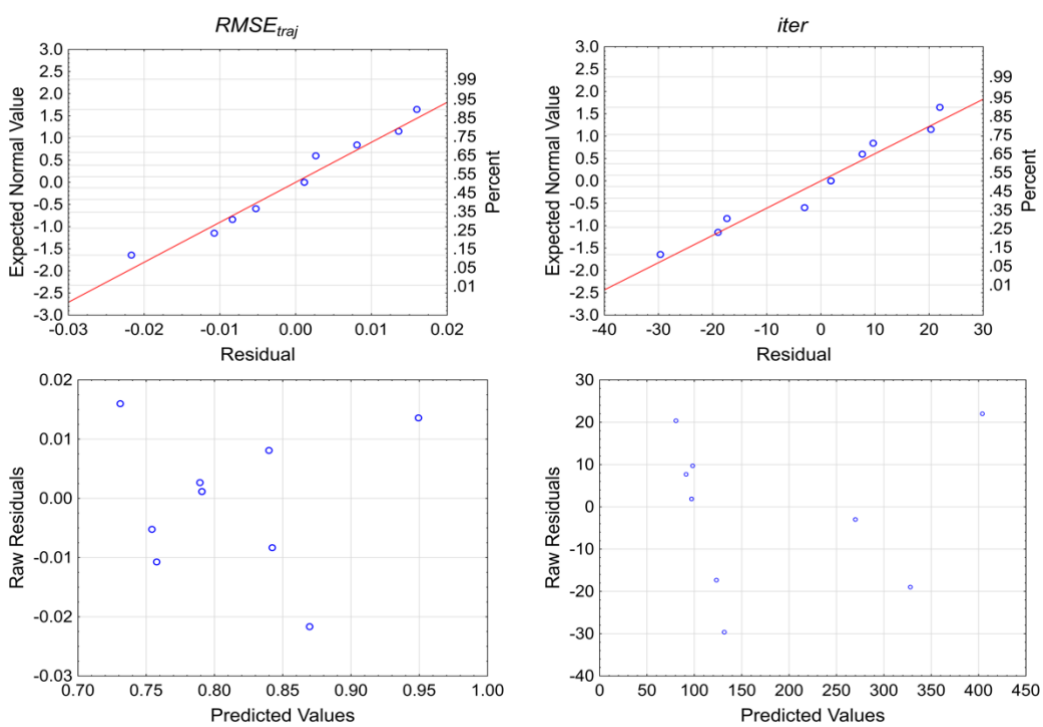

Figure 4.4 Normal probability plot of residuals (top line) and predicted vs residuals values plot (bottom line) for $RMSE_{traj}$ (left column) and $iter$ (right column).

The ANOVA (Table 4.2) indicated that the regression model was significative (p-value < 0.05). All independent variables were statistically significant, except for p_Q quadratic term. The lack of fit was not tested since the pure error of the OCP is 0. When the experimental variability is very low (pure error close to 0), the lack of fit test is always significant. However, it can be ignored if the R^2 and ${R_{adj}}^2$ are high [178], [193]. The values for R^2 and ${R_{adj}}^2$ are higher than 90% for both response models, indicating a good fit (Table 4.3). Furthermore, an ${R_{adj}}^2$ close to the R^2 value ensures a satisfactory adjustment of the quadratic model to the experimental data [194]. The quadratic models for $RMSE_{traj}$ and *iter* were constructed in terms of coded values for p_T and p_Q and are shown in Eq. 4.18 and 4.19 respectively.

Table 4.2 ANOVA for quadratic model of each of the final design space for p_T and p_Q. Significant variables (p-value < 0.05) are highlighted in bold.

Factor	SS	***df***	MS	F	p-value
$RMSE_{traj}$					
Model	$\mathbf{3.82 \cdot 10^{-2}}$	***5***	$\mathbf{7.64 \cdot 10^{-3}}$	$\mathbf{4.44 \cdot 10^{1}}$	***< 0.01***
$\boldsymbol{p_T}$	$\mathbf{4.21 \cdot 10^{-3}}$	**1**	$\mathbf{4.21 \cdot 10^{-3}}$	$\mathbf{2.45 \cdot 10^{1}}$	**< 0.01**
$\boldsymbol{{p_T}^2}$	$\mathbf{1.72 \cdot 10^{-3}}$	**1**	$\mathbf{1.72 \cdot 10^{-3}}$	$\mathbf{1.00 \cdot 10^{1}}$	**0.02**
$\boldsymbol{p_Q}$	$\mathbf{2.88 \cdot 10^{-2}}$	**1**	$\mathbf{2.88 \cdot 10^{-2}}$	$\mathbf{1.68 \cdot 10^{2}}$	**< 0.01**
${p_Q}^2$	$2.48 \cdot 10^{-4}$	1	$2.48 \cdot 10^{-4}$	$1.45 \cdot 10^{0}$	0.26817
$\boldsymbol{p_T \cdot p_Q}$	$\mathbf{3.19 \cdot 10^{-3}}$	**1**	$\mathbf{3.19 \cdot 10^{-3}}$	$\mathbf{1.86 \cdot 10^{1}}$	**< 0.01**
Residual	$1.20 \cdot 10^{-3}$	*7*	$1.72 \cdot 10^{-4}$		
Lack of Fit	$1.20 \cdot 10^{-3}$	3	$4.01 \cdot 10^{-4}$		
Pure Error	0	4	0		
iter					
Model	$\mathbf{1.27 \cdot 10^{5}}$	***5***	$\mathbf{2.55 \cdot 10^{4}}$	$\mathbf{6.81 \cdot 10^{1}}$	***< 0.01***
$\boldsymbol{p_T}$	$\mathbf{7.91 \cdot 10^{4}}$	**1**	$\mathbf{7.91 \cdot 10^{4}}$	$\mathbf{2.12 \cdot 10^{2}}$	**< 0.01**
$\boldsymbol{{p_T}^2}$	$\mathbf{3.72 \cdot 10^{4}}$	**1**	$\mathbf{3.72 \cdot 10^{4}}$	$\mathbf{9.94 \cdot 10^{1}}$	**< 0.01**
$\boldsymbol{p_Q}$	$\mathbf{3.90 \cdot 10^{3}}$	**1**	$\mathbf{3.90 \cdot 10^{3}}$	$\mathbf{1.04 \cdot 10^{1}}$	**0.01**
${p_Q}^2$	$2.25 \cdot 10^{2}$	1	$2.25 \cdot 10^{2}$	$6.01 \cdot 10^{-1}$	0.46
$\boldsymbol{p_T \cdot p_Q}$	$\mathbf{6.89 \cdot 10^{3}}$	**1**	$\mathbf{6.89 \cdot 10^{3}}$	$\mathbf{1.84 \cdot 10^{1}}$	**< 0.01**
Residual	$2.62 \cdot 10^{3}$	*7*	$3.74 \cdot 10^{2}$		
Lack of Fit	$2.62 \cdot 10^{3}$	3	$8.72 \cdot 10^{2}$		
Pure Error	0	4	0		

$$RMSE_{traj} = 7.9{\cdot}10^{-1} - 2.7{\cdot}10^{-2}p_T + 2.5{\cdot}10^{-2}{p_T}^2 + 6.9{\cdot}10^{-2}p_Q + 9.5{\cdot}10^{-3}{p_Q}^2 - 2.8{\cdot}10^{-2}p_T p_Q \tag{4.18}$$

$$iter = 9.7{\cdot}10^{1} - 1.1{\cdot}10^{2}p_T + 1.2{\cdot}10^{2}{p_T}^2 - 2.6{\cdot}10^{1}p_Q + 9.0{p_Q}^2 + 4.2{\cdot}10^{1}p_T p_Q \tag{4.19}$$

Table 4.3 Coefficient of determination (R^2) and adjusted R^2 for the final quadratic models.

Model	$\boldsymbol{R^2}$	$\boldsymbol{{R_{adj}}^2}$
$RMSE_{traj}$	97.0%	94.9%
iter	98.1%	96.8%

The desirability functions are presented in Figure 4.5. The estimated optimal values for p_T and p_Q are respectively 0.26 and -0.7 in coded values, which corresponds to $6.3 \cdot 10^3$ and $1.6 \cdot 10^{-5}$. Table 4.4 presents the RSD between the experimental and predicted response variables with the estimated optimal weights. The predicted $RMSE_{traj}$ and *iter* are respectively 0.75 mm and 90, while the experimental values are 0.75 mm and 100. Therefore, the RSD is 0 % and 7.4% for respectively $RMSE_{traj}$ and *iter*. The small $RMSE_{traj}$ can be observed in Figure 4.6, where the simulated and experimental end-effector trajectory in the global reference frame are presented.

Table 4.4 Predicted response values from desirability functions and experimental values from OCP with estimated optimal values for p_T ($6.3 \cdot 10^3$) and p_Q ($1.6 \cdot 10^{-5}$).

	$\boldsymbol{RMSE_{traj}}$ (mm)	*iter*
Desirability Functions	0.75	90
OCP	0.75	100
RSD (%)	0	7.4

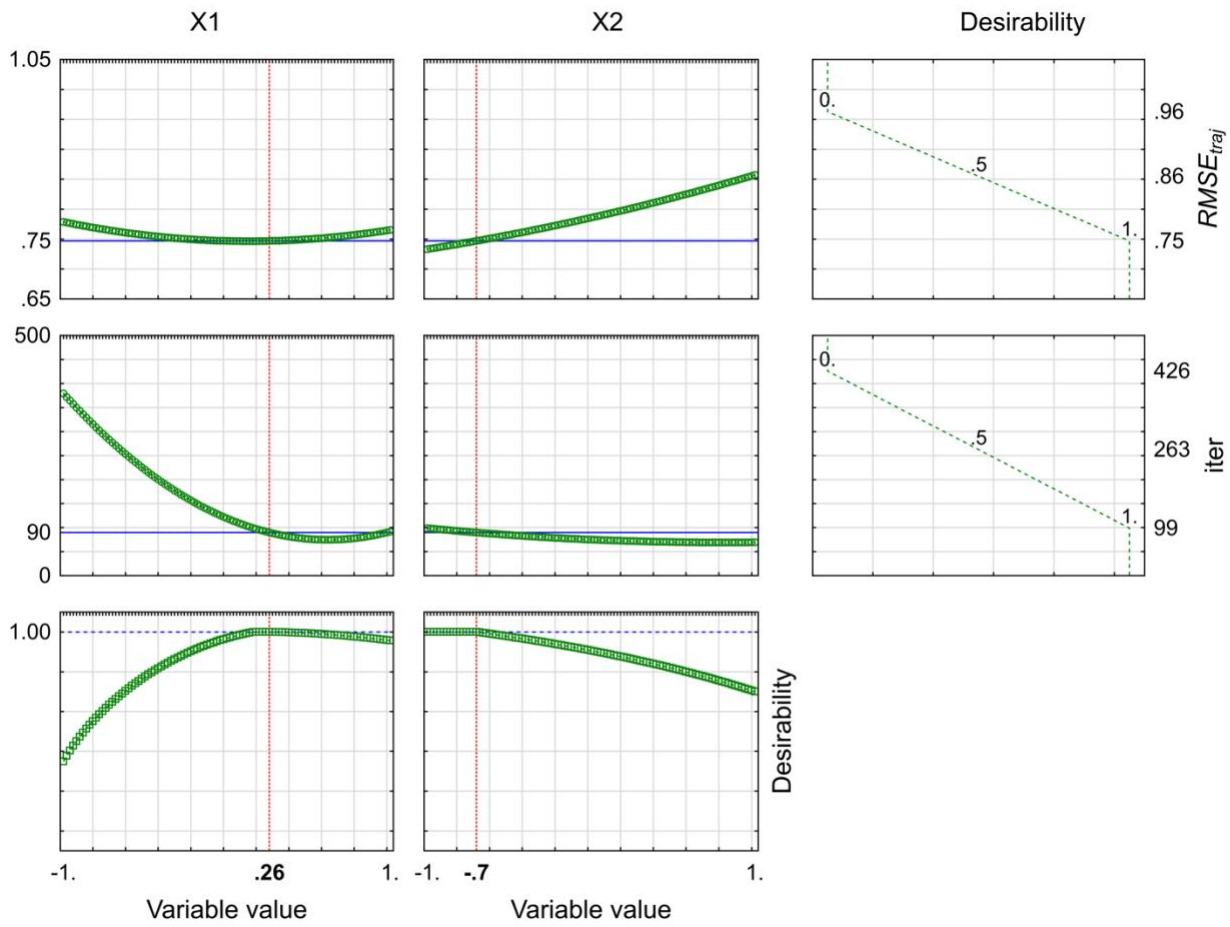

Figure 4.5 Profiles for predicted values and desirability function for $RMSE_{traj}$ and $iter$. Coded variables X1 and X2 are respectively for weights p_T and p_Q. Right column shows the desirability function for $RMSE_{traj}$ and $iter$. Red and blue line respectively indicate variable optimal value and predicted value at optimum.

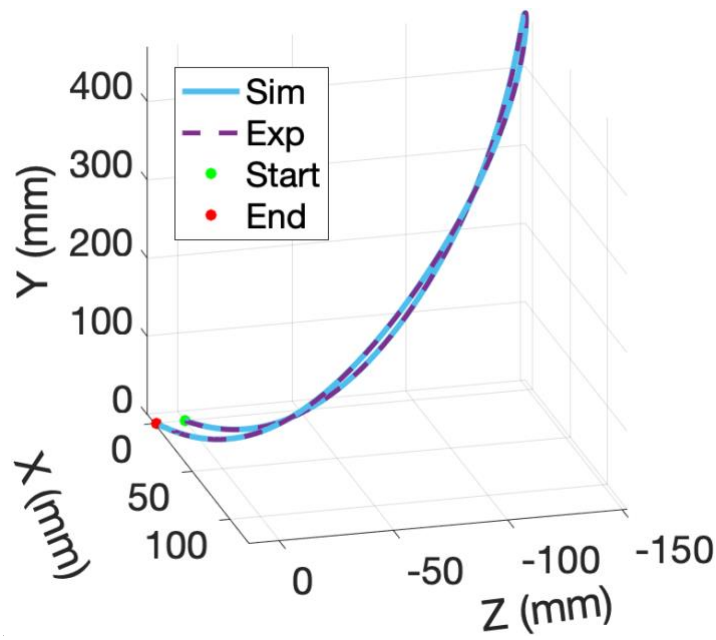

Figure 4.6 Simulated (blue) position of the hand during the E.FE movement with the estimated optimal values for p_T and p_Q. Experimental position is also shown (purple dashed).

4.2.1.2 Genetic algorithm

The GA identified a Pareto front with three unique combinations of p_T and p_Q after 8.8 days. The estimated optimal weight for p_T was identical, while the estimated optimal weight for p_Q showed small variations. Table 4.5 presents the estimated optimal values by GA with their respective response variables. $RMSE_{traj}$ was identical for all combinations (0.75 mm) while there was little variation for *iter* ([125 - 138]). The estimated optimal values for p_T and p_Q that minimized both response variables were respectively $6.3 \cdot 10^7$ and $1.9 \cdot 10^{-4}$.

Table 4.5 Estimated optimal value for p_T and p_Q by GA and their respective response variables.

p_T	p_Q	$RMSE_{traj}$ (mm)	*iter*
$6.3 \cdot 10^7$	$1.2 \cdot 10^{-4}$	0.75	137
$6.3 \cdot 10^7$	$1.9 \cdot 10^{-4}$	0.75	125
$6.3 \cdot 10^7$	$2.2 \cdot 10^{-4}$	0.75	138

4.2.2 Optimal weight for p_{Mu}

4.2.2.1 Identification of the initial design space

The lower bound for $p_Q Q$ observed in the FCD of the final design space for p_T and p_Q was $2.8 \cdot 10^{-4}$. The identification of the upper bound value for p_{Mu} for each cost function is presented in Table 4.6.

Table 4.6 Identification of the initial design space upper bound for p_{Mu}.Weights p_T and p_Q are set respectively to $6.3 \cdot 10^3$ and $1.6 \cdot 10^{-5}$, while $p_{Mu} Mu \geq (p_Q Q = 2.8 \cdot 10^{-4})$

Cost function	p_{Mu}	$p_{Mu} Mu$	Initial design space
Cr	10^{-7}	$4.4 \cdot 10^{-3}$	$[10^{-9}, 10^{-7}]$
Fo	10^{-1}	$9.9 \cdot 10^{-4}$	$[10^{-3}, 10^{-1}]$
Wen	10^{-7}	$2.8 \cdot 10^{-4}$	$[10^{-9}, 10^{-7}]$

4.2.2.2 Response surface methodology

The validation of the regression model for all cost functions is available online at https://github.com/guigau17/PhD_StatisticaFiles to avoid unnecessary clutter. For each cost function, the FCD, the coefficients of determination, the regression models, the desirability functions, and the validation with RSD are presented.

The FCD and the results of the OCP for Cr, Fo, and Wen cost function are respectively presented in Table 4.7, Table 4.8, and Table 4.9. The final design space for p_{Mu} was $[10^{-9}, 10^{-7}]$, $[10^{-5}, 10^{-3}]$, and $[10^{-9}, 10^{-7}]$ for respectively Cr, Fo, and Wen. The results for the initial ($[10^{-3}, 10^{-1}]$) and intermediate ($[10^{-4}, 10^{-2}]$) design space of p_{Mu} for Fo are available online at https://github.com/guigau17/PhD_StatisticaFiles.

Table 4.7 Face-centered central composite design of the final design space for p_T, p_Q, and p_{Mu} and the experimental results for trajectory error ($RMSE_{traj}$), number of iterations ($iter$), and muscle torque error ($rRMSE_Q$). Experimental results are computed after solving the optimal control problem with Crowninshield (Cr) cost function.

Muscle cost function: Cr						
Run	Experimental Design			Results		
	p_T	p_Q	p_{Mu}	$RMSE_{traj}$ (mm)	$iter$	$rRMSE_Q$ (%)
1	10^2 (-1)	10^{-6} (-1)	10^{-9} (-1)	0.75	322	4.0
2	10^4 (1)	10^{-6} (-1)	10^{-9} (-1)	0.75	164	4.1
3	10^2 (-1)	10^{-4} (1)	10^{-9} (-1)	0.95	346	3.9
4	10^4 (1)	10^{-4} (1)	10^{-9} (-1)	0.83	138	4.0
5	10^2 (-1)	10^{-6} (-1)	10^{-7} (1)	0.77	340	33.2
6	10^4 (1)	10^{-6} (-1)	10^{-7} (1)	0.77	149	33.2
7	10^2 (-1)	10^{-4} (1)	10^{-7} (1)	0.94	355	4.0
8	10^4 (1)	10^{-4} (1)	10^{-7} (1)	0.86	137	3.6
9	10^2 (-1)	$5.1 \cdot 10^{-5}$ (0)	$5.1 \cdot 10^{-8}$ (0)	0.83	336	3.6
10	10^4 (1)	$5.1 \cdot 10^{-5}$ (0)	$5.1 \cdot 10^{-8}$ (0)	0.79	151	3.4
11	$5.1 \cdot 10^3$ (0)	10^{-6} (-1)	$5.1 \cdot 10^{-8}$ (0)	0.76	143	16.6
12	$5.1 \cdot 10^3$ (0)	10^{-4} (1)	$5.1 \cdot 10^{-8}$ (0)	0.84	147	3.5
13	$5.1 \cdot 10^3$ (0)	$5.1 \cdot 10^{-5}$ (0)	10^{-9} (-1)	0.78	146	3.9
14	$5.1 \cdot 10^3$ (0)	$5.1 \cdot 10^{-5}$ (0)	10^{-7} (1)	0.82	139	3.5
15	$5.1 \cdot 10^3$ (0)	$5.1 \cdot 10^{-5}$ (0)	$5.1 \cdot 10^{-8}$ (0)	0.79	147	3.4
16	$5.1 \cdot 10^3$ (0)	$5.1 \cdot 10^{-5}$ (0)	$5.1 \cdot 10^{-8}$ (0)	0.79	147	3.4
17	$5.1 \cdot 10^3$ (0)	$5.1 \cdot 10^{-5}$ (0)	$5.1 \cdot 10^{-8}$ (0)	0.79	147	3.4
18	$5.1 \cdot 10^3$ (0)	$5.1 \cdot 10^{-5}$ (0)	$5.1 \cdot 10^{-8}$ (0)	0.79	147	3.4
19	$5.1 \cdot 10^3$ (0)	$5.1 \cdot 10^{-5}$ (0)	$5.1 \cdot 10^{-8}$ (0)	0.79	147	3.4

Table 4.8 Face-centered central composite design of the final design space for p_T, p_Q, and p_{Mu} and the experimental results for trajectory error ($RMSE_{traj}$), number of iterations ($iter$), and muscle torque error ($rRMSE_Q$). Experimental results are computed after solving the optimal control problem with Forster (Fo) cost function.

Muscle cost function: Fo						
Run	Experimental Design			Results		
	p_T	p_Q	p_{Mu}	$RMSE_{traj}$ (mm)	iter	$rRMSE_Q$ (%)
1	10^2 (-1)	10^{-6} (-1)	10^{-5} (-1)	0.75	356	7.6
2	10^4 (1)	10^{-6} (-1)	10^{-5} (-1)	0.75	199	5.8
3	10^2 (-1)	10^{-4} (1)	10^{-5} (-1)	0.95	340	4.3
4	10^4 (1)	10^{-4} (1)	10^{-5} (-1)	0.83	138	4.2
5	10^2 (-1)	10^{-6} (-1)	10^{-3} (1)	0.75	354	5.8
6	10^4 (1)	10^{-6} (-1)	10^{-3} (1)	0.75	230	5.9
7	10^2 (-1)	10^{-4} (1)	10^{-3} (1)	0.95	366	4.2
8	10^4 (1)	10^{-4} (1)	10^{-3} (1)	0.83	138	4.3
9	10^2 (-1)	$5.1 \cdot 10^{-5}$ (0)	$5.1 \cdot 10^{-4}$ (0)	0.83	278	4.3
10	10^4 (1)	$5.1 \cdot 10^{-5}$ (0)	$5.1 \cdot 10^{-4}$ (0)	0.78	137	4.4
11	$5.1 \cdot 10^3$ (0)	10^{-6} (-1)	$5.1 \cdot 10^{-4}$ (0)	0.75	171	5.8
12	$5.1 \cdot 10^3$ (0)	10^{-4} (1)	$5.1 \cdot 10^{-4}$ (0)	0.83	159	4.2
13	$5.1 \cdot 10^3$ (0)	$5.1 \cdot 10^{-5}$ (0)	10^{-5} (-1)	0.78	138	4.3
14	$5.1 \cdot 10^3$ (0)	$5.1 \cdot 10^{-5}$ (0)	10^{-3} (1)	0.78	152	4.4
15	$5.1 \cdot 10^3$ (0)	$5.1 \cdot 10^{-5}$ (0)	$5.1 \cdot 10^{-4}$ (0)	0.78	136	4.3
16	$5.1 \cdot 10^3$ (0)	$5.1 \cdot 10^{-5}$ (0)	$5.1 \cdot 10^{-4}$ (0)	0.78	136	4.3
17	$5.1 \cdot 10^3$ (0)	$5.1 \cdot 10^{-5}$ (0)	$5.1 \cdot 10^{-4}$ (0)	0.78	136	4.3
18	$5.1 \cdot 10^3$ (0)	$5.1 \cdot 10^{-5}$ (0)	$5.1 \cdot 10^{-4}$ (0)	0.78	136	4.3
19	$5.1 \cdot 10^3$ (0)	$5.1 \cdot 10^{-5}$ (0)	$5.1 \cdot 10^{-4}$ (0)	0.78	136	4.3

Table 4.9 Face-centered central composite design of the final design space for p_T, p_Q, and p_{Mu} and the experimental results for trajectory error ($RMSE_{traj}$), number of iterations ($iter$), and muscle torque error ($rRMSE_Q$). Experimental results are computed after solving the optimal control problem with Wen cost function.

Muscle cost function: Wen						
Run	Experimental Design			Results		
	p_T	p_Q	p_{Mu}	$RMSE_{traj}$ (mm)	iter	$rRMSE_Q$ (%)
1	10^2 (-1)	10^{-6} (-1)	10^{-9} (-1)	0.75	340	4.2
2	10^4 (1)	10^{-6} (-1)	10^{-9} (-1)	0.75	153	4.2
3	10^2 (-1)	10^{-4} (1)	10^{-9} (-1)	0.96	317	4.6
4	10^4 (1)	10^{-4} (1)	10^{-9} (-1)	0.85	135	5.3
5	10^2 (-1)	10^{-6} (-1)	10^{-7} (1)	0.99	382	27.8
6	10^4 (1)	10^{-6} (-1)	10^{-7} (1)	0.85	161	20.3
7	10^2 (-1)	10^{-4} (1)	10^{-7} (1)	0.98	608	4.3
8	10^4 (1)	10^{-4} (1)	10^{-7} (1)	0.86	159	3.6
9	10^2 (-1)	$5.1 \cdot 10^{-5}$ (0)	$5.1 \cdot 10^{-8}$ (0)	0.90	290	4.5
10	10^4 (1)	$5.1 \cdot 10^{-5}$ (0)	$5.1 \cdot 10^{-8}$ (0)	0.81	194	3.8
11	$5.1 \cdot 10^3$ (0)	10^{-6} (-1)	$5.1 \cdot 10^{-8}$ (0)	0.80	195	13.1
12	$5.1 \cdot 10^3$ (0)	10^{-4} (1)	$5.1 \cdot 10^{-8}$ (0)	0.84	171	3.8
13	$5.1 \cdot 10^3$ (0)	$5.1 \cdot 10^{-5}$ (0)	10^{-9} (-1)	0.80	145	5.4
14	$5.1 \cdot 10^3$ (0)	$5.1 \cdot 10^{-5}$ (0)	10^{-7} (1)	0.81	173	3.6
15	$5.1 \cdot 10^3$ (0)	$5.1 \cdot 10^{-5}$ (0)	$5.1 \cdot 10^{-8}$ (0)	0.80	192	3.8
16	$5.1 \cdot 10^3$ (0)	$5.1 \cdot 10^{-5}$ (0)	$5.1 \cdot 10^{-8}$ (0)	0.80	192	3.8
17	$5.1 \cdot 10^3$ (0)	$5.1 \cdot 10^{-5}$ (0)	$5.1 \cdot 10^{-8}$ (0)	0.80	192	3.8
18	$5.1 \cdot 10^3$ (0)	$5.1 \cdot 10^{-5}$ (0)	$5.1 \cdot 10^{-8}$ (0)	0.80	192	3.8
19	$5.1 \cdot 10^3$ (0)	$5.1 \cdot 10^{-5}$ (0)	$5.1 \cdot 10^{-8}$ (0)	0.80	192	3.8

The R^2 and ${R_{adj}}^2$ for all cost functions are presented in Table 4.10. The R^2 were higher than 90% while the ${R_{adj}}^2$ were higher than 80% for all response variables for each cost function. The highest values for both R^2 and ${R_{adj}}^2$ for Cr, Fo, and Wen were observed respectively for $RMSE_{traj}$, $iter$, and $RMSE_{traj}$. In contrast, the lowest values for both R^2 and ${R_{adj}}^2$ for Cr and Fo were observed respectively for $iter$ and $rRMSE_Q$. For Wen, the lowest values for R^2 and ${R_{adj}}^2$ were observed respectively for $iter$ and $rRMSE_Q$. These differences show that each cost function influence differently the precision and speed of the OCP.

Table 4.10 Coefficient of determination (R^2) and adjusted R^2 for the final quadratic models of each muscle cost function

	Model	$\boldsymbol{R^2}$ (%)	$\boldsymbol{{R_{adj}}^2}$ (%)
Cr	$RMSE_{traj}$	97.1	94.2
	iter	91.3	82.6
	$rRMSE_Q$	94.5	89.0
Fo	$RMSE_{traj}$	97.7	95.4
	iter	99.0	98.0
	$rRMSE_Q$	95.8	91.5
Wen	$RMSE_{traj}$	94.1	88.1
	iter	90.0	88.1
	$rRMSE_Q$	92.9	85.7

The constant, linear, interaction, and quadratic term coefficients of the second-order model for each cost function and response variables are presented in Table 4.11. The constant term coefficient is significant for all cost functions and second-order models. The linear term coefficient for p_T is significant for all cost functions and for second-order models of $RMSE_{traj}$ and $iter$. Linear term coefficient for p_Q is significant for all cost functions for the second-order model of $RMSE_{traj}$. Linear term coefficient for p_{Mu} is significant for Cr and Wen cost function for second-order model of $rRMSE_Q$. The observed differences for the significant independent variables (p_T, p_Q, and p_{Mu}) show that they each response variable is influenced differently both by the independent variables and the cost function used.

Table 4.11 Constant, linear, interaction, and quadratic term coefficient of the second-order models for Cr, Fo, and Wen cost function. Significant variables are highlighted in bold.

Cost function	Coefficient	$\boldsymbol{RMSE_{traj}}$	*iter*	$\boldsymbol{rRMSE_Q}$
Cr	Intercept	$\mathbf{7.9 \cdot 10^{-1}}$	$\mathbf{1.5 \cdot 10^{2}}$	$\mathbf{3.3}$
	p_T	$\mathbf{-2.4 \cdot 10^{-2}}$	$\mathbf{-7.4 \cdot 10^{1}}$	$-4.0 \cdot 10^{-2}$
	${p_T}^2$	$1.8 \cdot 10^{-2}$	$\mathbf{8.9 \cdot 10^{1}}$	$4.0 \cdot 10^{-1}$
	p_Q	$\mathbf{6.3 \cdot 10^{-2}}$	$2.3 \cdot 10^{1}$	$\mathbf{-7.2}$
	${p_Q}^2$	$5.7 \cdot 10^{-3}$	-9.7	**6.9**
	p_{Mu}	$\mathbf{9.7 \cdot 10^{-3}}$	$2.3 \cdot 10^{1}$	**5.8**
	${p_{Mu}}^2$	$9.2 \cdot 10^{-3}$	$-1.2 \cdot 10^{1}$	$6.0 \cdot 10^{-1}$
	$p_T p_Q$	$\mathbf{-2.4 \cdot 10^{-2}}$	$\mathbf{-3.7 \cdot 10^{1}}$	$-5.0 \cdot 10^{-2}$
	$p_T p_{Mu}$	$3.6 \cdot 10^{-3}$	$\mathbf{-3.3 \cdot 10^{1}}$	$-7.5 \cdot 10^{-2}$
	$p_Q p_{Mu}$	$-2.6 \cdot 10^{-3}$	$-2.7 \cdot 10^{1}$	$\mathbf{-7.3}$
Fo	Intercept	$\mathbf{7.8 \cdot 10^{-1}}$	$\mathbf{1.3 \cdot 10^{2}}$	$\mathbf{4.3}$
	p_T	$\mathbf{-2.9 \cdot 10^{-2}}$	$\mathbf{-8.5 \cdot 10^{1}}$	$-1.6 \cdot 10^{-1}$
	${p_T}^2$	$\mathbf{2.7 \cdot 10^{-2}}$	$\mathbf{7.9 \cdot 10^{1}}$	$1.1 \cdot 10^{-1}$
	p_Q	$\mathbf{6.4 \cdot 10^{-2}}$	$\mathbf{-1.7 \cdot 10^{1}}$	$\mathbf{-9.7 \cdot 10^{-1}}$
	${p_Q}^2$	$1.2 \cdot 10^{-2}$	$\mathbf{3.6 \cdot 10^{1}}$	$\mathbf{7.6 \cdot 10^{-1}}$
	p_{Mu}	0	$6.9 \cdot 10^{1}$	$-1.6 \cdot 10^{-1}$
	${p_{Mu}}^2$	$1.9 \cdot 10^{-3}$	$1.6 \cdot 10^{1}$	$1.1 \cdot 10^{-1}$
	$p_T p_Q$	$\mathbf{-3.0 \cdot 10^{-2}}$	$\mathbf{-1.9 \cdot 10^{1}}$	$2.1 \cdot 10^{-1}$
	$p_T p_{Mu}$	0	$8.8 \cdot 10^{-1}$	$\mathbf{2.6 \cdot 10^{-1}}$
	$p_Q p_{Mu}$	0	$-3.8 \cdot 10^{-1}$	$2.1 \cdot 10^{-1}$
Wen	Intercept	$\mathbf{8.0 \cdot 10^{-1}}$	$\mathbf{1.8 \cdot 10^{2}}$	$\mathbf{3.8}$
	p_T	$\mathbf{-4.6 \cdot 10^{-2}}$	$\mathbf{-1.1 \cdot 10^{2}}$	$-8.2 \cdot 10^{-1}$
	${p_T}^2$	$\mathbf{5.1 \cdot 10^{-2}}$	$\mathbf{8.0 \cdot 10^{1}}$	$2.7 \cdot 10^{-1}$
	p_Q	$\mathbf{3.7 \cdot 10^{-2}}$	$1.6 \cdot 10^{1}$	$\mathbf{-4.8}$
	${p_Q}^2$	$2.1 \cdot 10^{-2}$	$2.1 \cdot 10^{1}$	$\mathbf{4.6}$
	p_{Mu}	$\mathbf{3.8 \cdot 10^{-2}}$	$\mathbf{3.9 \cdot 10^{1}}$	$\mathbf{3.6}$
	${p_{Mu}}^2$	$1.0 \cdot 10^{-3}$	$-2.6 \cdot 10^{0}$	$6.2 \cdot 10^{-1}$
	$p_T p_Q$	$-1.2 \cdot 10^{-2}$	$-2.8 \cdot 10^{1}$	$9.4 \cdot 10^{-1}$
	$p_T p_{Mu}$	$-1.8 \cdot 10^{-2}$	$-3.8 \cdot 10^{1}$	-1.1
	$p_Q p_{Mu}$	$\mathbf{-3.9 \cdot 10^{-2}}$	$3.3 \cdot 10^{1}$	$\mathbf{-5.2}$

The desirability functions are presented in Figure 4.7, Figure 4.8 and Figure 4.9 respectively for Cr, Fo and Wen. The estimated optimal values for p_T, p_Q and p_{Mu} for Cr are respectively 0.46, -0.72 and -0.84 in coded values, which corresponds to $7.3 \cdot 10^{3}$, $1.5 \cdot 10^{-5}$ and $8.9 \cdot 10^{-9}$. The

estimated optimal values for p_T, p_Q and p_{Mu} for Fo are respectively 0.56, -0.02 and 0.06 in coded values, which corresponds to $7.8 \cdot 10^3$, $4.1 \cdot 10^{-5}$ and $8.0 \cdot 10^{-4}$. The estimated optimal values for p_T, p_Q and p_{Mu} for Wen are respectively 0.36, -0.34 and -0.82 in coded values, which corresponds to $6.8 \cdot 10^3$, $3.4 \cdot 10^{-5}$ and $9.9 \cdot 10^{-9}$.

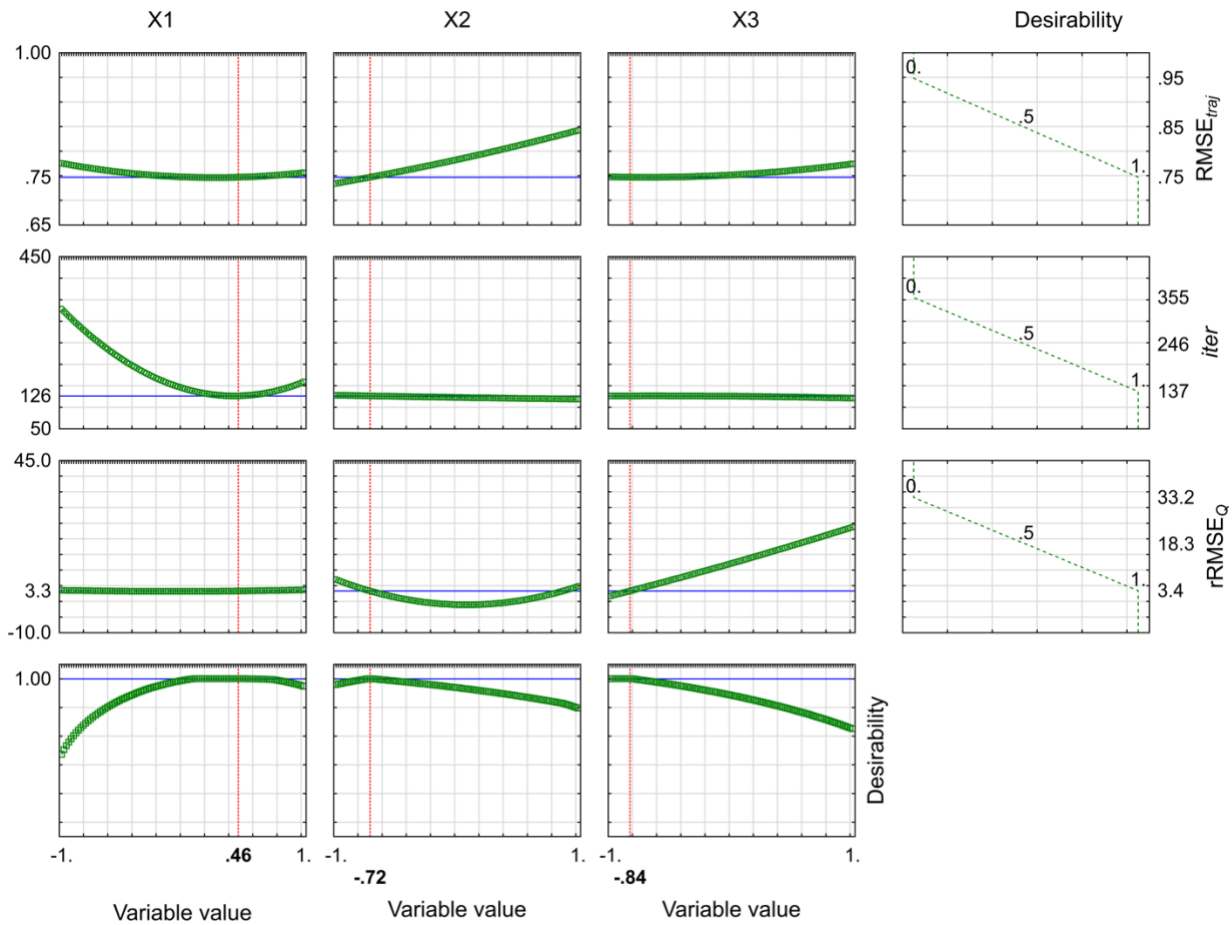

Figure 4.7 Profiles for predicted values and desirability function for $RMSE_{traj}$, $iter$, and $rRMSE_Q$ with the Crowninshield cost function. Coded variables X1, X2, and X3 are respectively for weights p_T, p_Q, and p_{Mu}. Right column shows the desirability function for $RMSE_{traj}$, $iter$, and $rRMSE_Q$. Red and blue line respectively indicate variable optimal value and predicted value at optimum.

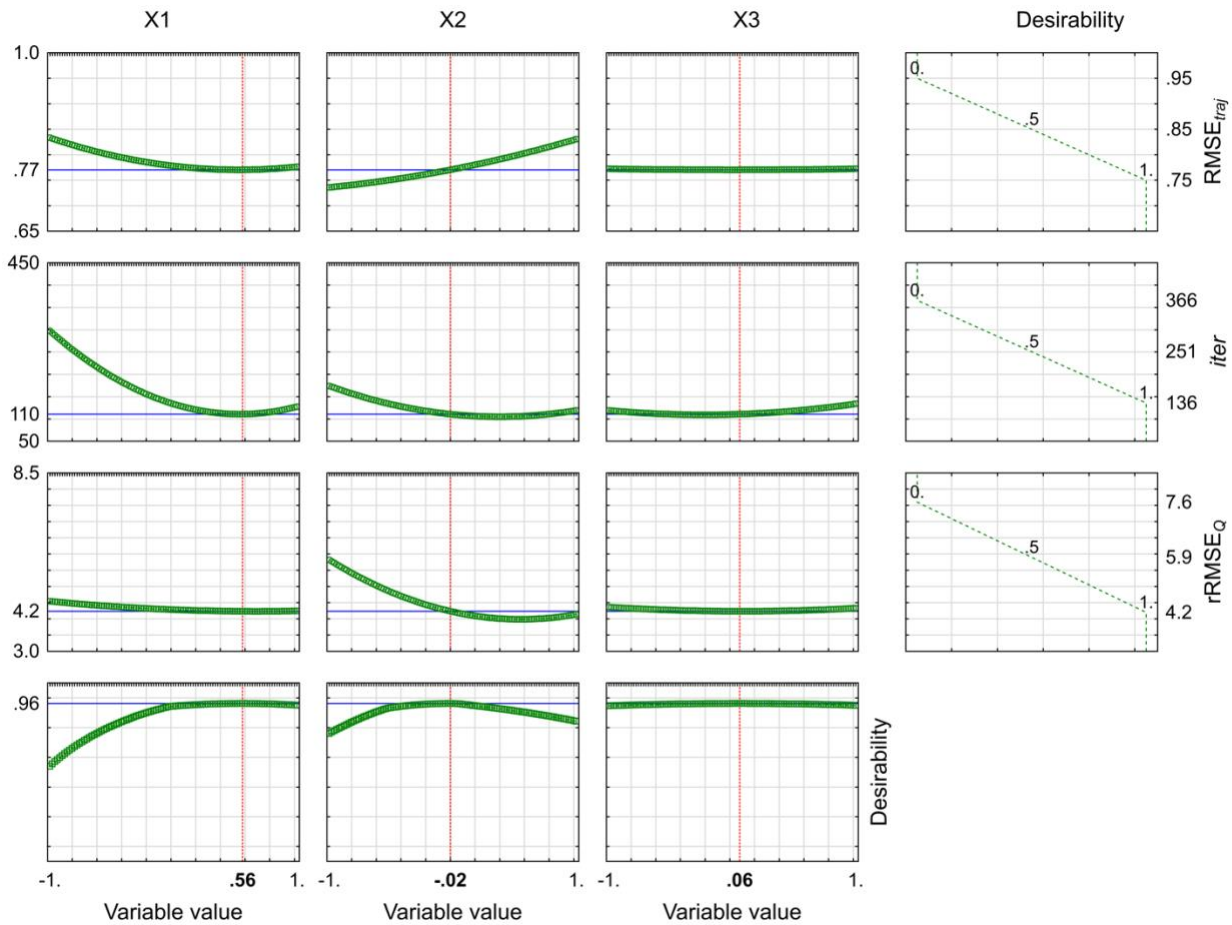

Figure 4.8 Profiles for predicted values and desirability function for $RMSE_{traj}$, $iter$, and $rRMSE_Q$ with the Forster cost function. Coded variables X1, X2, and X3 are respectively for weights p_T, p_Q, and p_{Mu}. Right column shows the desirability function for $RMSE_{traj}$, $iter$, and $rRMSE_Q$. Red and blue line respectively indicate variable optimal value and predicted value at optimum.

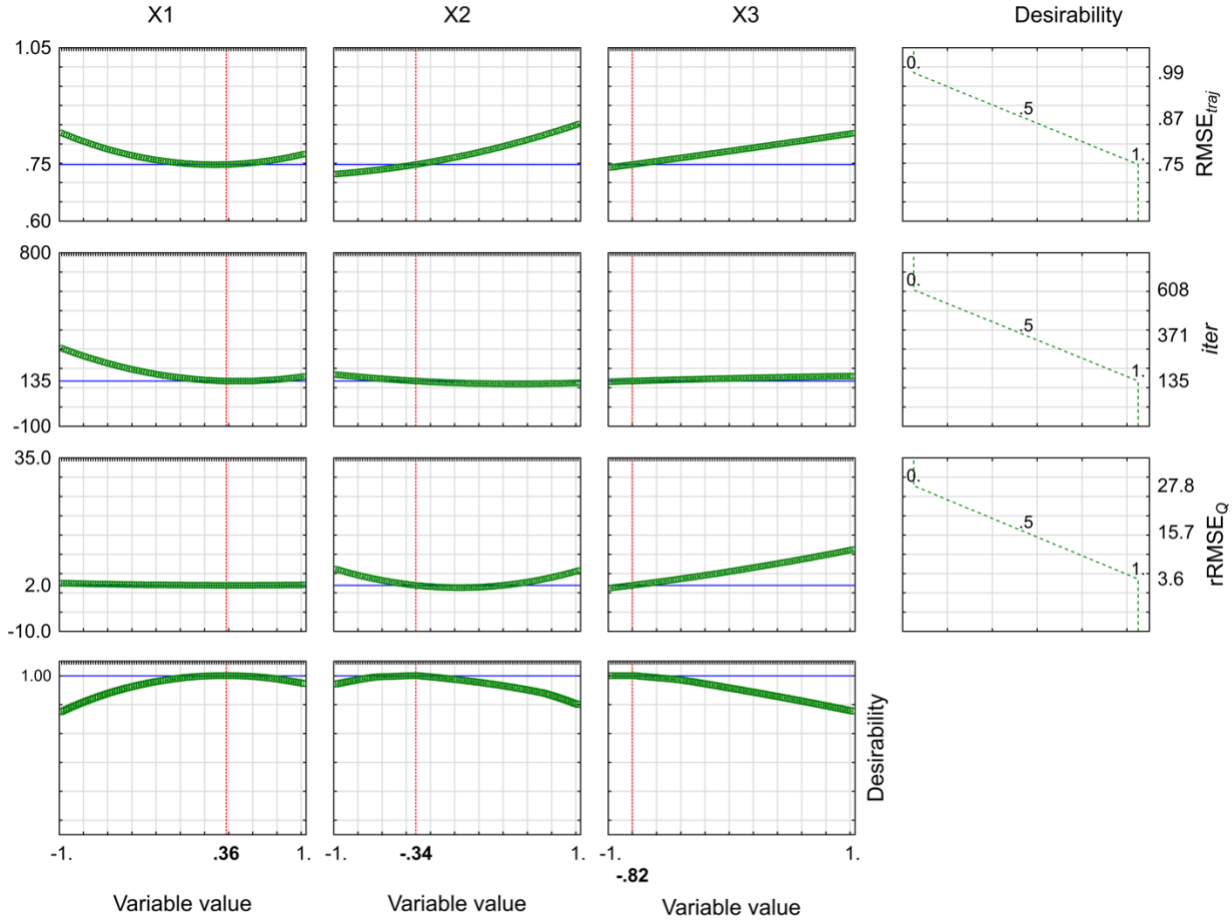

Figure 4.9 Profiles for predicted values and desirability function for $RMSE_{traj}$, $iter$, and $rRMSE_Q$ with the Wen cost function. Coded variables X1, X2, and X3 are respectively for weights p_T, p_Q, and p_{Mu}. Right column shows the desirability function for $RMSE_{traj}$, $iter$, and $rRMSE_Q$. Red and blue line respectively indicate variable optimal value and predicted value at optimum.

Table 4.12 presents the RSD between the experimental and predicted response variables with the estimated optimal weights for each cost function. The RSD for Cr is 0 %, 27.2% and 4.2% for respectively $RMSE_{traj}$, *iter* and $rRMSE_Q$. The RSD for Fo is 0 %, 20.8% and 3.3% for respectively $RMSE_{traj}$, *iter* and $rRMSE_Q$. Finally, the RSD for Wen is 0 %, 0% and 55.7% for respectively $RMSE_{traj}$, *iter* and $rRMSE_Q$. The lowest $RMSE_{traj}$ was 0.75mm, obtained for both Cr and Wen.

The OCP with Wen cost function was the fastest, solving in 135 iterations. The best $rRMSE_Q$ was 3.5% and was obtained with Cr cost function.

Table 4.12 Predicted response values from desirability functions and experimental values from OCP with estimated optimal values for p_T, p_Q, and p_{Mu}.

		$\boldsymbol{RMSE_{traj}}$ (mm)	*iter*	$\boldsymbol{rRMSE_Q}$ (%)
Cr	Desirability Functions	0.75	126	3.3
	OCP	0.75	186	3.5
	RSD (%)	*0*	*27.2*	*4.2*
Fo	Desirability Functions	0.77	110	4.2
	OCP	0.77	148	4.4
	RSD (%)	*0*	*20.8*	*3.3*
Wen	Desirability Functions	0.75	135	2.0
	OCP	0.75	135	4.6
	RSD (%)	*0*	*0*	*55.7*

As a summary, Table 4.13 presents the selected optimal values for p_T, p_Q and p_{Mu} used for muscle force quantification. The estimated optimal values for p_T and p_Q were different depending on the model used (AOM or AMM). However, all weights for p_T and p_Q were a power of respectively 10^3 and 10^{-5}.

Table 4.13 Optimal values for p_T, p_Q and p_{Mu}.

Model	$\boldsymbol{p_T}$	$\boldsymbol{p_Q}$	$\boldsymbol{p_{Mu}}$
AOM	$6.3 \cdot 10^3$	$1.6 \cdot 10^{-5}$	-
AMM – Cr	$7.3 \cdot 10^3$	$1.5 \cdot 10^{-5}$	$8.9 \cdot 10^{-9}$
AMM – Fo	$7.8 \cdot 10^3$	$4.1 \cdot 10^{-5}$	$8.0 \cdot 10^{-4}$
AMM – Wen	$6.8 \cdot 10^3$	$3.4 \cdot 10^{-5}$	$9.9 \cdot 10^{-9}$

4.2.3 Muscle force quantification

This section presents the results of muscle force quantification with the previously calibrated objective function for each muscle cost function. The quantification of muscle forces during E.FE is presented first (Section 4.2.3.1), as this movement was used during the calibration process. The quantification of muscle forces for the selected functional tasks (ES, ZC, AR) is then presented (Section 4.2.3.2).

4.2.3.1 Muscle forces: elbow flexion-extension

Figure 4.10A illustrates the computed E.FE torque with each muscle cost function as well as the reference elbow torque from inverse dynamics. All curves are similar, which is expected since the $rRMSE_Q$ were all below 5% with the estimated optimal weights (Table 4.12). Figure 4.10B, Figure 4.10C, and Figure 4.10D illustrates the individual muscle forces for respectively the Cr, Fo, and Wen cost function. Visually, the muscle forces obtained with Fo and Wen show the presence of co-contraction during the movement while it is absent for Cr. The notable differences in the estimation of muscle forces depending on the cost function represent well the muscle redundancy problem: multiple combinations of muscle forces produce the same resulting joint effort.

The $rRMS_{mf}$ (Table 4.14) were the lowest for BIC_{long} and BIC_{short} with Fo cost function and for BRA, BRD, TRI_{long}, TRI_{lat}, and TRI_{med} with Cr cost function. The highest $rRMS_{F_M}$ were observed with Wen cost function for all muscles except for BRD, whose highest value was observed with Fo cost function. Since co-contraction is included in Fo and Wen, the observation of the highest $rRMS_{F_M}$ values for all muscles is expected. However, it is surprising that the lowest $rRMS_{F_M}$ for BIC_{long} and BIC_{short} are observed with Fo. A high $rRMS_{F_M}$ for BRD with Fo cost function explains the lower values for BIC_{long} and BIC_{short}.

Table 4.14 $rRMS_{F_M}$ during E.FE movement for each muscle cost function

Cost function	$\boldsymbol{rRMS_{F_M}}$(%)						
	BIC_{long}	BIC_{short}	BRA	BRD	TRI_{long}	TRI_{lat}	TRI_{med}
Cr	3.7	3.7	2.3	3.9	1.1	1.1	1.1
Fo	2.4	2.4	4.8	12.5	7.6	7.7	7.7
Wen	3.9	3.9	5.0	10.7	10.6	10.8	10.8

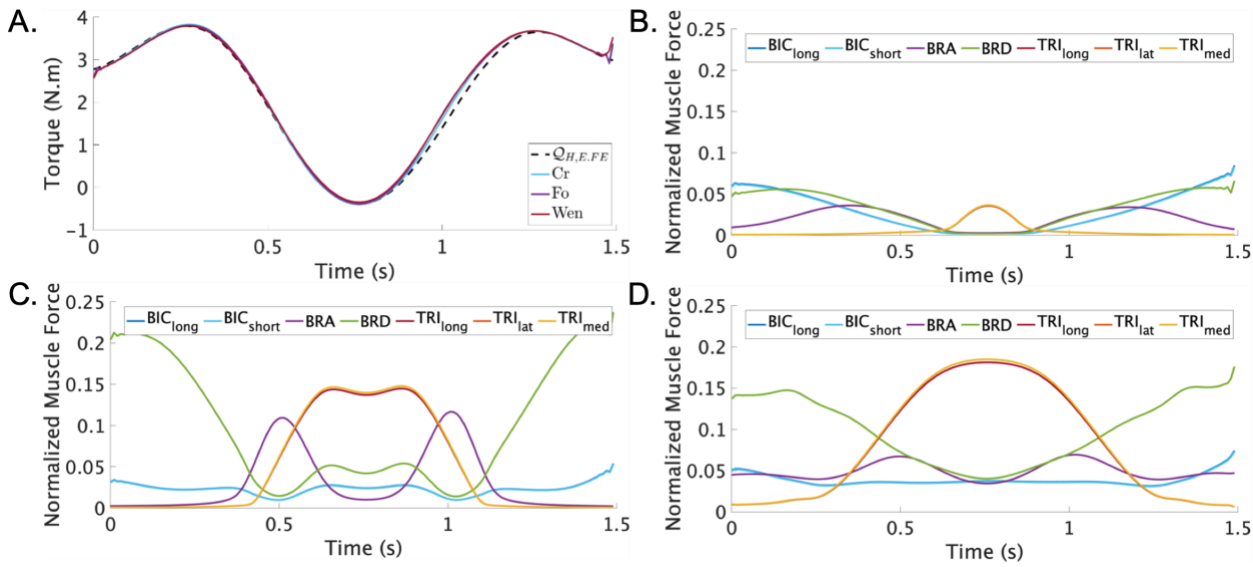

Figure 4.10 **A.** Computed E.FE torque with Crowninshield (light blue), Forster (purple), and Wen (red) cost function during E.FE movement. Elbow torque from inverse dynamics is plotted as reference (dashed line). Individual muscle forces estimated with **B.** Crowninshield, **C.** Forster, and **D.** Wen cost function

4.2.3.2 Muscle forces: functional tasks

Table 4.15 presents the results from OCP for each functional task and cost function with the optimal weights. The $RMSE_{traj}$ was below 1 mm for every task and cost function, which means that the OCP followed the experimental trajectory efficiently. The simulated trajectory from the OCP for ES, ZC, and AR can be observed respectively on Figure 4.11A, Figure 4.11B, and Figure 4.11C. The OCP for ZC was the fastest while it was the slowest for AR.

The $rRMSE_Q$ varied between task and the used cost function. The best result was observed for ES with Cr cost function (4.1 %), while the worst result was observed for AR with Fo cost function. Despite having the worst result for $rRMSE_Q$, all cost functions for AR gave a similar $rRMSE_Q$. In contrast, a ratio of 2 is observed between the highest and lowest $rRMSE_Q$ for ES and ZC. The $rRMSE_Q$ can be observed visually for ES, ZC, and AR in respectively Figure 4.12A, Figure 4.13A, and Figure 4.14A.

Table 4.15 Experimental values from OCP with optimal values of p_T, p_Q, and p_{Mu} for each functional movement (ES, ZC, AR) and each muscle cost function (Cr, Fo, Wen)

Task	Cost function	$\boldsymbol{RMSE_{traj}}$ (mm)	*iter*	$\boldsymbol{rRMSE_Q}$ (%)
ES	Cr	0.59	262	4.1
	Fo	0.61	268	4.4
	Wen	0.61	234	10.4
ZC	Cr	0.57	143	7.0
	Fo	0.58	145	13.5
	Wen	0.58	150	7.7
AR	Cr	0.79	723	12.8
	Fo	0.82	1250	14.6
	Wen	0.81	419	11.9

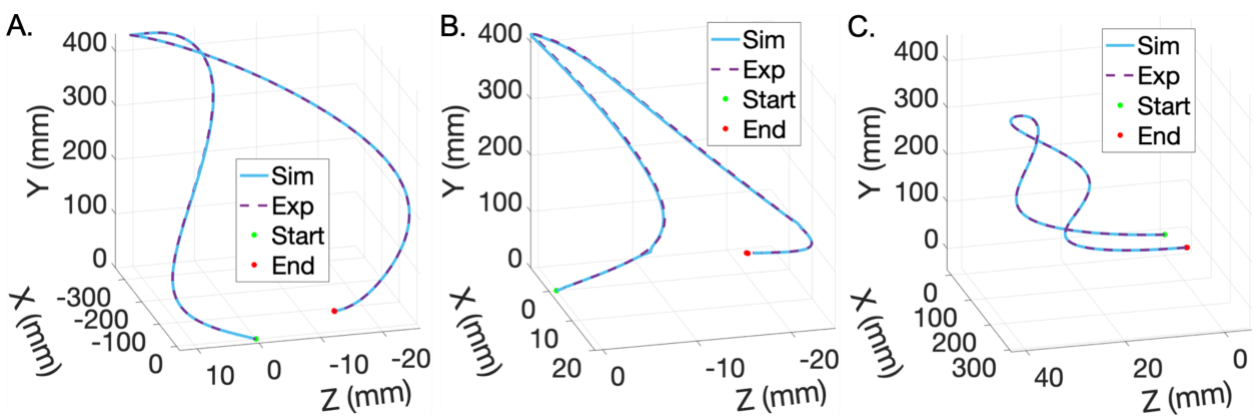

Figure 4.11 Simulated (blue) position of the hand during the **A.** ES, **B.** ZC, and **C.** AR functional task with the optimal values for p_T, p_Q, and p_{Mu}. Experimental position is also shown (purple dashed).

The estimated muscle forces for ES, ZC, and AR are respectively illustrated in Figure 4.12, Figure 4.13, and Figure 4.14. In each figure, the estimated muscle forces with Cr, Fo, and Wen are respectively presented in sub-figure B, C, and D. As it was observed for E.FE, almost no co-contraction is visible for Cr, while it is clearly present for Fo and Wen. The presence of co-contraction results in higher muscle forces for Fo and Wen. Indeed, the observed maximum normalized force is around 0.10 for all muscles and tasks when Cr is used while it reaches 0.3 and 0.4 for respectively Fo and Wen.

The $rRMS_{F_M}$ were the highest for all muscles during ES and ZC with respectively Wen and Fo. For AR, BIC_{long}, BIC_{short}, TRI_{long}, TRI_{lat}, and TRI_{med} showed the highest $rRMS_{F_M}$ with Wen while Fo gave the highest $rRMS_{F_M}$ for BRA and BRD. In general, the lowest $rRMS_{mf}$ were observed with Cr for all muscles, except for BIC_{long} and BIC_{short} during ES and AR.

Table 4.16 $rRMS_{F_M}$ during ES, ZC, and AR functional movement for each muscle cost function.

Task	Cost function	$\boldsymbol{rRMS_{F_M}}$ (%)						
		BIC_{long}	BIC_{short}	BRA	BRD	TRI_{long}	TRI_{lat}	TRI_{med}
ES	Cr	2.5	2.4	1.2	2.9	7.2	7.3	7.3
	Fo	2.3	2.2	3.8	8.1	16.0	16.4	16.4
	Wen	4.2	4.1	5.8	8.6	23.6	24.1	24.1
ZC	Cr	1.3	1.3	2.1	2.1	2.0	2.0	2.0
	Fo	2.3	2.2	17.7	2.8	22.5	23.0	23.0
	Wen	2.1	2.1	4.0	3.9	9.2	9.4	9.4
AR	Cr	2.4	2.4	2.0	2.7	0.3	0.3	0.3
	Fo	1.7	1.7	8.1	7.8	6.7	6.8	6.8
	Wen	3.4	3.4	5.2	7.6	8.1	8.3	8.3

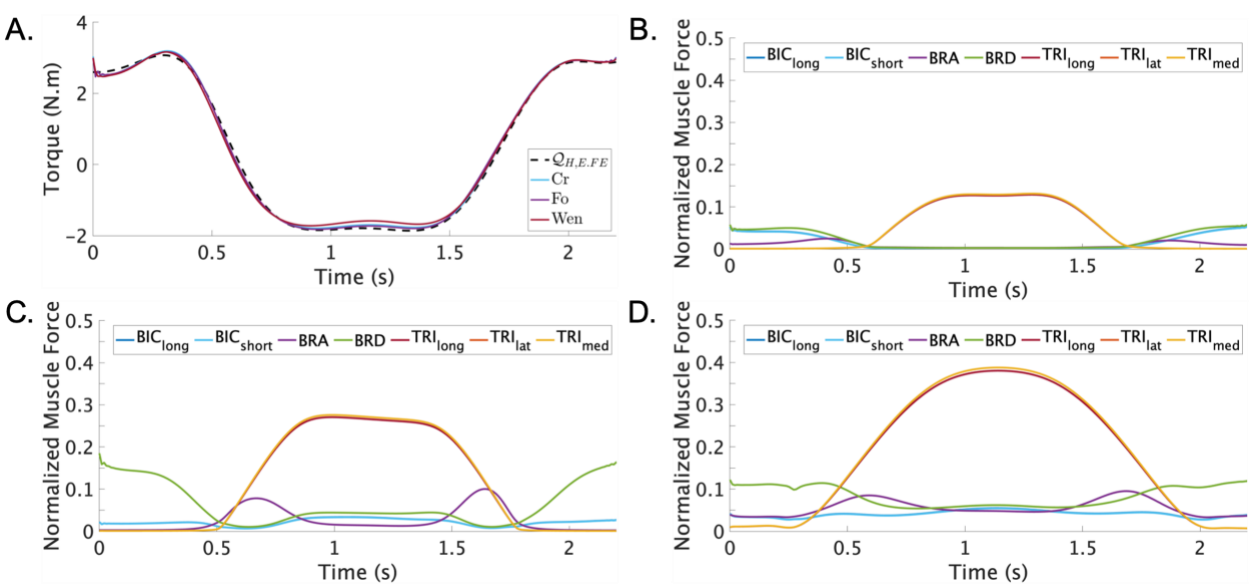

Figure 4.12 **A.** Computed E.FE torque with Crowninshield (light blue), Forster (purple), and Wen (red) cost function during ES functional task. Elbow torque from inverse dynamics is plotted as reference (dashed line). Individual muscle forces estimated with **B.** Crowninshield, **C.** Forster, and **D.** Wen cost function.

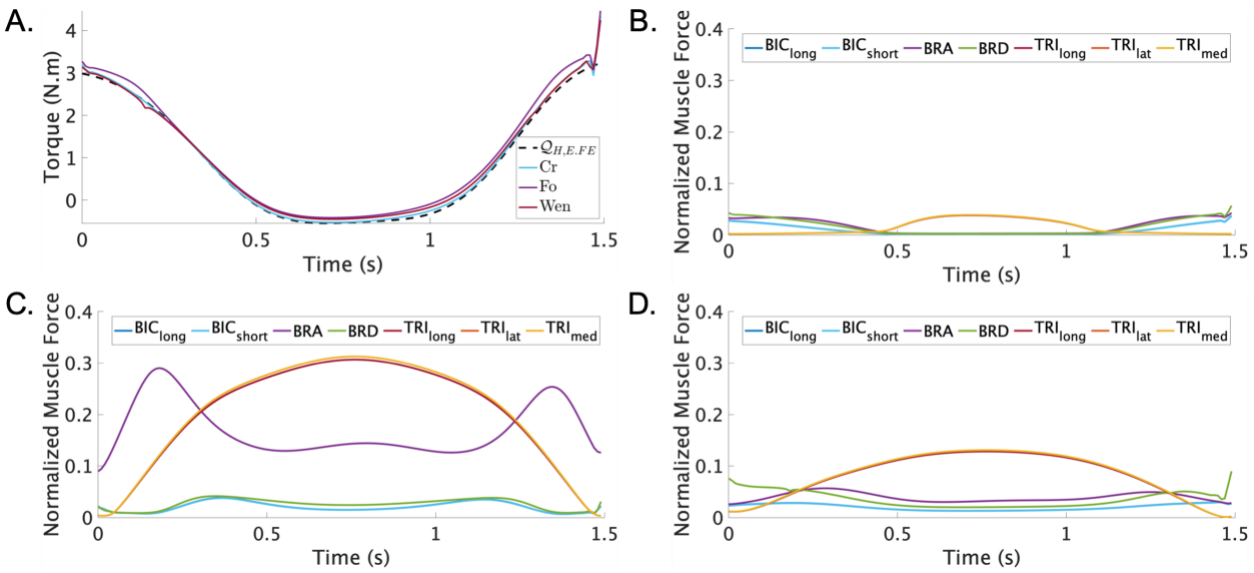

Figure 4.13 **A.** Computed E.FE torque with Crowninshield (light blue), Forster (purple), and Wen (red) cost function during ZC functional task. Elbow torque from inverse dynamics is plotted as reference (dashed line). Individual muscle forces estimated with **B.** Crowninshield, **C.** Forster, and **D.** Wen cost function.

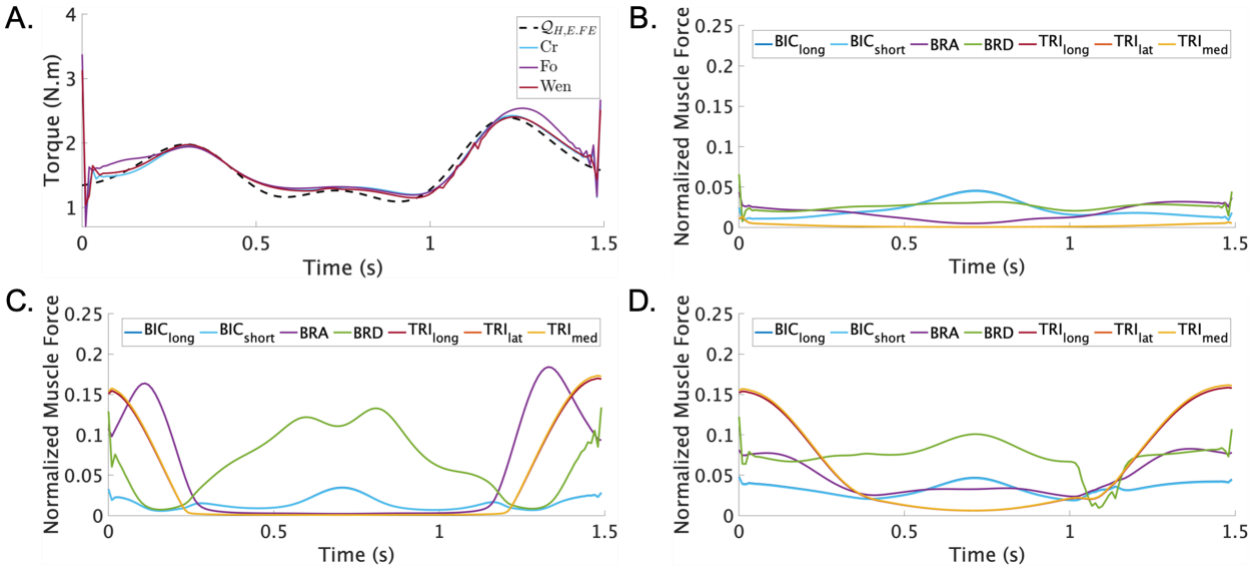

Figure 4.14 **A.** Computed E.FE torque with Crowninshield (light blue), Forster (purple), and Wen (red) cost function during AR functional task. Elbow torque from inverse dynamics is plotted as reference (dashed line). Individual muscle forces estimated with **B.** Crowninshield, **C.** Forster, and **D.** Wen cost function.

4.3 Discussion

The **SO2** was to implement a non-EMG-based method to quantify muscle forces during upper limb movements. The proposed approach to tackle the muscle redundancy problem is based on solving an OCP where a muscle cost function is integrated to the objective function of the OCP. To optimize the performance of the OCP, a methodological approach using RSM is proposed to identify the optimal weights for the objective function instead of using the commonly used heuristic approach. The RSM performance was confirmed by a GA while being more time efficient and easy to use. The calibration of the optimal weights is performed during E.FE. The identified weights are then used to quantify muscle forces during three functional tasks, namely ES, ZC, and AR.

4.3.1 Optimal weights for p_T, p_Q, and p_{Mu}

Two different approaches were used to identify the optimal weights for p_T and p_Q, namely RSM and GA. Both approaches showed similar performance in term of the OCP results but identified different optimal weights. The identification of multiple combinations of p_T and p_Q that results in the same performance suggests that the OCP does not have a global minimum. However, there was an important difference regarding the time required to identify the optimal weights. Indeed, the whole RSM was realized in a day of work (about 7-8 hours), while the GA took close to 9 full days. It is worth mentioning that the GA parameters were not optimized, which could have reduced the time required to find the optimal weights. Nonetheless, the difference between the two methods was important enough to choose RSM for the calibration p_{Mu}.

The RSM approach presents some limitations. First, only a small portion of the global design space was analyzed. Indeed, the upper bound of the final design space for p_T and p_Q was respectively 10^4 and 10^{-4} while the values identified in the literature were respectively 10^9 and 10^0. However, it is reasonable to assume that the identified weights are near-optimal since the GA, which explored the design space unbounded, did not identify weights that resulted in a better performance. Secondly, the second-order models of the response variables were not optimized following the ANOVA. Indeed, the ANOVA showed that the quadratic term of p_Q was not statistically significant for both response variables ($RMSE_{traj}$ and $iter$). A new second-order model could have been investigated by ignoring the quadratic term of p_Q. The predicted profiles and desirability functions

might have identified different optimal weights in the design space. Nonetheless, the probability that these new optimal weights resulted in better performance remains small.

RSM was also used to identify the optimal weight for p_{Mu}. While the process was also modeled with a FCD, a Box-Behnken design (BBD) could have been used. BBD are commonly used to fit second-order models for three or more independent variables. In this thesis, FCD was preferred for two reasons. First, it allowed for better consistency since all RSM used the same design. Second, the design points in FCD allow to evaluate the OCP at each corner of the design space, which is not possible with BBD. Nonetheless, it would be interesting to compare if FCD and BBD identified similar optimal weights.

The above-mentioned observation on the optimization of the second-order models of the response variables during RSM for p_T and p_Q also applies to p_{Mu}. Indeed, the ANOVA identified multiple terms that were not statistically significant for each response variable and muscle cost function. Removing the non-significant terms in the second-order models could lead to better results in terms of R^2, ${R^2}_{adj}$, and RSD as well as new optimal weights.

4.3.2 Muscle force quantification

The proposed musculoskeletal model allows us to tackle the muscle redundancy problem through an OCP. The muscle forces are quantified with a non-EMG-based method using one of the three following cost functions: Cr, Fo, and Wen. As seen in Figure 4.12, Figure 4.13, and Figure 4.14, each cost function resulted in a different muscle force distribution. The Fo and Wen cost functions allow for co-contraction of the muscles while the Cr cost function does not. Nonetheless, all cost functions can estimate muscle forces that result in a computed E.FE torque which is similar to $Q_{H,E.FE}$ from inverse dynamics.

Despite that the objective function was calibrated on E.FE, the OCP was able to quantify muscle forces for functional tasks. This shows that the optimal weights of the objective function are not movement dependent. However, the identified weights might benefit from a fine tuning to improve the OCP performance. Indeed, the observed $rRMSE_Q$ for multiple cost functions and functional tasks were higher than 10 %, while they were all below 5 % for E.FE. The highest values were observed for AR, which might be explained by a greater difference in $Q_{H,E.FE}$ compared to E.FE. In contrast, the $Q_{H,E.FE}$ curves for ES and ZC were similar to E.FE and resulted in lower $rRMSE_Q$.

The observed difference between muscle forces depending on the cost function used are interesting. First, almost no co-contraction is observable with the Cr cost function for all functional tasks. This is expected and was already reported in [108]. The estimation of muscle forces with Fo and Wen cost function resulted in higher $rRMS_{F_M}$ than Cr since co-contraction is introduced. However, it is interesting to note that the introduction of co-contraction does not result in higher $rRMS_{F_M}$ for all muscles. Indeed, BIC_{long} and BIC_{short} showed a decrease in $rRMS_{F_M}$ for Fo cost function during ES and AR. This decrease can be explained by a larger increase in $rRMS_{F_M}$ for BRD and BRA. Therefore, the proposed musculoskeletal model seems to favor co-contraction of BRD and BRA over BIC_{long} and BIC_{short}.

The observation of the maximum normalized muscle force during the analyzed tasks highlights a possible limitation of the model. Indeed, Figure 4.12D shows normalized muscle forces that reach close to 0.4 for TRI_{long}, TRI_{lat}, and TRI_{med} during ES. This is concerning since ES is not a highly dynamic movement both in terms of speed and load. The normalization of muscle forces was made with the F_{max} values from Table 3.1. These values were taken from reference tables in the literature [99] and are not personalized to the subject. Since the subject analyzed was in great physical condition, it is possible that the reference values for F_{max} underestimate its real F_{max}. This could explain the high observed normalized muscle forces.

CHAPTER 5 VALIDATION OF AN EXOSKELETON PERFORMANCE

This chapter presents the validation of an exoskeleton performance by investigating the impact on muscle forces quantification through simulation. The 3D and MBS models of the exoskeleton were developed by the research team [123], [195] and their latest iterations are extensively presented in [196]. The work presented demonstrates the achievement of **SO3**: Validate the performance of an exoskeleton during functional tasks through simulation.

5.1 Preliminary work

This section briefly summarizes the improvements to the proposed exoskeleton customization procedure developed by Blanchet et al. [13]. These improvements are extensively described in the work of Li [196]. Therefore, they will only be briefly presented in this thesis. The main improvements to the customization procedure are as follows:

General improvements:

- Integration of the exoskeleton's mechanical design in the synthesis procedure.
- Addition of a quasi-static structural analysis on the mechanical design of the exoskeleton.
- Synthesis tool used on two typically developed subjects of different morphology.

Geometric customization:

- Reduction of computation time for geometric optimization by simplifying the initial values definition for multi-task exoskeletons.
- Integration of torso in collision avoidance.

Dynamic sizing:

- Quantification of the effects of adding dynamic components on exoskeleton to the upper limb torques.
- Dynamic sizing based on a multitask.

The author's contribution to the work of Li [196] is estimated at 15 %. Specifically, the author contributed to:

- Modelling of the torso and integration of constraints for collision avoidance

- Reduction of the computation time for geometric and dynamic customization
- Study conception and design for the dynamic components
- Interpretation of results for the dynamic sizing of the exoskeleton

5.1.1 Integration of the exoskeleton

The exoskeleton model, presented in Figure 5.1, is an active assistive upper limb exoskeleton. The exoskeleton was designed to reduce the user's joint torques during ES, ZC, and AR. While this objective was achieved, it does not pretend to be a perfect design [196]. The exoskeleton connects to a wearable back brace as well as two braces, one at the upper arm and one at the forearm. The arm braces are described by the kinematics constraints of body cuts $h_{l,1-6}$ and $h_{l,7-12}$. As a reminder, body cuts impose that the brace and arm possess a common point of attachment and that their body orientation coincide at any time [132].

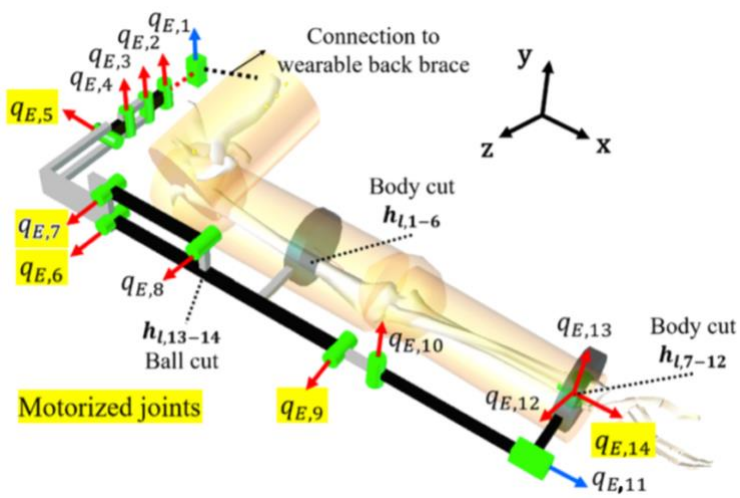

Figure 5.1 The exoskeleton model [196] with fourteen (14) generalized coordinates q_E. Joints $q_{E,5-7,9,14}$ are motorized (highlighted in yellow). The kinematics constraints imposed by the body cuts represent the braces that connect the exoskeleton to the user's arm. The ball cut closes the four-bar mechanism. Prismatic and rotational joints are respectively represented by blue and red arrows. The gas tension spring is not represented in the image. (Image adapted from [14]).

The exoskeleton is composed of five joints that are motorized and nine additional passive joints. Moreover, torsion springs were added to joint $q_{E,5}$ and $q_{E,9}$ as well as a tension gas spring to take

advantage of the four-bar mechanism. The tension gas spring allows to lower the output requirements of the motorized joints $q_{E,5}$ and $q_{E,6}$.

In details, the prismatic joint $q_{E,1}$ accounts for the elevation-depression of the shoulder. It is followed by three redundant rotational joints $q_{E,2-4}$ that allows the exoskeleton to adjust itself to the shoulder movements. The rotation joint $q_{E,5}$ is motorized and assist S.AA. The four-bar mechanism supports the S.FE and is composed of three rotational joints $q_{E,6-8}$ and ball cut $h_{l,13-14}$. Joints $q_{E,6-7}$ of the four-bar mechanism are motorized. The E.FE is supported by the motorized joint $q_{E,9}$. The next four passive joints $q_{E,10-13}$ ensure the kinematic compatibility of the exoskeleton with closed-loop model of the forearm. Finally, the motorized joint $q_{E,14}$ supports F.PS.

5.1.2 Geometric customization

The objective of the geometric customization is to personalize the exoskeleton dimensions $\boldsymbol{l}_E$ to the user's anatomy. A total of 17 dimensions were selected for the geometric customization procedure and are illustrated in Figure 5.2. The initial dimensions of the exoskeleton, $\boldsymbol{l}_{E,ini}$, were obtained with user-defined proportional ratios based on the anthropometric measurements of the individual to generalize the procedure to users of different size. The geometric customization was realized for three functional tasks: ES, ZC, and AR.

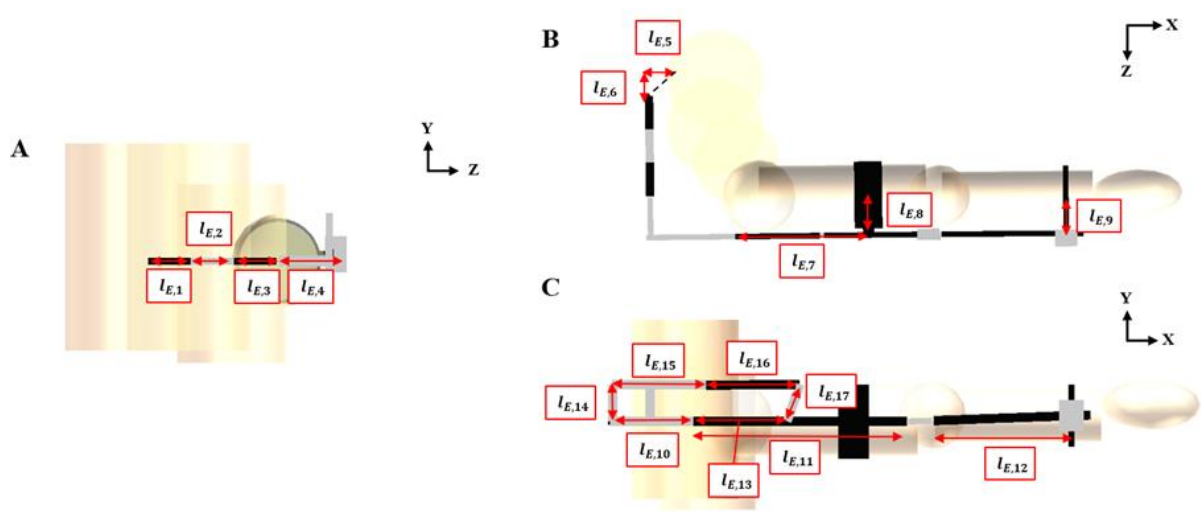

Figure 5.2 Optimized dimensions $\boldsymbol{l}_E$ of the exoskeleton [196]. **A.** Dimensions $l_{E,1-4}$ (posterior view) **B.** Dimensions $l_{E,5-9}$ (top view) **C.** Dimensions $l_{E,10-17}$ (sagittal view).

The exoskeleton adjustment is defined as a combination of three elements [14]: (1) loop closure, (2) proximity between the exoskeleton and the upper-limb and (3) collisions avoidance. The first two elements are integrated in the objective function of the optimization problem (Eq. 5.1) , while the latter is defined as geometrical constraints. The global objective function is defined as:

$$\min_{\boldsymbol{l_E},\boldsymbol{q_v}} \sum_{\boldsymbol{q_{u,i=1}}}^{\boldsymbol{q_{u,n_{task}}}} p_{loop} L_C + p_{dist} D \tag{5.1}$$

where the exoskeleton dimensions $\boldsymbol{l_E}$ and the dependent generalized coordinates $\boldsymbol{q_v}$ are the optimisation variables. The independent relative coordinates $\boldsymbol{q_u}$ describe the displacement of the user's arm for the ith functional task. The loop closure L_C and the distance D between the exoskeleton and the upper limb are respectively weighted by p_{loop} and p_{dist}. Weights were fixed at 10^4 and 1 for respectively p_{loop} and p_{dist} to emphasize the importance of loop closure. Loop closure L_c and distance D are respectively defined as:

$$L_c = \frac{1}{2} \boldsymbol{h_l}(\boldsymbol{q},\boldsymbol{l})^T \boldsymbol{h_l}(\boldsymbol{q},\boldsymbol{l}) \tag{5.2}$$

$$D = \alpha \sum_{i=1}^{n} d_i(\boldsymbol{q},\boldsymbol{l}) \tag{5.3}$$

where $\boldsymbol{h_l}$ are the loop closure geometrical constraints. The distances $\boldsymbol{d}$ [m] are illustrated in Figure 5.3. Coefficient α is set to 1 for all distances, except for d_{6-7} where it is set to 5 to emphasize the proximity of the exoskeleton at the shoulder level [196].

Collision avoidance was considered in the geometrical constraints, modelling the volume of the torso and the upper limb as cylinders or spheres and each piece of the exoskeleton as a cylinder as well. Constraints where also added to limit joints amplitude, to guarantee the parallelism of the four-bar mechanism, the elongation of the tension gas spring and to impose continuity between specific exoskeleton joints.

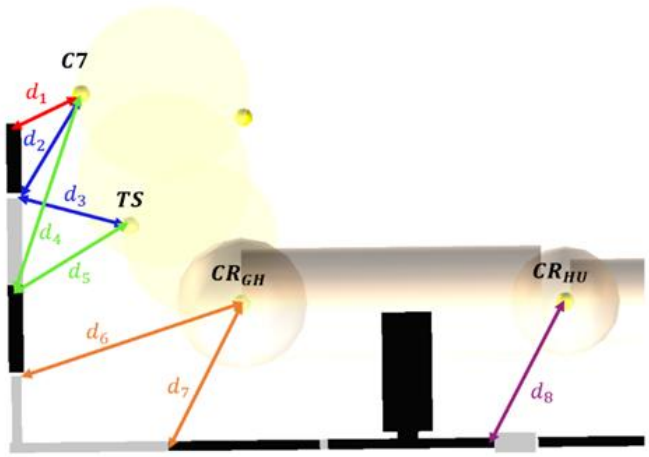

Figure 5.3 Optimized distances d_{1-8} of the human-exoskeleton model (top view) [196]. Two anatomic landmarks on the torso (C7, TS) as well as the center of rotation of the shoulder (CR_{GH}) and the elbow (CR_{HU}) are shown.

5.1.3 Dynamic sizing

The aim of the dynamic sizing was to size the dynamic components of an active assistive exoskeleton to assist the upper limb across chosen ADLs. The dynamic sizing [196] was done through an experimental design which is presented in Table 5.1. This sizing includes an active sizing and a sizing by selection. The active sizing aims to study the effect of the exoskeleton's dynamic components on the upper limb's torque while the sizing by selection aims to select the most appropriate dynamic components based on the active sizing and the dynamic components available from the manufacturer. A dynamic sizing is considered a success if it satisfies the three following conditions:

- The dynamic sizing of the exoskeleton must lower the RMS torque at the upper limb joints
- The RMS torque of each motor must stay lower than the nominal torque of the selected model
- The dynamic behavior of the motors must respect the torque-speed limits.

Considering an initial state where the upper limb is not supported at all, the OCP is defined by a formulation based on direct dynamics. The state variables $\boldsymbol{x}(t)$ and the control vector $\boldsymbol{u}(t)$ are described as:

$$\boldsymbol{x}(t) = [\dot{\boldsymbol{q}}_u \; \boldsymbol{q}_u] \tag{5.4}$$

$$\boldsymbol{u}(t) = [\boldsymbol{Q}_H \; \boldsymbol{Q}_A \; F_{TGS} \; \boldsymbol{k} \; \boldsymbol{q}_0] \tag{5.5}$$

where the state variables $\dot{\boldsymbol{q}}_u$ and $\boldsymbol{q}_u$ are respectively the independent velocity and position, and the control variables $\boldsymbol{Q}_H$, $\boldsymbol{Q}_A$, F_{TGS}, $\boldsymbol{k}$, and $\boldsymbol{q_0}$ are respectively the human joint torques, the motor (actuator) torques, the compression force of the tension gas spring, the torsion springs constant and the initial position of the torsion springs. The objective function is defined as:

$$\min_{\boldsymbol{Q_H},\boldsymbol{Q_M},\mathrm{F_{TGS}},\boldsymbol{k},\boldsymbol{q_0},\dot{\boldsymbol{q}}_{\boldsymbol{u}},\boldsymbol{q_u}} \underbrace{p_T T}_{Trajectory} + \underbrace{p_Q Q}_{Joint\ torques} \tag{5.6}$$

where T and Q correspond respectively to the previously defined Eq. 4.4 and Eq. 4.5. Extensive details on the respective expressions, the weights and the constraints of the equations can be found in the work of Li – Section 4.6 [196].

Table 5.1 Experimental design for the dynamic sizing of the exoskeleton (Adapted from [196]).

Trial number	S.AA		S.FE		E.FE		F.PS
	Motor	**Spring**	**Motor**	**Spring**	**Motor**	**Spring**	**Motor**
Control	N	N	N	N	N	N	N
A1	N	N	N	N	N	N	XC430-W150-R3
A2	N	N	N	N	XH540-W270	N	XM430-W350-R3
A3	N	N	N	N	XH540-W270	T	XM430-W350-R3
A4	N	N	XH540-W270 (2)	N	XH540-W270	T	XM430-W350-R3
A5	N	N	XH540-W270 (2)	TGS	XH540-W270	T	XM430-W350-R3
A6	XH540-W270	N	XH540-W270 (2)	TGS	XH540-W270	T	XM430-W350-R3
A7	XH540-W270	T	XH540-W270 (2)	TGS	XH540-W270	T	XM430-W350-R3
S1	XH540-W270	T-Selection	XH540-W270 (2)	TGS-Selection	XH540-W270	T - Selection	XM430-W350-R3
S2	Motor - Selection	T – S1	Motors (2) - Selection	TGS – S1	Motor - Selection	T – S1	Motor - Selection

Abbreviations: N: None; T: Torsion spring; TGS: Tension gas spring

5.1.4 Results & discussion

This section briefly summarizes the main results and discussion from Li [196]. The 3D model of the customized exoskeleton is presented in Figure 5.4.

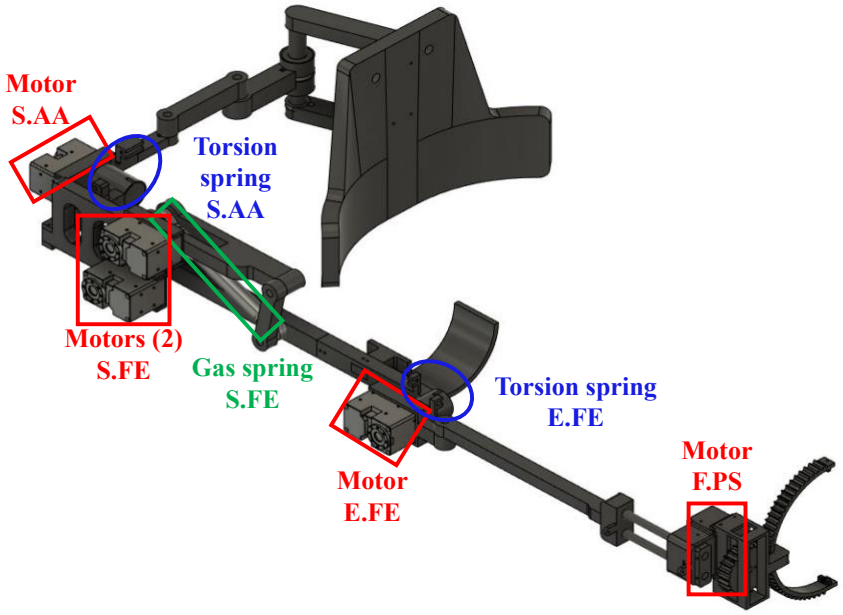

Figure 5.4 Illustration of the 3D model of the optimized exoskeleton [196]. The shoulder, elbow, and forearm movements are actuated by a motor. Passive elements are also integrated in the exoskeleton which enables to reduce the size of the required motors.

5.1.4.1 Geometric customization

The geometric customization resulted in similar distances between the exoskeleton and the human as observed in [14]. However, the error on the loop closure was 10.7 times lower than the error reported by Blanchet et al. [14], which indicates and overall better adjustment of the exoskeleton. The maximal loop closure error was observed at the humerus brace and was 5.70 mm. This error is physically acceptable, considering that skin itself can produce displacements as high as 12 mm [197].

5.1.4.2 Dynamic sizing

The dynamic sizing concluded that the addition of passive elements such as springs does not always reduce the motor's torque. Indeed, the addition of a torsion spring to S.AA resulted in an increased RMS torque of the S.AA motor compared to when no spring was used. However, this result should be considered as preliminary since the dynamic sizing revealed kinematic limitations. Indeed, an important conclusion of the dynamic sizing is that the misalignment of the exoskeleton was revealed. Misalignment was observed for the shoulder joint. Indeed, the addition of motors to compensate S.FE also resulted in decreased torques for S.AA.

At the end of the sizing per selection, all upper limb joint torques were lowered by a minimum of 97,8 %, while respecting all conditions of success. The dynamic sizing proposed by Li [196] was able to identify motors that were each 100 $ less expensive than the motors identified by Blanchet et al. [14], while being able to compensate the upper limb for the three most problematic ADL (ES, ZC and AR) of patients affected by neuromuscular pathologies.

5.1.4.3 Limitations

The work from Li [196] included the following limitations. First, the exoskeleton showed misalignment at the shoulder and elbow joints. New mechanisms should be investigated to improve the exoskeleton kinematics. Secondly, the geometric and dynamic optimizations were realized separately. Since the exoskeleton geometry influences the dynamic sizing, a procedure to optimize both parameters simultaneously should be considered. Finally, the dynamic sizing requires the designer to make a-priori selection of the motors at the beginning of the dynamic sizing. An automatic selection of the motors could be implemented to make the whole dynamic sizing procedure objective.

5.2 Methodology

The custom-fitted exoskeleton was added to the developed AMM. The final MBS model is presented in Figure D.1 of Appendix D - Musculoskeletal-exoskeleton multibody model in ROBOTRAN.

The previously defined OCP with the identified optimal weights was used to validate the exoskeleton support during the three functional tasks with respect to the muscle forces (Eq. 4.3).

The *user torque ratio C*, defined by Blanchet et al. [14], is used to characterize the support of the exoskeleton. This ratio is defined as:

$$C = \frac{RMS(\boldsymbol{Q}_{M,exo})}{RMS(\boldsymbol{Q}_{M,ref})} \cdot 100 \text{ [\%]} \tag{5.7}$$

where $\boldsymbol{Q}_{M,exo}$ and $\boldsymbol{Q}_{M,ref}$ are the computed elbow torque from muscle forces respectively with and without the exoskeleton support. To facilitate the comparison with the results of Li [196] and Blanchet et al. [14], a *user torque ratio* of 0 % is expected. This means that RMS($\boldsymbol{Q}_{M,exo}$) should be close to 0 N.m since the exoskeleton was designed to fully compensate the user's produced torque.

5.3 Results

The integration of the exoskeleton to the musculoskeletal model has caused an increase of the human joint torques computed from inverse dynamics during the three functional tasks. This increase is expected since the exoskeleton adds an additional weight to the user's upper limb. The variation of the $\mathcal{Q}_{H,E.FE}$ is presented in Table 5.2. The increase in terms of RMS was only 0.5 N.m, 0.4 N.m, and 0.4 N.m, which respectively represent a variation of 22.9 %, 23.4 %, and 25.4 % for respectively ES, ZC, and AR. These results show that wearing an exoskeleton have an impact on the human movement, as noted by Bastide et al. [198]. Therefore, it is important to monitor the possible impacts and limit their effect on the user, both in a static position and during dynamic movements.

Table 5.2 Impact of the integration of the exoskeleton on the human elbow torque $\mathcal{Q}_{H,E.FE}$ during the functional tasks.

Task	$\boldsymbol{RMS(\mathcal{Q}_{H,E.FE})}$		
	w/o exo (N.m)	**w/ exo (N.m)**	**Variation (%)**
ES	2.1	2.6	22.9
ZC	1.6	2.0	23.4
AR	1.7	2.1	25.4

The *user torque ratio C* for each functional task and cost function are presented in Table 5.3. The computed elbow torque from the muscles and the motors during ES, ZC, and AR are illustrated

respectively in Figure 5.5A, Figure 5.6A, and Figure 5.7A. In general, the *user torque ratio C* were similar for a same task no matter the cost function, except for ES. Indeed, Wen cost function resulted in a *user torque ratio C* of 29.7 %, while it was of 7.0 % and 6.6 % for Cr and Fo respectively. The *user torque ratio C* was around 15.1 % and 18.1 % for ZC and AR respectively. While these values imply a decrease in the computed torque from muscles of at least 80 %, it is far from the observed 97.8 % decrease in Li [196].

Table 5.3 *User torque ratio C* for each functional movement (ES, ZC, AR) and muscle cost function (Cr, Fo, Wen).

Task	Cost function	$\boldsymbol{C}$ (%)
ES	Cr	7.0
	Fo	6.6
	Wen	29.7
ZC	Cr	14.1
	Fo	15.7
	Wen	15.4
AR	Cr	18.5
	Fo	17.9
	Wen	18.0

The individual muscle forces are also presented in Figure 5.5, Figure 5.6, and Figure 5.7 respectively for ES, ZC, and AR. Sub-figures B, C, and D respectively present the quantified forces with Cr, Fo, and Wen cost function. The results of muscle force quantification show that, while the computed torque from muscles is close to 0 N.m, the individual muscle forces are high. Moreover, when comparing the curves of Figure 5.5, Figure 5.6, and Figure 5.7, with the ones of Figure 4.12, Figure 4.13, and Figure 4.14 (from AMM), the individual forces with the exoskeleton support are even higher than when no exoskeleton is used. This result shows that the exoskeleton is only able to reduce the computed torque for E.FE and not the individual muscle forces.

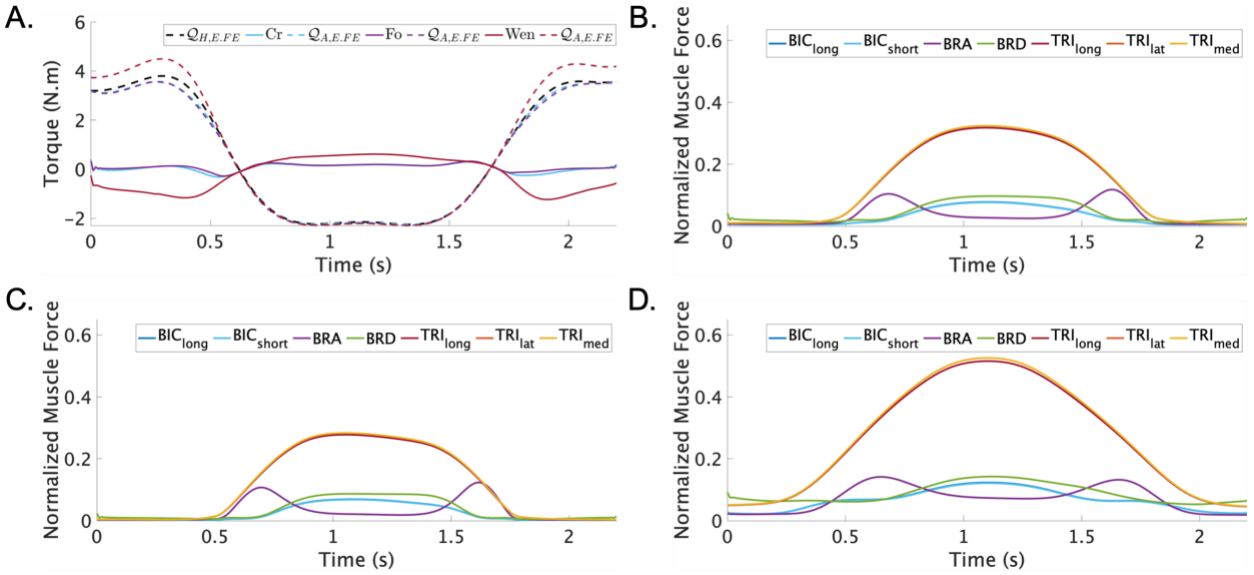

Figure 5.5 **A.** Computed E.FE torque with Crowninshield (Cr, blue), Forster (Fo, purple), and Wen (red) cost function during ES functional task. Actuator torque for each cost function is plotted as a dashed line in its respective color. Elbow torque from inverse dynamics is plotted as reference (dashed black line). Individual muscle forces estimated with **B.** Cr, **C.** Fo, and **D.** Wen.

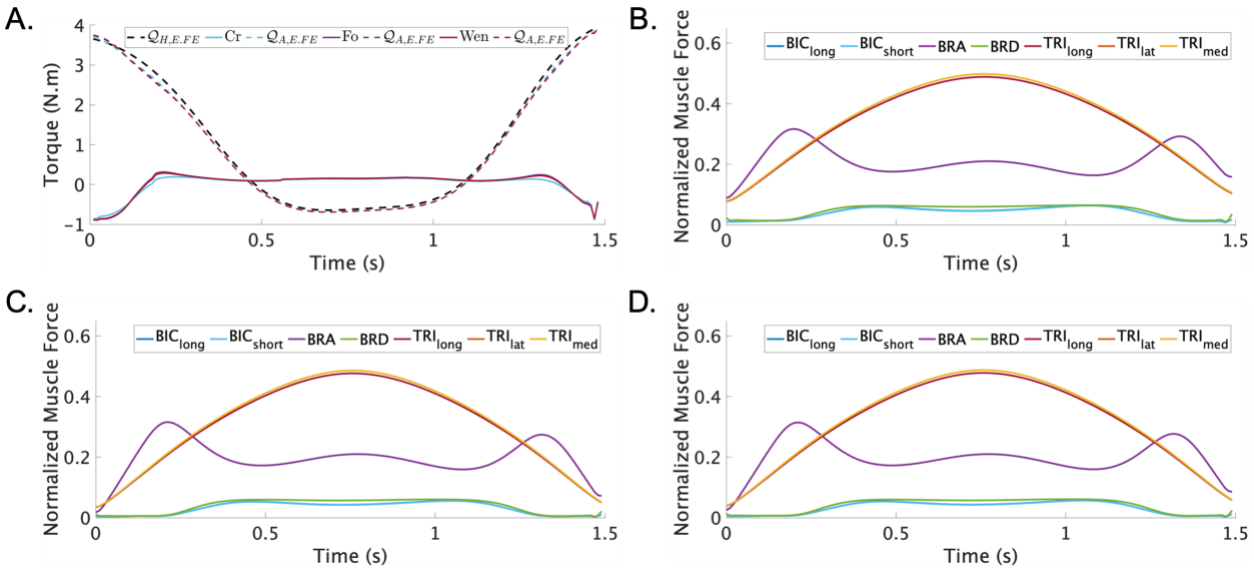

Figure 5.6 **A.** Computed E.FE torque with Crowninshield (Cr, blue), Forster (Fo, purple), and Wen (red) cost function during ZC functional task. Actuator torque for each cost function is plotted as a dashed line in its respective color. Elbow torque from inverse dynamics is plotted as reference (dashed black line). Individual muscle forces estimated with **B.** Cr, **C.** Fo, and **D.** Wen.

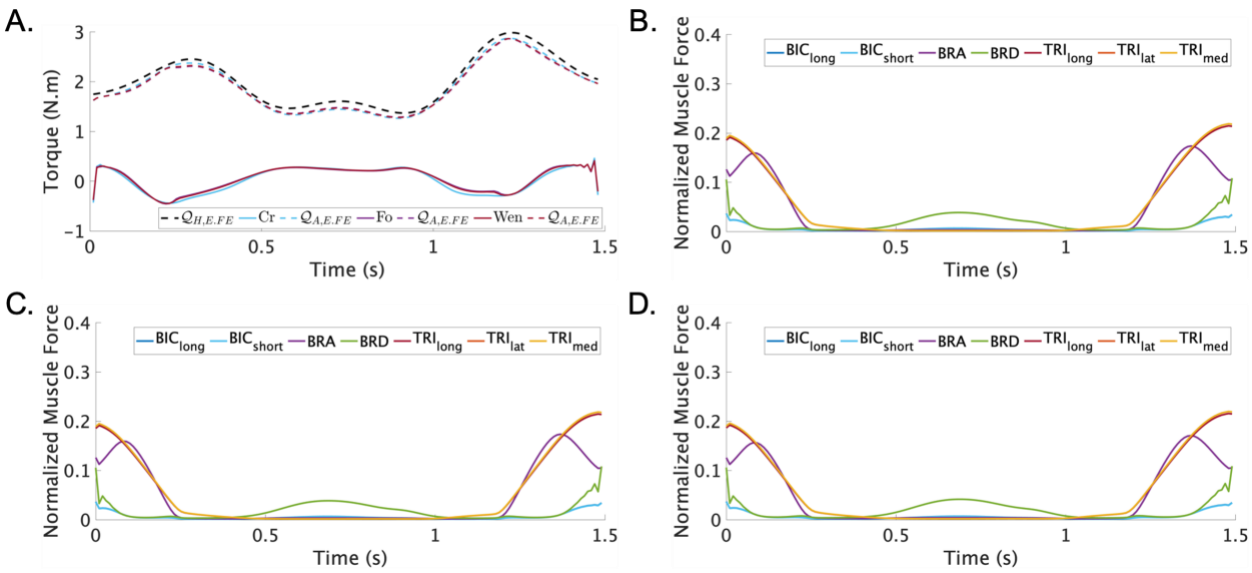

Figure 5.7 **A.** Computed E.FE torque with Crowninshield (Cr, blue), Forster (Fo, purple), and Wen (red) cost function during AR functional task. Actuator torque for each cost function is plotted as a dashed line in its respective color. Elbow torque from inverse dynamics is plotted as reference (dashed black line). Individual muscle forces estimated with **B.** Cr, **C.** Fo, and **D.** Wen.

5.4 Discussion

The **SO3** was to validate the performance of an exoskeleton during functional tasks through simulation. The validation is realized by computing the *user torque ratio C* that evaluates how well the exoskeleton can compensate for the user's torque. The exoskeleton used for validation was able to lower the user's E.FE torque produced by the muscles by at least 80 %. However, this decrease is not noticeable in terms of muscle forces. Indeed, the individual muscle forces showed an increase during ES and ZC.

The first observed impact of the exoskeleton was on the user's joint torques. The increase in E.FE joint torque was similar in terms of RMS torque for all tasks (Table 5.2). The absolute variation of the user's E.FE torque was similar for all tasks since the exoskeleton adds the same weight no matter the task. However, the relative variation varied slightly between tasks since each one solicits the E.FE differently. A comparison of the proposed exoskeleton's weight with commercially available exoskeletons raises concerns on the usability of the device. The designed exoskeleton weighs 7.0 kg (3.5 kg per side [196]). This number does not include the power source and other electronic components required by the motors. However, these elements could be attached to the

waist area to limit the impact on the user's joint torques at the upper limb [199]. Nonetheless, the exoskeleton's weight remains, on average, twice as high as the commercially available exoskeletons: ShoulderX (3.2 kg) [65], Ekso-EVO (4.3 kg) [68], Airframe (3.2 kg) [62], and Skelex 360-XFR (2.5 kg) [66]. The weight difference can be partially explained by the presence of motors on the proposed exoskeleton, which represents 22 % of its total weight. In contrast, all the above-mentioned commercial exoskeletons are passive, which makes it easier to design lightweight devices. Nonetheless, this confirms that additional work is needed to reduce the proposed exoskeleton's weight. Moreover, it will be important to record the functional tasks while wearing the proposed exoskeleton to evaluate the impact of it on joint kinematics as well as joint torques.

The use of E.FE torque produced by the muscles to compute the *user torque ratio C*, resulted in overall higher values than when using joint torque, as it was done by [14], [196]. This is an important finding as it shows the limitation of using joint torques as the only target to size an exoskeleton. Indeed, the exoskeleton, in its current form, is not able to reduce the individual muscle forces during the functional tasks. A certain amount of residual muscle forces is expected when using Fo and Wen since these cost functions allow muscle co-contraction. However, the Cr cost function does not consider co-contraction. Therefore, the muscle forces should be close to 0 N if the exoskeleton fully compensates for the user's effort, as it was designed for.

A possible explanation for these high muscle forces lies in the exoskeleton kinematic compatibility with the user's upper limb. The exoskeleton designed by Li [196], and used in this thesis, showed misalignment between the axis of rotation of the motors and those of the human joints. A precise alignment of motor and human joints axis is primordial in exoskeleton design since misalignment produces spurious forces or torques at the human-exoskeleton interface, which can result in discomfort and injuries [148]. It is highly possible that the observed muscle forces are compensating the spurious forces and torques produced by the E.FE motor.

CHAPTER 6 GENERAL DISCUSSION

The general objective of this thesis was to **develop a design tool to validate, through simulation, the performance of an exoskeleton based on the quantification of muscle forces**. This objective was achieved through the completion of the three following specific objectives (SO):

SO1 (Chapter 3): Model the muscles on top of an existing osteoarticular multibody system of the upper limb.

SO2 (Chapter 4**)**: Implement a non-EMG-based method to quantify muscle forces during upper limb movements.

SO3 (Chapter 5): Validate the performance of an exoskeleton during functional tasks through simulation.

This chapter presents a general discussion on the achievements of the objectives of this thesis and concludes by the limits of the projects and the future work.

6.1 Musculoskeletal model of the upper limb

The proposed musculoskeletal model is the first of its kind for the upper limb developed with ROBOTRAN. It includes the main elbow flexors and extensors: *BIC*, *BRA*, *BRD*, *TRI*. Moreover, it is based on the most precise osteoarticular model in the literature for elbow modeling [27], which ensures the accuracy of the model for biomechanics simulation. Simulation software are scarce in biomechanics. Therefore, it is challenging to validate a software in multiple ways [200] since the options are limited.

The validation of the musculoskeletal model was based on a comparison with OpenSim [201], an open-source and well established biomechanics software in the scientific community. Another option would have been to use the software Anybody [202]. However, Anybody is a closed and proprietary software. Therefore, it is impossible to directly compare both software if they produce different results. This happened in two recent papers [203], [204] that compared the outputs of Anybody and OpenSim. The authors were able to provide possible explanations for these differences. However, these explanations cannot be verified due to the closed-source nature of Anybody. The proposed musculoskeletal model in this thesis was developed with ROBOTRAN, which is free-to-use for teaching and academic research. Moreover, the MBS equations generated

by ROBOTRAN are available as a clear box, which means that they are accessible for inspection. Therefore, the proposed musculoskeletal could eventually provide a new tool for the validation of biomechanics software.

6.2 Quantification of muscle forces

The musculoskeletal model solves the muscle redundancy problem at the elbow through an OCP approach. The model focuses on non-EMG-based method to quantify the muscle forces, since they are easier to implement and do not require expensive equipment for data acquisition. The muscle forces can be quantified with one of the three following cost function: Crowninshield, Forster, Wen.

The three chosen cost functions were selected for the following reasons. First, Cr cost function, based on the muscle force-endurance relationship, is the most widely used and accepted in the literature [18]. It is notably available in OpenSim [106] and Anybody [202]. However, Cr cost function is limited because it underestimates antagonist muscle activity. To overcome this limitation, Fo cost function introduced a co-contraction factor. The results from Forster et al. [108] showed an increase in antagonist muscle force, to maintain or improve joint stability. Nonetheless, the co-contraction factor is defined as a constant and no guidelines are given on how to adjust the factor. Finally, the recently published Wen cost function tackles the definition of the co-contraction factor by calibrating it with EMG data [18]. The calibration process uncovered a general relationship between the elbow joint torque $\mathcal{Q}_{H,E.FE}$ and the co-contraction factor. Therefore, the cost function from Wen allows for a quantification of muscle forces that is physiologically coherent with EMG data, while keeping the same advantages of non-EMG-based cost function.

The objective function of the OCP to solve the muscle redundancy problem was formulated as a weighted sum. One of the challenges of using a weighted sum method is to identify optimal weights to obtain satisfying results. Although some literature indicates that the sum of the individual weights should equal zero, it is not always necessary. As stated by Marler and Arora [177], the critical idea when selecting weights is that "*the value of a weight is significant not only relative to other weights but also relative to its corresponding objective function*". Since the individual terms of the global objective have different magnitudes, no constraints were imposed on the weight values.

Two different approaches were implemented to identify the optimal weights, namely RSM and GA. The idea behind the implementation of these methods is to bring rigor for the selection of optimal weights instead of relying on a trial-and-error approach. While the two approaches resulted in similar performance in terms of accuracy, RSM allowed to find the optimal weights faster. The application of RSM to identify the optimal weights of an OCP's objective function is a novel advancement in biomechanics simulation and will improve the performance of the developed models.

Regarding the quantification of muscle forces, the proposed model allows to easily switch between the three cost functions implemented. The use of an OCP to solve the muscle redundancy problem at the elbow was successful for different movements. The estimated individual muscle forces are realistic and vary with respect to the cost function used. In general, Cr cost function results in the lowest muscle forces since there is no co-contraction. Between Fo and Wen cost function, the muscles forces are generally higher for Fo since the co-contraction factor is a constant that is situated on the higher end of the range identified by Wen co-contraction formulae.

6.3 Validation of the exoskeleton performance

The validation of the exoskeleton performance was realized by (1) computing the *user torque ratio* between the muscle torque with and without the exoskeleton support and (2) observing the quantified muscle forces. The exoskeleton that is integrated into this thesis was designed to fully compensate for the user's efforts and was sized with respect to the user's joint torque [196]. Hence, the expected *user torque ratio* is 0 %. The validation presented in this thesis shows that the exoskeleton is not able to fully compensate the user's effort when the *user torque ratio* is computed with the user's muscle torque.

The validation also showed that the exoskeleton was not able to decrease the individual muscle forces. This observation highlights that using the user's joint torque for the dynamic sizing might not be sufficient to guarantee the exoskeleton performance. Indeed, the procedure does not consider the spurious torques at the elbow due to the exoskeleton's misalignment, which are most likely compensated by the muscle forces.

6.4 Research contributions

This research project resulted in different research contributions. They are summarized in and associated with their respective **SO**.

Table 6.1 Research contributions and their associated specific objective (SO).

Research contribution	SO
New method: Musculoskeletal multibody model of the elbow: • Four main elbow actuators: BIC, BRA, BRD, TRI • Musculotendinous length and moment arms are coherent with the literature	**SO1**
New method: Use of RSM to optimize weights of a weighted-sum objective function in an OCP	-
New knowledge: RSM provides similar performance to GA for optimal weight selection while requiring less time	-
New method: Quantification of muscle forces with a non-EMG-based method • Muscle redundancy is solved with an OCP • Muscle forces can be quantified with three different cost functions: Cr, Fo, and Wen	**SO2**
New knowledge: Utilizing user's joint torques for dynamic sizing is not sufficient to guarantee the exoskeleton's performance	**SO3**
New observation: Spurious torques from exoskeleton misalignment are compensated by muscle forces	-

6.5 Limits of the project and future work

Even though the general objective of this thesis was achieved, there exist limitations that need to be addressed before the musculoskeletal model can be used in a commercial or medical context. These limitations open the way to new research studies to improve and validate the model thoroughly. The following paragraphs present the limits with their respective future work.

First, this research project was realized only on one subject. This limitation is important as it raises doubts on the generalization of the musculoskeletal models to other subjects. Since the proposed musculoskeletal mode is personalized to the user's anthropometry, it is reasonable to assume that it would be accurate for subject of different sizes. Nonetheless, it would be important to test the accuracy of the proposed model for different populations with different characteristics.

Secondly, the developed musculoskeletal model only included muscles for E.FE. This limits its use to the analysis of a single upper limb movement, which is restricting considering the multiple DoF that the upper limb possess. Future work should focus on modeling additional muscles to allow the quantification of muscle forces responsible for shoulder movement and F.PS.

Thirdly, an important limitation of this thesis is that the quantified muscle forces were not validated. While the obtained muscle forces were realistic, the proposed model is not able to confirm without a doubt that the muscle forces are precise. To obtain such validation, a first step would be to implement the non-EMG-based method from this thesis in OpenSim and compare the quantified muscle forces with both software. Another approach is to quantify the muscle forces with an EMG-based method and use these results as a golden standard.

Finally, this research project did not acquire data with the exoskeleton. The exoskeleton is still in the design phase and was not available for actual testing. Future work will need to record kinematics data with the exoskeleton since it will probably have an impact on the user's movement. The impact of the exoskeleton on the user's trajectory and speed was not considered in the design and validation process.

CHAPTER 7 CONCLUSION

The goal of this research project was to develop a musculoskeletal multibody model of the elbow for non-EMG-based muscle forces quantification, to validate, through simulation, the performance of an assistive exoskeleton. The proposed model includes the four principal E.FE muscles, namely BIC, BRA, BRD, and TRI, and is used for three functional tasks.

The first step was to model E.FE muscles to an existing multibody model of the upper limb. The muscles were modeled with a via-points method, which facilitates the design and usability of the model. The modeled muscles showed good consistency in terms of musculotendinous length and muscle moment arms with reference values from the literature.

The second step involved the quantification of muscle forces. This is an ongoing challenge in the literature and requires solving the muscle redundancy problem. The redundancy problem can be tackled with different methods. In this thesis, an OCP approach was chosen for this optimization problem. The objective function of the OCP required the adjustment of weights for a weighted-sum optimization. This thesis proposes to use RSM for optimal identification of weights instead of proceeding with a trial-and-error method. Following the adjustment of the weights, muscle forces were quantified with three different muscle cost functions, namely Cr, Fo, and Wen. More importantly, the joint torque produced by the muscle forces was coherent with the joint torque obtained from inverse dynamics.

The last step focused on the validation of a previously developed exoskeleton. This exoskeleton was designed to fully compensate the user's joint torque from inverse dynamics. The validation step examined if the exoskeleton was also able to compensate the joint torque produced by muscle forces. While the joint torque produced by the muscles showed a significant decrease when using the exoskeleton, the compensation by the exoskeleton did not reach its expected level. Even more concerning is that the muscle forces did not decrease with the exoskeleton support. This additional validation raises doubts on the exoskeleton design. Indeed, the misalignment between the exoskeleton joint and the human elbow is a possible reason behind these high muscle forces.

The proposed musculoskeletal multibody model from this thesis requires additional work to be used more broadly. This involves the integration of more muscles to the model so it can be used to analyze a wider range of upper limb movements.

To conclude, the developed model consists of a first step in the development of new a biomechanics software for upper limb simulations. The musculoskeletal model can be used alone for the quantification of muscle forces during upper limb movements, which is desirable in many applications. Indeed, rehabilitation, ergonomics, and sport industry could improve their services by gaining the precious information provided by muscle forces. The musculoskeletal model can also be used in combination with rehabilitation devices, such as exoskeletons, to provide a tool for validation. This could lead to improved design, which will result in a better quality of life for the users. Moreover, the validation step through simulation will help identify weaknesses in the beginning of the design process, which will decrease the development costs and limit the production of badly designed prototypes.

REFERENCES

[1] R. J. Adams, A. Ellington, M. White, and P. T. Diamond, "Assessing Upper Extremity Motor Function in Practice of Virtual Activities of Daily Living," *IEEE Trans. NEURAL Syst. Rehabil. Eng.*, vol. 23, no. 2, Art. no. 2, 2015.

[2] W. T. Latt, T. P. Luu, C. Kuah, and A. W. Tech, "Towards an Upper-limb Exoskeleton System for Assistance in Activities of Daily Living (ADLs)," in *Proceedings of the international Convention on Rehabilitation Engineering & Assistive Technology*, Midview City, SGP, Aug. 2014, pp. 1–4.

[3] C.-J. Lai, W.-Y. Liu, T.-F. Yang, C.-L. Chen, C.-Y. Wu, and R.-C. Chan, "Pediatric aquatic therapy on motor function and enjoyment in children diagnosed with cerebral palsy of various motor severities," *J. Child Neurol.*, vol. 30, no. 2, pp. 200–208, Feb. 2015, doi: 10.1177/0883073814535491.

[4] P. A. Wright, S. Durham, D. J. Ewins, and I. D. Swain, "Neuromuscular electrical stimulation for children with cerebral palsy: a review," *Arch. Dis. Child.*, vol. 97, no. 4, pp. 364–371, Apr. 2012, doi: 10.1136/archdischild-2011-300437.

[5] B. Balaban, D. J. Matthews, G. H. Clayton, and T. Carry, "Corticosteroid treatment and functional improvement in Duchenne muscular dystrophy: long-term effect," *Am. J. Phys. Med. Rehabil.*, vol. 84, no. 11, pp. 843–850, Nov. 2005, doi: 10.1097/01.phm.0000184156.98671.d0.

[6] L. Ouyang, S. D. Grosse, and A. Kenneson, "Health care utilization and expenditures for children and young adults with muscular dystrophy in a privately insured population," *J. Child Neurol.*, vol. 23, no. 8, pp. 883–888, Aug. 2008, doi: 10.1177/0883073808314962.

[7] E. Guglielmelli *et al.*, "Self-feeding apparatus," WO2006126239A2, Nov. 30, 2006 Accessed: Mar. 24, 2022. [Online]. Available: https://patents.google.com/patent/WO2006126239A2/un

[8] V. Maheu, J. Frappier, P. S. Archambault, and F. Routhier, "Evaluation of the JACO robotic arm: clinico-economic study for powered wheelchair users with upper-extremity disabilities," *IEEE Int. Conf. Rehabil. Robot. Proc.*, vol. 2011, p. 5975397, 2011, doi: 10.1109/ICORR.2011.5975397.

[9] A. Gupta, A. Singh, V. Verma, A. K. Mondal, and M. K. Gupta, "Developments and clinical evaluations of robotic exoskeleton technology for human upper-limb rehabilitation," *Adv. Robot.*, vol. 34, no. 15, pp. 1023–1040, août 2020, doi: 10.1080/01691864.2020.1749926.

[10] M. A. Gull, S. Bai, and T. Bak, "A Review on Design of Upper Limb Exoskeletons," *Robotics*, vol. 9, no. 1, Art. no. 1, Mar. 2020, doi: 10.3390/robotics9010016.

[11] R. A. R. C. Gopura, D. S. V. Bandara, K. Kiguchi, and G. K. I. Mann, "Developments in hardware systems of active upper-limb exoskeleton robots: A review," *Robot. Auton. Syst.*, vol. 75, pp. 203–220, 2016.

[12] T. M. Shank, J. Wee, J. Ty, and T. Rahman, "Quantitative measures with WREX usage," in *International Conference on Rehabilitation Robotics (ICORR)*, Jul. 2017, pp. 1375–1380. doi: 10.1109/ICORR.2017.8009440.

[13] J. Higginson and L. Ma, “Playskin Lift: Development and Initial Testing of an Exoskeletal Garment to Assist Upper Extremity Mobility and Function,” p. 10, 2016.

[14] L. Blanchet, S. Achiche, Q. Docquier, P. Fisette, and M. Raison, “A procedure to optimize the geometric and dynamic designs of assistive upper limb exoskeletons,” *Multibody Syst. Dyn.*, vol. 51, no. 2, pp. 221–245, Feb. 2021, doi: 10.1007/s11044-020-09766-6.

[15] Y. Hayashi, R. Dubey, and K. Kiguchi, “Torque optimization for a 7DOF upper-limb power-assist exoskeleton robot,” in *2011 IEEE Workshop on Robotic Intelligence In Informationally Structured Space*, Apr. 2011, pp. 49–54. doi: 10.1109/RIISS.2011.5945786.

[16] Y. Aoustin and A. M. Formalskii, “Walking of biped with passive exoskeleton: evaluation of energy consumption,” *Multibody Syst. Dyn.*, vol. 43, no. 1, pp. 71–96, May 2018, doi: 10.1007/s11044-017-9602-7.

[17] L. Zhou, Y. Li, and S. Bai, “A human-centered design optimization approach for robotic exoskeletons through biomechanical simulation,” *Robot. Auton. Syst.*, vol. 91, pp. 337–347, May 2017, doi: 10.1016/j.robot.2016.12.012.

[18] J. Wen, M. Raison, and S. Achiche, “Using a cost function based on kinematics and electromyographic data to quantify muscle forces,” *J. Biomech.*, vol. 80, pp. 151–158, Oct. 2018, doi: 10.1016/j.jbiomech.2018.09.002.

[19] M. Raison, C. Detrembleur, and P. Fisette, “Assessment of Antagonistic Muscle Forces During Forearm Flexion/Extension,” in *Comput Methods Appl Sci*, vol. 23, 2010, pp. 215–238. doi: 10.1007/978-90-481-9971-6_11.

[20] T. S. Buchanan, D. G. Lloyd, K. Manal, and T. F. Besier, “Neuromusculoskeletal Modeling: Estimation of Muscle Forces and Joint Moments and Movements From Measurements of Neural Command,” p. 34, 2006.

[21] J. M. Winters and L. Stark, “Muscle models: What is gained and what is lost by varying model complexity,” *Biol. Cybern.*, vol. 55, no. 6, pp. 403–420, Mar. 1987, doi: 10.1007/BF00318375.

[22] D. Knudson, *Fundamentals of Biomechanics*. Springer International Publishing, 2021.

[23] H. Patel, “Medical Terminology - Body Position.” Accessed: Jun. 24, 2022. [Online]. Available: https://www.slideshare.net/HemalPatel26/medical-terminology-body-position

[24] D. H. Gates, L. S. Walters, J. Cowley, J. M. Wilken, and L. Resnik, “Range of Motion Requirements for Upper-Limb Activities of Daily Living,” *Am. J. Occup. Ther.*, vol. 70, no. 1, pp. 7001350010p1-7001350010p10, Dec. 2015, doi: 10.5014/ajot.2016.015487.

[25] E. N. Marieb and K. Hoehn, *Human Anatomy & Physiology*. Pearson Education, Incorporated, 2018.

[26] G. J. Tortora and B. H. Derrickson, *Tortora’s Principles of Anatomy and Physiology*. Wiley, 2017.

[27] M. Laitenberger, M. Raison, D. Périé, and M. Begon, “Refinement of the upper limb joint kinematics and dynamics using a subject-specific closed-loop forearm model,” *Multibody Syst. Dyn.*, vol. 33, no. 4, pp. 413–438, Apr. 2015, doi: 10.1007/s11044-014-9421-z.

[28] Rice University, “Anatomy and Physiology,” *openstax - Access. The future of education*, 2022. https://openstax.org/details/books/anatomy-and-physiology

[29] “One simple move to loosen up your shoulders,” *Sequence Wiz*, Mar. 16, 2016. https://sequencewiz.org/2016/03/16/loosen-up-your-shoulders/ (accessed Jun. 27, 2022).

[30] J. Ruddock, “Serving yourself up a problem, is your tennis serve causing you pain?,” *Align Body Clinic*, 2018. https://alignbodyclinic.co.uk/serving-yourself-up-a-problem-is-your-tennis-serve-causing-you-pain/ (accessed Jun. 24, 2022).

[31] A. Kapandji, *Anatomie Fonctionnelle T.1 - Membre Supérieur 7e Éd.*, 7th edition. Paris: Maloine, 2018.

[32] F. H. Netter, *Atlas of Human Anatomy*. Elsevier, 2018.

[33] I. M. Andres, “Contribution of the Anconeus Muscle to the Elbow Kinematics: Range of Motion of 90° of Flexion-Extension and Pronation-Supination,” The University of Manchester, 2016. Accessed: Feb. 25, 2022. [Online]. Available: https://www.research.manchester.ac.uk/portal/files/55558628/FULL_TEXT.PDF

[34] H. Gray, *Anatomy of the Human Body*, Lea&Febiger, 1918. Bartleby.com, 2000. [Online]. Available: www.bartleby.com/107/

[35] H. J. Sommer III and N. R. Miller, “A Technique for Kinematic Modeling of Anatomical Joints,” *J. Biomech. Eng.*, vol. 102, no. 4, pp. 311–317, Nov. 1980, doi: 10.1115/1.3138228.

[36] R. Riener, T. Nef, and G. Colombo, “Robot-aided neurorehabilitation of the upper extremities,” *Med. Biol. Eng. Comput.*, vol. 43, no. 1, pp. 2–10, Jan. 2005, doi: 10.1007/BF02345116.

[37] A. Emery, “The muscular dystrophies,” *The Lancet*, vol. 359, no. 9307, pp. 687–695, Feb. 2002, doi: https://doi.org/10.1016/S0140-6736(02)07815-7.

[38] M. R. Lunn and C. H. Wang, “Spinal muscular atrophy,” *The Lancet*, vol. 371, no. 9630, pp. 2120–2133, Jun. 2008, doi: 10.1016/S0140-6736(08)60921-6.

[39] D. Makki, J. Duodu, and M. Nixon, “Prevalence and pattern of upper limb involvement in cerebral palsy,” *J. Child. Orthop.*, vol. 8, no. 3, pp. 215–219, May 2014, doi: 10.1007/s11832-014-0593-0.

[40] R. Hamdy and N. Dahan-Oliel, “Arthrogryposis,” in *Pediatric Lower Limb Deformities: Principles and Techniques of Management*, S. Sabharwal, Ed. Cham: Springer International Publishing, 2016, pp. 297–311. doi: 10.1007/978-3-319-17097-8_18.

[41] P. O’Berry, M. Brown, L. Phillips, and S. H. Evans, “Obstetrical Brachial Plexus Palsy,” *Curr. Probl. Pediatr. Adolesc. Health Care*, vol. 47, no. 7, pp. 151–155, Jul. 2017, doi: 10.1016/j.cppeds.2017.06.003.

[42] N. Valè *et al.*, “Characterization of Upper Limb Impairments at Body Function, Activity, and Participation in Persons With Multiple Sclerosis by Behavioral and EMG Assessment: A Cross-Sectional Study,” *Front. Neurol.*, vol. 10, 2020, Accessed: Mar. 01, 2022. [Online]. Available: https://www.frontiersin.org/article/10.3389/fneur.2019.01395

[43] J. Mackay, G. A. Mensah, W. H. Organization, and K. Greenlund, *The Atlas of Heart Disease and Stroke*. World Health Organization, 2004.

[44] J. Zariffa *et al.*, “Relationship Between Clinical Assessments of Function and Measurements From an Upper-Limb Robotic Rehabilitation Device in Cervical Spinal Cord Injury,” *IEEE Trans. NEURAL Syst. Rehabil. Eng.*, vol. 20, no. 3, Art. no. 3, 2012.

[45] M. M. H. P. Janssen, J. Horstik, P. Klap, and I. J. M. de Groot, “Feasibility and effectiveness of a novel dynamic arm support in persons with spinal muscular atrophy and duchenne muscular dystrophy,” *J. Neuroengineering Rehabil.*, vol. 18, no. 1, p. 84, May 2021, doi: 10.1186/s12984-021-00868-6.

[46] J. G. Hall, E. Kimber, and K. Dieterich, “Classification of arthrogryposis,” *Am. J. Med. Genet.*, vol. 181, no. 3, pp. 300–303, 2019.

[47] H. Feys *et al.*, “Early and repetitive stimulation of the arm can substantially improve the long-term outcome after stroke: a 5-year follow-up study of a randomized trial,” *Stroke*, vol. 35, no. 4, pp. 924–929, Apr. 2004, doi: 10.1161/01.STR.0000121645.44752.f7.

[48] G. Gaudet, M. Raison, and S. Achiche, “Current Trends and Challenges in Pediatric Access to Sensorless and Sensor-Based Upper Limb Exoskeletons,” *Sensors*, vol. 21, no. 10, Art. no. 10, Jan. 2021, doi: 10.3390/s21103561.

[49] M. M. H. P. Janssen, J. Harlaar, B. Koopman, and I. J. M. de Groot, “Dynamic arm study: quantitative description of upper extremity function and activity of boys and men with duchenne muscular dystrophy,” *J. NeuroEngineering Rehabil.*, vol. 14, no. 1, p. 45, May 2017, doi: 10.1186/s12984-017-0259-5.

[50] A. Cruz, L. Callaway, M. Randall, and M. Ryan, “Mobile arm supports in Duchenne muscular dystrophy: a pilot study of user experience and outcomes,” *Disabil. Rehabil. Assist. Technol.*, vol. 16, no. 8, pp. 880–889, Nov. 2021, doi: 10.1080/17483107.2020.1749892.

[51] L. A. van der Heide, G. J. Gelderblom, and L. P. de Witte, “Dynamic arm supports: Overview and categorization of dynamic arm supports for people with decreased arm function,” in *IEEE 13th International Conference on Rehabilitation Robotics (ICORR)*, Seattle, WA, Jun. 2013, pp. 1–6. doi: 10.1109/ICORR.2013.6650491.

[52] J. L. Pons, *Wearable Robots: Biomechatronic Exoskeletons*. John Wiley & Sons, 2008.

[53] B. R. Fick and J. B. Makinson, “Hardiman I Prototype for Machine Augmentation of Human Strength and Endurance,” GENERAL ELECTRIC CO SCHENECTADY NY SPECIALTY MATERIALS HANDLING PRODUCTS OPERATION, Aug. 1971. Accessed: Apr. 01, 2022. [Online]. Available: https://apps.dtic.mil/sti/citations/AD0739735

[54] “hardiman | GE News,” *Do You Even Lift, Bro ? Hardiman Was GE’s Muscular Take On The Human-Machine Interface*. https://www.ge.com/news/taxonomy/term/2999 (accessed Apr. 11, 2022).

[55] H. Kazerooni, “Human-robot interaction via the transfer of power and information signals,” *IEEE Trans. Syst. Man Cybern.*, vol. 20, no. 2, pp. 450–463, Mar. 1990, doi: 10.1109/21.52555.

[56] Y. Sankai, “HAL: Hybrid Assistive Limb Based on Cybernics,” *Robot. Res.*, pp. 25–34, 2010, doi: 10.1007/978-3-642-14743-2_3.

[57] A. Zoss, H. Kazerooni, and A. Chu, “On the mechanical design of the Berkeley Lower Extremity Exoskeleton (BLEEX),” in *2005 IEEE/RSJ International Conference on Intelligent*

Robots and Systems, Edmonton, Alta., Canada, 2005, pp. 3465–3472. doi: 10.1109/IROS.2005.1545453.

[58] U. Keller and R. Riener, "Design of the pediatric arm rehabilitation robot ChARMin," in *5th IEEE RAS/EMBS International Conference on Biomedical Robotics and Biomechatronics*, Aug. 2014, pp. 530–535. doi: 10.1109/BIOROB.2014.6913832.

[59] M. Gunn, T. M. Shank, M. Eppes, J. Hossain, and T. Rahman, "User Evaluation of a Dynamic Arm Orthosis for People With Neuromuscular Disorders," *IEEE Trans. Neural Syst. Rehabil. Eng.*, vol. 24, no. 12, pp. 1277–1283, Dec. 2016, doi: 10.1109/TNSRE.2015.2492860.

[60] H. M. Qassim and W. Z. Wan Hasan, "A Review on Upper Limb Rehabilitation Robots," *Appl. Sci.*, vol. 10, no. 19, Art. no. 19, Jan. 2020, doi: 10.3390/app10196976.

[61] N. Rehmat, J. Zuo, W. Meng, Q. Liu, S. Q. Xie, and H. Liang, "Upper limb rehabilitation using robotic exoskeleton systems: a systematic review," *Int. J. Intell. Robot. Appl.*, vol. 2, no. 3, pp. 283–295, Sep. 2018, doi: 10.1007/s41315-018-0064-8.

[62] Levitate Technologies, "Engineering a Healthier Workplace.," *AIRFRAME - Fatigue has a New Enemy*. https://www.levitatetech.com/airframe/ (accessed Mar. 07, 2022).

[63] Comau, "Mate XT – Fit for workers," *Where does it work? Where you do.* https://mate.comau.com/ (accessed Mar. 07, 2022).

[64] Ottobock Bionic Exoskeletons, "Paexo Shoulder," *The supportive exoskeleton for overhead work*. https://paexo.com/paexo-shoulder/?lang=en (accessed Mar. 07, 2022).

[65] suitX, "ShoulderX," *Dynamic Shoulder Support*. https://www.suitx.com/shoulderx (accessed Mar. 07, 2022).

[66] Skelex, "Skelex 360-XFR," *The Ultimate Exoskeleton for Overhead Work*. https://www.skelex.com/ (accessed Mar. 07, 2022).

[67] Hyundai Motor Group, "Hyundai and Kia's Wearable Robot: VEX(Vest EXoskeleton)." https://tech.hyundaimotorgroup.com/article/hyundai-and-kias-wearable-robot-vexvest-exoskeleton/ (accessed Mar. 07, 2022).

[68] Ekso Bionics, "EVO - The Next Exoskeleton Vest," *Ekso Evo*. https://eksobionics.com/ekso-evo/ (accessed Mar. 07, 2022).

[69] T. Haumont *et al.*, "Wilmington robotic exoskeleton: a novel device to maintain arm improvement in muscular disease," *J. Pediatr. Orthop.*, vol. 31, no. 5, pp. e44-49, Aug. 2011, doi: 10.1097/BPO.0b013e31821f50b5.

[70] I. Babik, E. Kokkoni, A. B. Cunha, J. C. Galloway, T. Rahman, and M. A. Lobo, "Feasibility and Effectiveness of a Novel Exoskeleton for an Infant with Arm Movement Impairments," *Pediatr. Phys. Ther. Off. Publ. Sect. Pediatr. Am. Phys. Ther. Assoc.*, vol. 28, no. 3, pp. 338–346, 2016, doi: 10.1097/PEP.0000000000000271.

[71] B. Li *et al.*, "Design of the Playskin Air™: A User-Controlled, Soft Pneumatic Exoskeleton," presented at the 2019 Design of Medical Devices Conference, Jul. 2019. doi: 10.1115/DMD2019-3231.

[72] Myomo, "MyoPal: Increased function for children with a paralyzed or weakened arm.," Nov. 25, 2020. https://myomo.com/myopal/

[73] J. Huang, X. Tu, and J. He, “Design and Evaluation of the RUPERT Wearable Upper Extremity Exoskeleton Robot for Clinical and In-Home Therapies,” *IEEE Trans. Syst. Man Cybern. Syst.*, vol. 46, no. 7, pp. 926–935, Jul. 2016, doi: 10.1109/TSMC.2015.2497205.

[74] Bioservo Technologies, “Improve your hand function,” *Bioservo - Strength for Life*.

[75] G.-Y. Gu, “A survey on dielectric elastomer actuators for soft robots,” *Bioinspir Biomim*, p. 23, 2017.

[76] E. Biddiss and T. Chau, “Dielectric elastomers as actuators for upper limb prosthetics: Challenges and opportunities,” *Med. Eng. Phys.*, vol. 30, no. 4, pp. 403–418, May 2008, doi: 10.1016/j.medengphy.2007.05.011.

[77] J.-H. Youn *et al.*, “Dielectric Elastomer Actuator for Soft Robotics Applications and Challenges,” *Appl. Sci.*, vol. 10, no. 2, Art. no. 2, Jan. 2020, doi: 10.3390/app10020640.

[78] K. Huysamen, T. Bosch, M. de Looze, K. S. Stadler, E. Graf, and L. W. O’Sullivan, “Evaluation of a passive exoskeleton for static upper limb activities,” *Appl. Ergon.*, vol. 70, pp. 148–155, juillet 2018, doi: 10.1016/j.apergo.2018.02.009.

[79] P. Polygerinos, Z. Wang, K. C. Galloway, R. J. Wood, and C. J. Walsh, “Soft robotic glove for combined assistance and at-home rehabilitation,” *Robot. Auton. Syst.*, vol. 73, pp. 135–143, Nov. 2015, doi: 10.1016/j.robot.2014.08.014.

[80] S. Crea *et al.*, “Feasibility and safety of shared EEG/EOG and vision-guided autonomous whole-arm exoskeleton control to perform activities of daily living,” *Sci. Rep.*, vol. 8, no. 1, Art. no. 1, Jul. 2018, doi: 10.1038/s41598-018-29091-5.

[81] Z. Tang, H. Yu, H. Yang, L. Zhang, and L. Zhang, “Effect of velocity and acceleration in joint angle estimation for an EMG-Based upper-limb exoskeleton control,” *Comput. Biol. Med.*, vol. 141, p. 105156, Feb. 2022, doi: 10.1016/j.compbiomed.2021.105156.

[82] B. Samadi, S. Achiche, A. Parent, L. Ballaz, U. Chouinard, and M. Raison, “Custom sizing of lower limb exoskeleton actuators using gait dynamic modelling of children with cerebral palsy,” *Comput. Methods Biomech. Biomed. Engin.*, vol. 19, no. 14, pp. 1519–1524, Oct. 2016, doi: 10.1080/10255842.2016.1159678.

[83] S. V. Sarkisian, M. K. Ishmael, and T. Lenzi, “Self-Aligning Mechanism Improves Comfort and Performance With a Powered Knee Exoskeleton,” *IEEE Trans. Neural Syst. Rehabil. Eng.*, vol. 29, pp. 629–640, 2021, doi: 10.1109/TNSRE.2021.3064463.

[84] B. Falk, C. Usselman, R. Dotan, L. Brunton, P. Klentrou, and D. Gabriel, “Child–adult differences in muscle strength and activation pattern during isometric elbow flexion and extension,” p. 14, 2013.

[85] C. L. Owings, D. B. Chaffin, R. G. Snyder, and R. H. Norcutt, “Strength characteristics of U.S. children for product safety design. Final report,” The University of Michigan, 1975. Accessed: May 12, 2021. [Online]. Available: /paper/Strength-characteristics-of-U.S.-children-for-Final-Owings/749d33719262b47a7e97ead199bf638b195eeeda

[86] M. N. Eek, A.-K. Kroksmark, and E. Beckung, “Isometric muscle torque in children 5 to 15 years of age: normative data,” *Arch. Phys. Med. Rehabil.*, vol. 87, no. 8, pp. 1091–1099, Aug. 2006, doi: 10.1016/j.apmr.2006.05.012.

[87] A. Nasr, S. Ferguson, and J. McPhee, “Model-Based Design and Optimization of Passive Shoulder Exoskeletons,” *J. Comput. Nonlinear Dyn.*, vol. 17, no. 5, Mar. 2022, doi: 10.1115/1.4053405.

[88] D. Tsirakos, V. Baltzopoulos, and R. Bartlett, “Inverse Optimization: Functional and Physiological Considerations Related to the Force-Sharing Problem,” *Crit. Rev. Biomed. Eng.*, vol. 25, no. 4–5, 1997, doi: 10.1615/CritRevBiomedEng.v25.i4-5.20.

[89] L. Z. F. Chiu, “Biomechanical Methods to Quantify Muscle Effort During Resistance Exercise,” *J. Strength Cond. Res.*, vol. 32, no. 2, pp. 502–513, Feb. 2018, doi: 10.1519/JSC.0000000000002330.

[90] V. Zatsiorsky, *Biomechanics in Sport: Performance Enhancement and Injury Prevention*. John Wiley & Sons, 2008.

[91] M. Epstein and W. Herzog, *Theoretical Models of Skeletal Muscle: Biological and Mathematical Considerations*. Wiley, 1998.

[92] G. Gaudet, M. Raison, S. Achiche, F. D. Maso, G. Musy, and M. Begon, “Solutions to the Muscle Redundancy Problem: From an Underterminate to a Deterministic Problem,” in *11th World Congress on Computational Mechanics (WCCM XI)*, Barcelona, Spain, 2014, p. 2.

[93] J. M. Winters, “An improved muscle-reflex actuator for use in large-scale neuromusculoskeletal models,” *Ann. Biomed. Eng.*, vol. 23, no. 4, pp. 359–374, Jul. 1995, doi: 10.1007/BF02584437.

[94] F. Dal Maso, M. Begon, and M. Raison, “Methodology to Customize Maximal Isometric Forces for Hill-Type Muscle Models,” *J. Appl. Biomech.*, vol. 33, no. 1, pp. 80–86, Feb. 2017, doi: 10.1123/jab.2016-0062.

[95] F. E. Zajac, “Muscle and tendon: properties, models, scaling, and application to biomechanics and motor control,” *Crit. Rev. Biomed. Eng.*, vol. 17, no. 4, pp. 359–411, Jan. 1989.

[96] J. M. Winters, “Hill-Based Muscle Models: A Systems Engineering Perspective,” in *Multiple Muscle Systems: Biomechanics and Movement Organization*, J. M. Winters and S. L.-Y. Woo, Eds. New York, NY: Springer, 1990, pp. 69–93. doi: 10.1007/978-1-4613-9030-5_5.

[97] D. G. Thelen, “Adjustment of Muscle Mechanics Model Parameters to Simulate Dynamic Contractions in Older Adults,” *J. Biomech. Eng.*, vol. 125, no. 1, pp. 70–77, Feb. 2003, doi: 10.1115/1.1531112.

[98] A. F. Huxley, “6 - Muscle Structure and Theories of Contraction,” *Prog. Biophys. Biophys. Chem.*, vol. 7, pp. 255–318, Jan. 1957, doi: 10.1016/S0096-4174(18)30128-8.

[99] K. R. S. Holzbaur, W. M. Murray, and S. L. Delp, “A Model of the Upper Extremity for Simulating Musculoskeletal Surgery and Analyzing Neuromuscular Control,” *Ann. Biomed. Eng.*, vol. 33, no. 6, Art. no. 6, Jun. 2005, doi: 10.1007/s10439-005-3320-7.

[100] G. Durandau and W. Suleiman, “Toward a Unified Framework for EMG Signals Processing and Controlling an Exoskeleton,” presented at the Proceedings - Conference on Computer and Robot Vision, CRV 2014, May 2014, pp. 291–298. doi: 10.1109/CRV.2014.46.

[101] F. Heinen *et al.*, “Muscle-Tendon Unit Parameter Estimation of a Hill-Type Musculoskeletal Model Based on Experimentally Obtained Subject-Specific Torque Profiles,” *J. Biomech. Eng.*, vol. 141, no. 6, p. 061005, Jun. 2019, doi: 10.1115/1.4043356.

[102] L. Sun, Y. Sun, Z. Huang, J. Hou, and J. Wu, “Improved Hill-type musculotendon models with activation-force-length coupling,” *Technol. Health Care*, vol. 26, no. 6, pp. 909–920, Jan. 2018, doi: 10.3233/THC-181267.

[103] W. Weber and E. Weber, *Mechanik der menschlichen Gehwerkzeuge: Eine anatomisch-physiologische Untersuchung*. Dieterich, 1836.

[104] R. D. Crowninshield and R. A. Brand, “A physiologically based criterion of muscle force prediction in locomotion,” *J. Biomech.*, vol. 14, no. 11, pp. 793–801, Jan. 1981, doi: 10.1016/0021-9290(81)90035-X.

[105] M. Zellmer, T. W. Kernozek, N. Gheidi, J. Hove, and M. Torry, “Patellar tendon stress between two variations of the forward step lunge,” *J. Sport Health Sci.*, vol. 8, no. 3, pp. 235–241, May 2019, doi: 10.1016/j.jshs.2016.12.005.

[106] E. Beaucage-Gauvreau *et al.*, “Validation of an OpenSim full-body model with detailed lumbar spine for estimating lower lumbar spine loads during symmetric and asymmetric lifting tasks,” *Comput. Methods Biomech. Biomed. Engin.*, vol. 22, no. 5, pp. 451–464, Apr. 2019, doi: 10.1080/10255842.2018.1564819.

[107] A. Kian *et al.*, “Static optimization underestimates antagonist muscle activity at the glenohumeral joint: A musculoskeletal modeling study,” *J. Biomech.*, vol. 97, p. 109348, Dec. 2019, doi: 10.1016/j.jbiomech.2019.109348.

[108] E. Forster, U. Simon, P. Augat, and L. Claes, “Extension of a state-of-the-art optimization criterion to predict co-contraction,” *J. Biomech.*, p. 5, 2004.

[109] A. Seireg and R. J. Arvikar, “A mathematical model for evaluation of forces in lower extremeties of the musculo-skeletal system,” *J. Biomech.*, vol. 6, no. 3, pp. 313–326, mai 1973, doi: 10.1016/0021-9290(73)90053-5.

[110] D. D. Penrod, D. T. Davy, and D. P. Singh, “An optimization approach to tendon force analysis,” *J. Biomech.*, vol. 7, no. 2, pp. 123–129, Mar. 1974, doi: 10.1016/0021-9290(74)90050-5.

[111] J. Dul, G. E. Johnson, R. Shiavi, and M. A. Townsend, “Muscular synergism—II. A minimum-fatigue criterion for load sharing between synergistic muscles,” *J. Biomech.*, vol. 17, no. 9, pp. 675–684, Jan. 1984, doi: 10.1016/0021-9290(84)90121-0.

[112] T. Xiao and Y. Fu, “Biomechanical Modeling of Human Body Movement,” *J. Biom. Biostat.*, vol. 7, Jan. 2016, doi: 10.4172/2155-6180.1000309.

[113] G. Paul and S. Wischniewski, “Standardisation of digital human models,” *Ergonomics*, vol. 55, no. 9, pp. 1115–1118, Sep. 2012, doi: 10.1080/00140139.2012.690454.

[114] C.-M. Chang and J. J. P. Tsai, “Ergonomic Designs Based on Musculoskeletal Models,” in *2011 IEEE 11th International Conference on Bioinformatics and Bioengineering*, Oct. 2011, pp. 112–116. doi: 10.1109/BIBE.2011.24.

[115] M. Obentheuer, M. Roller, S. Björkenstam, K. Berns, and J. Linn, “Human like motion generation for ergonomic assessment - a muscle driven Digital Human Model using muscle synergies,” in *Proceedings of the 8th ECCOMAS Thematic Conference on Multibody Dynamics*, Prague, Czech Republic, Jun. 2017, pp. 847–856.

[116] B. A. Slavens and G. F. Harris, “The Biomechanics of Upper Extremity Kinematic and Kinetic Modeling: Applications to Rehabilitation Engineering,” *Crit. Rev. Biomed. Eng.*, vol. 36, no. 2–3, 2008, doi: 10.1615/CritRevBiomedEng.v36.i2-3.20.

[117] G. Chiriatti, G. Palmieri, and M. C. Palpacelli, “Collaborative Robotics for Rehabilitation: A Multibody Model for Kinematic and Dynamic Analysis,” in *Advances in Italian Mechanism Science*, Cham, 2021, pp. 431–438. doi: 10.1007/978-3-030-55807-9_49.

[118] K. A. Inkol, C. Brown, W. McNally, C. Jansen, and J. McPhee, “Muscle torque generators in multibody dynamic simulations of optimal sports performance,” *Multibody Syst. Dyn.*, vol. 50, no. 4, pp. 435–452, Dec. 2020, doi: 10.1007/s11044-020-09747-9.

[119] F. Leboeuf, G. Bessonnet, P. Seguin, and P. Lacouture, “Energetic versus sthenic optimality criteria for gymnastic movement synthesis,” *Multibody Syst. Dyn.*, vol. 16, no. 3, pp. 213–236, Oct. 2006, doi: 10.1007/s11044-006-9024-4.

[120] M. Taylor and P. J. Prendergast, “Four decades of finite element analysis of orthopaedic devices: Where are we now and what are the opportunities?,” *J. Biomech.*, vol. 48, no. 5, pp. 767–778, Mar. 2015, doi: 10.1016/j.jbiomech.2014.12.019.

[121] Q. Zhang, T. Chon, Y. Zhang, J. S. Baker, and Y. Gu, “Finite element analysis of the lumbar spine in adolescent idiopathic scoliosis subjected to different loads,” *Comput. Biol. Med.*, vol. 136, p. 104745, Sep. 2021, doi: 10.1016/j.compbiomed.2021.104745.

[122] D. Benoit, X. Wang, D. G. Crandall, and C.-É. Aubin, “Biomechanical analysis of sagittal correction parameters for surgical instrumentation with pedicle subtraction osteotomy in adult spinal deformity,” *Clin. Biomech. Bristol Avon*, vol. 71, pp. 45–52, Jan. 2020, doi: 10.1016/j.clinbiomech.2019.10.014.

[123] L. Blanchet, “Development of a Procedure to Optimize the Geometric and Dynamic Designs of Assistive Upper Limb Exoskeletons,” masters, Polytechnique Montréal, 2020. Accessed: Mar. 07, 2022. [Online]. Available: https://publications.polymtl.ca/5224/

[124] “Adams - The Multibody Dynamics Simulation Solution.” https://www.mscsoftware.com/product/adams (accessed Aug. 03, 2022).

[125] “Musculoskeletal modeling and simulations with AnyBody.” https://www.anybodytech.com/software/anybodymodelingsystem/ (accessed Aug. 03, 2022).

[126] “MapleSim - Advanced System-Level Modeling & Simulation - Maplesoft.” https://www.maplesoft.com/products/maplesim/ (accessed Aug. 03, 2022).

[127] S. L. Delp *et al.*, “OpenSim: Open-Source Software to Create and Analyze Dynamic Simulations of Movement,” *IEEE Trans. Biomed. Eng.*, vol. 54, no. 11, Art. no. 11, 2007.

[128] M. L. Felis, “RBDL: an efficient rigid-body dynamics library using recursive algorithms,” *Auton Robot*, p. 17, 2017.

[129] N. Docquier, A. Poncelet, and P. Fisette, “ROBOTRAN: a powerful symbolic gnerator of multibody models,” *Mech. Sci.*, vol. 4, no. 1, pp. 199–219, May 2013, doi: 10.5194/ms-4-199-2013.

[130] “Simscape Multibody.” https://www.mathworks.com/products/simscape-multibody.html (accessed Aug. 03, 2022).

[131] A. Sarcher *et al.*, “Impact of muscle activation on ranges of motion during active elbow movement in children with spastic hemiplegic cerebral palsy,” *Clin. Biomech.*, p. 9, 2015.

[132] J.-C. Samin and P. Fisette, *Symbolic Modeling of Multibody Systems*. Springer Netherlands, 2003. doi: 10.1007/978-94-017-0287-4.

[133] B. Michaud, S. Duprey, and M. Begon, “Scapular kinematic reconstruction – segmental optimization, multibody optimization with open-loop or closed-loop chains: which one should be preferred?,” *Int. Biomech.*, vol. 4, no. 2, pp. 86–94, Nov. 2017, doi: 10.1080/23335432.2017.1405741.

[134] A. El Habachi, S. Duprey, L. Cheze, and R. Dumas, “A parallel mechanism of the shoulder—application to multi-body optimisation,” *Multibody Syst Dyn*, vol. 33, pp. 1–13, Apr. 2014, doi: 10.1007/s11044-014-9418-7.

[135] A. Kecskemethy and A. Weinberg, “An Improved Elasto-Kinematic Model of the Human Forearm for Biofidelic Medical Diagnosis,” *Multibody Syst. Dyn.*, vol. 14, pp. 1–21, Aug. 2005, doi: 10.1007/s11044-005-1756-z.

[136] M. Raison, “On the Quantification of Joint and Muscle Efforts in the Human Body During Motion,” Université Catholique de Louvain, Louvain-la-Neuve, Belgique, 2010.

[137] V. Norman-Gerum and J. McPhee, “Comparison of Cylindrical Wrapping Geometries to Via Points for Modeling Muscle Paths in the Estimation of Sit-to-Stand Muscle Forces,” presented at the ASME 2013 International Design Engineering Technical Conferences and Computers and Information in Engineering Conference, Feb. 2014. doi: 10.1115/DETC2013-13437.

[138] P. Favre, C. Gerber, and J. G. Snedeker, “Automated muscle wrapping using finite element contact detection,” *J. Biomech.*, vol. 43, no. 10, pp. 1931–1940, Jul. 2010, doi: 10.1016/j.jbiomech.2010.03.018.

[139] B. A. Garner and M. G. Pandy, “The Obstacle-Set Method for Representing Muscle Paths in Musculoskeletal Models,” *Comput. Methods Biomech. Biomed. Engin.*, vol. 3, no. 1, pp. 1–30, Jan. 2000, doi: 10.1080/10255840008915251.

[140] C. Livet, T. Rouvier, G. Dumont, and C. Pontonnier, “An Automatic and Simplified Approach to Muscle Path Modeling,” *J. Biomech. Eng.*, vol. 144, no. 1, Sep. 2021, doi: 10.1115/1.4051870.

[141] C. L. Dembia, N. A. Bianco, A. Falisse, J. L. Hicks, and S. L. Delp, “OpenSim Moco: Musculoskeletal optimal control,” *PLOS Comput. Biol.*, vol. 16, no. 12, p. e1008493, déc 2020, doi: 10.1371/journal.pcbi.1008493.

[142] A. J. van den Bogert, D. Blana, and D. Heinrich, “Implicit methods for efficient musculoskeletal simulation and optimal control,” *Procedia IUTAM*, vol. 2, pp. 297–316, Jan. 2011, doi: 10.1016/j.piutam.2011.04.027.

[143] R. A. Wehage and E. J. Haug, “Generalized Coordinate Partitioning for Dimension Reduction in Analysis of Constrained Dynamic Systems,” *J. Mech. Des.*, vol. 104, no. 1, pp. 247–255, Jan. 1982, doi: 10.1115/1.3256318.

[144] “EduExo - The Robotic Exoskeleton Kit,” *EduExo*. http://www.eduexo.com/ (accessed Jun. 27, 2022).

[145] D. Galinski, J. Sapin, and B. Dehez, “Optimal design of an alignment-free two-DOF rehabilitation robot for the shoulder complex,” *IEEE Int. Conf. Rehabil. Robot. Proc.*, vol. 2013, p. 6650502, Jun. 2013, doi: 10.1109/ICORR.2013.6650502.

[146] F. Ferrati, R. Bortoletto, and E. Pagello, “Virtual modelling of a real exoskeleton constrained to a human musculoskeletal model,” in *Proceedings of the Second international conference on Biomimetic and Biohybrid Systems*, Berlin, Heidelberg, juillet 2013, pp. 96–107. doi: 10.1007/978-3-642-39802-5_9.

[147] D. Galinski, “Conception et optimisation d’un robot de rééducation neuromotrice du membre supérieur avec compensation active de la gravité,” UCL - Université Catholique de Louvain, 2014. Accessed: Mar. 23, 2022. [Online]. Available: https://dial.uclouvain.be/pr/boreal/fr/object/boreal%3A153440

[148] N. Jarrasse and G. Morel, “Connecting a Human Limb to an Exoskeleton,” *IEEE Trans. Robot.*, vol. 28, no. 3, Art. no. 3, 2012.

[149] M. G. Carmichael and D. K. Liu, “Human Biomechanical Model Based Optimal Design of Assistive Shoulder Exoskeleton,” in *Field and Service Robotics: Results of the 9th International Conference*, L. Mejias, P. Corke, and J. Roberts, Eds. Cham: Springer International Publishing, 2015, pp. 245–258. doi: 10.1007/978-3-319-07488-7_17.

[150] J.-F. Collard, “Geometrical and kinematic optimization of closed-loop multibody systems/Optimisation géométrique et cinématique de systèmes multicorps avec boucles cinématiques,” UCL - Université Catholique de Louvain, 2007. Accessed: Mar. 25, 2022. [Online]. Available: https://dial.uclouvain.be/pr/boreal/object/boreal:5212/

[151] J. Iqbal, N. G. Tsagarakis, and D. G. Caldwell, “A human hand compatible optimised exoskeleton system,” in *2010 IEEE International Conference on Robotics and Biomimetics*, Dec. 2010, pp. 685–690. doi: 10.1109/ROBIO.2010.5723409.

[152] R. P. Matthew, E. J. Mica, W. Meinhold, J. A. Loeza, M. Tomizuka, and R. Bajcsy, “Introduction and initial exploration of an Active/Passive Exoskeleton framework for portable assistance,” in *2015 IEEE/RSJ International Conference on Intelligent Robots and Systems (IROS)*, Sep. 2015, pp. 5351–5356. doi: 10.1109/IROS.2015.7354133.

[153] C. J. Walsh, K. Endo, and H. Herr, “A quasi-passive leg exoskeleton for load-carrying augmentation,” *Int. J. Humanoid Robot.*, vol. 04, no. 03, pp. 487–506, Sep. 2007, doi: 10.1142/S0219843607001126.

[154] D. La Torre, H. Kunze, M. Ruiz-Galan, T. Malik, and S. Marsiglio, “Optimal Control: Theory and Application to Science, Engineering, and Social Sciences,” *Abstr. Appl. Anal.*, vol. 2015, p. e890527, Apr. 2015, doi: 10.1155/2015/890527.

[155] Q. Docquier, O. Brüls, and P. Fisette, “Comparison and Analysis of Multibody Dynamics Formalisms for Solving Optimal Control Problem,” in *IUTAM Symposium on Intelligent Multibody Systems – Dynamics, Control, Simulation*, Cham, 2019, pp. 55–77. doi: 10.1007/978-3-030-00527-6_3.

[156] M. Gerdts, *Optimal Control of ODEs and DAEs*. Walter de Gruyter, 2011.

[157] R. Bellman, “Dynamic Programming,” *Science*, vol. 153, no. 3731, pp. 34–37, Jul. 1966, doi: 10.1126/science.153.3731.34.

[158] C. R. Taylor, *Applications Of Dynamic Programming To Agricultural Decision Problems*. CRC Press, 2019.

[159] L. S. Pontryagin, *Mathematical Theory of Optimal Processes*. CRC Press, 1987.

[160] J. T. Betts, *Practical Methods for Optimal Control Using Nonlinear Programming, Third Edition*. SIAM, 2020.

[161] L. T. Biegler and V. M. Zavala, "Large-scale nonlinear programming using IPOPT: An integrating framework for enterprise-wide dynamic optimization," *Comput. Chem. Eng.*, vol. 33, no. 3, pp. 575–582, Mar. 2009, doi: 10.1016/j.compchemeng.2008.08.006.

[162] D. Kraft, "On Converting Optimal Control Problems into Nonlinear Programming Problems," 1985. doi: 10.1007/978-3-642-82450-0_9.

[163] H. G. Bock and K. J. Plitt, "A Multiple Shooting Algorithm for Direct Solution of Optimal Control Problems*," *IFAC Proc. Vol.*, vol. 17, no. 2, pp. 1603–1608, Jul. 1984, doi: 10.1016/S1474-6670(17)61205-9.

[164] O. von Stryk, "Numerical Solution of Optimal Control Problems by Direct Collocation," in *Optimal Control: Calculus of Variations, Optimal Control Theory and Numerical Methods*, R. Bulirsch, A. Miele, J. Stoer, and K. Well, Eds. Basel: Birkhäuser, 1993, pp. 129–143. doi: 10.1007/978-3-0348-7539-4_10.

[165] M. Diehl, H. G. Bock, H. Diedam, and P.-B. Wieber, "Fast Direct Multiple Shooting Algorithms for Optimal Robot Control," in *Fast Motions in Biomechanics and Robotics*, Heidelberg, Germany: Springer, 2005, pp. 65–93. doi: 10.1007/978-3-540-36119-0_4.

[166] S. Gros and M. Diehl, *Numerical Optimal Control*. 2020.

[167] S. Kameswaran and L. T. Biegler, "Convergence rates for direct transcription of optimal control problems using collocation at Radau points," *Comput. Optim. Appl.*, vol. 41, no. 1, pp. 81–126, Sep. 2008, doi: 10.1007/s10589-007-9098-9.

[168] J. Andersson, J. Åkesson, and M. Diehl, "Dynamic optimization with CasADi," in *2012 IEEE 51st IEEE Conference on Decision and Control (CDC)*, Dec. 2012, pp. 681–686. doi: 10.1109/CDC.2012.6426534.

[169] J. A. E. Andersson, J. Gillis, G. Horn, J. B. Rawlings, and M. Diehl, "CasADi: a software framework for nonlinear optimization and optimal control," *Math. Program. Comput.*, vol. 11, no. 1, pp. 1–36, Mar. 2019, doi: 10.1007/s12532-018-0139-4.

[170] J. S. Arora, "Chapter 18 - Multi-objective Optimum Design Concepts and Methods," in *Introduction to Optimum Design (Fourth Edition)*, J. S. Arora, Ed. Boston: Academic Press, 2017, pp. 771–794. doi: 10.1016/B978-0-12-800806-5.00018-4.

[171] F. Bailly, A. Ceglia, B. Michaud, D. M. Rouleau, and M. Begon, "Real-Time and Dynamically Consistent Estimation of Muscle Forces Using a Moving Horizon EMG-Marker Tracking Algorithm—Application to Upper Limb Biomechanics," *Front. Bioeng. Biotechnol.*, vol. 9, 2021, doi: 10.3389/fbioe.2021.642742.

[172] C. Bélaise, F. Dal Maso, B. Michaud, K. Mombaur, and M. Begon, "An EMG-marker tracking optimisation method for estimating muscle forces," *Multibody Syst. Dyn.*, vol. 42, no. 2, pp. 119–143, Feb. 2018, doi: 10.1007/s11044-017-9587-2.

[173] A. D. Gidley, A. P. Marsh, and B. R. Umberger, “Performance criteria for generating predictive optimal control simulations of bicycle pedaling,” *Comput. Methods Biomech. Biomed. Engin.*, vol. 22, no. 1, pp. 11–20, Jan. 2019, doi: 10.1080/10255842.2018.1522535.

[174] M. Ezati, P. Brown, B. Ghannadi, and J. McPhee, “Comparison of direct collocation optimal control to trajectory optimization for parameter identification of an ellipsoidal foot–ground contact model,” *Multibody Syst. Dyn.*, vol. 49, no. 1, pp. 71–93, May 2020, doi: 10.1007/s11044-020-09731-3.

[175] E. Charbonneau, F. Bailly, and M. Begon, “Optimal forward twisting pike somersault without self-collision,” *Sports Biomech.*, vol. 0, no. 0, pp. 1–18, Mar. 2022, doi: 10.1080/14763141.2022.2052348.

[176] Z. Wahid and N. Nadir, “Improvement of One Factor at a Time Through Design of Experiments.”

[177] R. T. Marler and J. S. Arora, “The weighted sum method for multi-objective optimization: new insights,” *Struct. Multidiscip. Optim.*, vol. 41, no. 6, pp. 853–862, Jun. 2010, doi: 10.1007/s00158-009-0460-7.

[178] M. J. Anderson and P. J. Whitcomb, *RSM Simplified: Optimizing Processes Using Response Surface Methods for Design of Experiments, Second Edition*, 2nd ed. New York: Productivity Press, 2016. doi: 10.1201/9781315382326.

[179] X.-S. Yang, “Chapter 6 - Genetic Algorithms,” in *Nature-Inspired Optimization Algorithms (Second Edition)*, X.-S. Yang, Ed. Academic Press, 2021, pp. 91–100. doi: 10.1016/B978-0-12-821986-7.00013-5.

[180] R. Adhao and V. Pachghare, “Feature selection using principal component analysis and genetic algorithm,” *J. Discrete Math. Sci. Cryptogr.*, vol. 23, no. 2, pp. 595–602, Feb. 2020, doi: 10.1080/09720529.2020.1729507.

[181] N. Gorgolis, I. Hatzilygeroudis, Z. Istenes, and L. – G. Gyenne, “Hyperparameter Optimization of LSTM Network Models through Genetic Algorithm,” in *2019 10th International Conference on Information, Intelligence, Systems and Applications (IISA)*, Jul. 2019, pp. 1–4. doi: 10.1109/IISA.2019.8900675.

[182] S. Mirjalili, J. Song Dong, A. S. Sadiq, and H. Faris, “Genetic Algorithm: Theory, Literature Review, and Application in Image Reconstruction,” in *Nature-Inspired Optimizers: Theories, Literature Reviews and Applications*, S. Mirjalili, J. Song Dong, and A. Lewis, Eds. Cham: Springer International Publishing, 2020, pp. 69–85. doi: 10.1007/978-3-030-12127-3_5.

[183] R. M. Ehrig, W. R. Taylor, G. N. Duda, and M. O. Heller, “A survey of formal methods for determining the centre of rotation of ball joints,” *J. Biomech.*, p. 12, 2006.

[184] R. M. Ehrig, W. R. Taylor, G. N. Duda, and M. O. Heller, “A survey of formal methods for determining functional joint axes,” *J. Biomech.*, p. 8, 2007.

[185] J. Rosen, J. C. Perry, N. Manning, S. Burns, and B. Hannaford, “The human arm kinematics and dynamics during daily activities - toward a 7 DOF upper limb powered exoskeleton,” in *12th International Conference on Advanced Robotics*, Jul. 2005, pp. 532–539. doi: 10.1109/ICAR.2005.1507460.

[186] J. F. O'Brien, R. E. Bodenheimer, G. J. Brostow, and J. K. Hodgins, "Automatic Joint Parameter Estimation from Magnetic Motion Capture Data," Georgia Institute of Technology, Technical Report, 1999. Accessed: Aug. 11, 2021. [Online]. Available: https://smartech.gatech.edu/handle/1853/3408

[187] B. Goislard De Monsabert, D. Edwards, D. Shah, and A. Kedgley, "Importance of Consistent Datasets in Musculoskeletal Modelling: A Study of the Hand and Wrist," *Ann. Biomed. Eng.*, vol. 46, no. 1, pp. 71–85, Jan. 2018, doi: 10.1007/s10439-017-1936-z.

[188] W. M. Murray, T. S. Buchanan, and S. L. Delp, "Scaling of peak moment arms of elbow muscles with upper extremity bone dimensions," *J. Biomech.*, p. 8, 2002.

[189] F. De Groote, A. L. Kinney, A. V. Rao, and B. J. Fregly, "Evaluation of Direct Collocation Optimal Control Problem Formulations for Solving the Muscle Redundancy Problem," *Ann. Biomed. Eng.*, vol. 44, no. 10, pp. 2922–2936, Oct. 2016, doi: 10.1007/s10439-016-1591-9.

[190] K. Ishihara, T. D. Itoh, and J. Morimoto, "Full-Body Optimal Control Toward Versatile and Agile Behaviors in a Humanoid Robot," *IEEE Robot. Autom. Lett.*, vol. 5, no. 1, pp. 119–126, Jan. 2020, doi: 10.1109/LRA.2019.2947001.

[191] B. Michaud, F. Bailly, E. Charbonneau, A. Ceglia, L. Sanchez, and M. Begon, "Bioptim, a Python framework for Musculoskeletal Optimal Control in Biomechanics," *bioRxiv*, p. 2021.02.27.432868, May 2021, doi: 10.1101/2021.02.27.432868.

[192] K. Deb, "Multi-objective Optimisation Using Evolutionary Algorithms: An Introduction," in *Multi-objective Evolutionary Optimisation for Product Design and Manufacturing*, L. Wang, A. H. C. Ng, and K. Deb, Eds. London: Springer, 2011, pp. 3–34. doi: 10.1007/978-0-85729-652-8_1.

[193] S. H. Dhawane, T. Kumar, and G. Halder, "Central composite design approach towards optimization of flamboyant pods derived steam activated carbon for its use as heterogeneous catalyst in transesterification of Hevea brasiliensis oil," *Energy Convers. Manag.*, vol. 100, pp. 277–287, Aug. 2015, doi: 10.1016/j.enconman.2015.04.083.

[194] D. C. Montgomery, *Design and Analysis of Experiments*. John Wiley & Sons, 2017.

[195] S. Lecours, "Développement d'un exosquelette portable motorisé des membres supérieurs pour les enfants atteints de troubles neuromusculaires," masters, Polytechnique Montréal, 2019. Accessed: Mar. 07, 2022. [Online]. Available: https://publications.polymtl.ca/4048/

[196] P. L. Li, "Support à la conception d'exosquelettes motorisés d'assistance du membre supérieur multitâches," masters, Polytechnique Montréal, 2022.

[197] J. Mahmud, C. A. Holt, and S. L. Evans, "An innovative application of a small-scale motion analysis technique to quantify human skin deformation in vivo," *J. Biomech.*, vol. 43, no. 5, pp. 1002–1006, Mar. 2010, doi: 10.1016/j.jbiomech.2009.11.009.

[198] S. Bastide, N. Vignais, F. Geffard, and B. Berret, "Interacting with a 'Transparent' Upper-Limb Exoskeleton: A Human Motor Control Approach," in *2018 IEEE/RSJ International Conference on Intelligent Robots and Systems (IROS)*, Oct. 2018, pp. 4661–4666. doi: 10.1109/IROS.2018.8593991.

[199] Y. Bougrinat, S. Achiche, and M. Raison, “Design and development of a lightweight ankle exoskeleton for human walking augmentation,” *Mechatronics*, vol. 64, p. 102297, Dec. 2019, doi: 10.1016/j.mechatronics.2019.102297.

[200] J. L. Hicks, T. K. Uchida, A. Seth, A. Rajagopal, and S. L. Delp, “Is my model good enough? Best practices for verification and validation of musculoskeletal models and simulations of movement,” *J. Biomech. Eng.*, vol. 137, no. 2, p. 020905, Feb. 2015, doi: 10.1115/1.4029304.

[201] A. Seth *et al.*, “OpenSim: Simulating musculoskeletal dynamics and neuromuscular control to study human and animal movement,” *PLOS Comput. Biol.*, vol. 14, no. 7, p. e1006223, juil 2018, doi: 10.1371/journal.pcbi.1006223.

[202] M. Damsgaard, J. Rasmussen, S. T. Christensen, E. Surma, and M. de Zee, “Analysis of musculoskeletal systems in the AnyBody Modeling System,” *Simul. Model. Pract. Theory*, vol. 14, no. 8, pp. 1100–1111, Nov. 2006, doi: 10.1016/j.simpat.2006.09.001.

[203] Y. Kim, Y. Jung, W. Choi, K. Lee, and S. Koo, “Similarities and differences between musculoskeletal simulations of OpenSim and AnyBody modeling system,” *J. Mech. Sci. Technol.*, vol. 32, no. 12, pp. 6037–6044, Dec. 2018, doi: 10.1007/s12206-018-1154-0.

[204] U. Trinler, H. Schwameder, R. Baker, and N. Alexander, “Muscle force estimation in clinical gait analysis using AnyBody and OpenSim,” *J. Biomech.*, vol. 86, pp. 55–63, Mar. 2019, doi: 10.1016/j.jbiomech.2019.01.045.

[205] G. Kamen and D. A. Gabriel, *Essentials of Electromyography*. Human Kinetics, 2010.

APPENDIX A ELECTROMYOGRAPHY FUNDAMENTALS

This section, based on the book of [205], presents the basic notions in electromyography.

A person's movement intentions are generated in the brain and transferred to the muscles via the nervous system. When a muscle contracts, ions are exchanged between the membranes of the muscle fibres. These are innervated by a motor unit. Each motor unit innervates several muscle fibers. When nerve impulses from the brain reach the motor units, they produce an action potential which propagates in the muscle fibers which causes ion exchanges. The EMG signal measures the action potential of the motor units recruited to produce the contraction. There are two main methods for measuring EMG: intramuscular and surface.

Intramuscular EMG uses needle-shaped electrodes that penetrate the skin to record the electrical signal directly into the muscle tissue. The main advantage of this method is that it makes it possible to record the action potential produced by a single motor unit. Intramuscular EMG is particularly useful for measuring the activity of deep muscles. This method being invasive, it presents a risk of infection and a possibility of loss of mobility due to the electrodes.

Surface EMG is a non-invasive method that uses electrodes placed on the surface of the skin. This method is not able to record an individual action potential, but rather the sum of the action potentials produced by the motor units. Surface EMG is mainly used to measure superficial muscle activity because the signal from deep muscles reaches the surface with a very low amplitude since the muscle tissue attenuates the high frequencies of the signal. In addition, there is a high risk of cross-talk (or cross-talk): the activity of a distant but powerful muscle can propagate through the tissues and add to that of the muscle above which the electrodes. However, it is not possible to isolate the signal specific to each muscle following the recording. To promote comparisons between studies on EMG, the SENIAM project (Surface Electromyography for the Non-Invasive Assessment of Muscles) set up by the European Union has produced an EMG user guide containing recommendations on the skin preparation, electrode placement and signal processing [22].

APPENDIX B HILL-TYPE MODEL FORCE COMPONENTS

Section 2.3.2.2 Muscle contraction dynamics presented the contraction dynamics equation:

$$F(t) = \left(\underbrace{a(t)\tilde{F}_l^{CE}(\tilde{l}_m)\tilde{F}_v^{CE}(\tilde{v}_m)}_{active} + \underbrace{\tilde{F}_l^{PE}(\tilde{l}_m)}_{passive} + \underbrace{b_m\tilde{v}_m}_{damping} \right) \tag{B.1}$$

where:

- $a(t)$ is the muscle activation signal obtained from muscle activation dynamics, a number between 0 and 1.
- $\tilde{F}_l^{CE}(\tilde{l}_m)$, $\tilde{F}_v^{CE}(\tilde{v}_m)$, and $\tilde{F}_l^{PE}(\tilde{l}_m)$ respectively are the *force-length*, *active force-velocity*, and *passive force-length* relations [95]–[97]. The sign ~ above the variables mean that they are normalized, i.e., $\tilde{F}_l^{CE}$, $\tilde{F}_v^{CE}(\tilde{v}_m)$, and $\tilde{F}_l^{PE}(\tilde{l}_m)$ are normalized with respect to F_{max}, the muscle length $\tilde{l}_m$ is normalized with respect to the optimal muscle fiber length L_m^{opt} (from [99], and the muscle velocity $\tilde{v}_m$ is normalized with respect to the muscle maximal contraction velocity v_{max} (from [99]).

The force-length, active force-velocity, and passive force-length relations are defined below.

The force-length relationship $\tilde{F}_l^{CE}$ of the muscle is represented by a Gaussian function [96], [97]:

$$\tilde{F}_l^{CE}(\tilde{l}_m) = e^{-\frac{(\tilde{l}_m-1)^2}{\gamma}} \tag{B.2}$$

where $\tilde{l}_m$ is the normalized muscle fiber length and γ is a shape factor whose role is to approximate the force-length relationship of individual sarcomeres. It is set to 0.45 [97].

The active force-velocity relationship $\tilde{F}_v^{CE}$ of the muscle is represented by the following function [96], [97]:

$$\tilde{F}_v^{CE}(\tilde{v}_m) = -A_f\left(1 + \frac{0.25+0.75a}{\tilde{v}_m}\right) \quad if\ \tilde{F}_v^{CE} \le a\tilde{F}_l^{CE} \tag{B.3}$$

$$\tilde{F}_v^{CE}(\tilde{v}_m) = \frac{\dfrac{\tilde{v}_m(2+2/A_f)\tilde{F}_m^{len}}{(0.25+0.75a)(\tilde{F}_m^{len}-1)} + 1}{\dfrac{\tilde{v}_m\left(2+\dfrac{2}{A_f}\right)}{(0.25+0.75a)(\tilde{F}_m^{len}-1)} + 1} \quad if\ \tilde{F}_v^{CE} > a\tilde{F}_l^{CE} \tag{B.4}$$

where a is the previously computed muscle activation, $\tilde{v}_m$ is the normalized muscle contraction velocity, $\tilde{F}_m^{len}$ is the maximum normalized muscle force achievable when the fiber is lengthening (set to 1.4 for young adults [97]), and A_f is a force-velocity shape factor (set to 0.25 [93]).

Both formulations of $\tilde{F}_v^{CE}$ must be evaluated in a first time. The choice between B.3 and B.4 is made a posteriori by evaluating the inequalities between $\tilde{F}_v^{CE}$ and $a\tilde{F}_l^{CE}$.

The passive force-length relationship $\tilde{F}_l^{PE}$ of the muscle is represented by an exponential function [96], [97]:

$$\tilde{F}_l^{PE}(\tilde{l}_m) = \frac{e^{\frac{k^{PE}(\tilde{l}_m - 1)}{\varepsilon_m^0}} - 1}{e^{k^{PE}} - 1} \tag{B.5}$$

where k^{PE} is a shape factor (set to 5 [97]), and ε_m^0 is the passive muscle strain due to maximum isometric force (set to 0.6 for young adults [97]).

APPENDIX C SPATIAL PARAMETERS OF THE UPPER LIMB MUSCLES

Table C.1 Spatial position of each via-points with respect to its reference bone [99]

Muscle name	Coordinates (m)	Reference bone
Biceps – Long head	(-0.03123, -0.02353, -0.01305)	Scapula
	(-0.02094, -0.01309, -0.00461)	Scapula
	(0.02131, 0.01793, 0.01028)	Humerus
	(0.02378, -0.00511, 0.01201)	Humerus
	(0.01345, -0.02827, 0.00136)	Humerus
	(0.01068, -0.07736, -0.00165)	Humerus
Biceps – Short head	(0.01268, -0.03931, -0.02625)	Scapula
	(0.00093, -0.06704, -0.01593)	Scapula
	(0.01117, -0.07576, -0.01101)	Humerus
Biceps – Distal portion	(0.01703, -0.12125, 0.00024)	Humerus
	(0.0228, -0.1754, -0.0063)	Humerus
	(-0.002, -0.0375, -0.002)	Radius
Brachialis	(0.0068, -0.1739, -0.0036)	Humerus
	(0.01894, -0.20559, -0.01105)	Humerus
	(0.00498, -0.01463, 0.00128)	Ulna
	(-0.0032, -0.0239, 0.0009)	Ulna
Brachioradialis	(-0.0098, -0.19963, 0.00223)	Humerus
	(0.03577, -0.12742, 0.02315)	Radius
	(0.0419, -0.221, 0.0224)	Radius

Table C.1 (continued) Spatial position of each via-points with respect to its reference bone [99]

Muscle name	**Coordinates (m)**	**Reference bone**
Triceps – Long head	(-0.04565, -0.04073, -0.01377)	Scapula
	(-0.02714, -0.11441, -0.00664)	Humerus
Triceps – Lateral head	(-0.00599, -0.12646, -0.00428)	Humerus
	(-0.02344, -0.14528, -0.00928)	Humerus
Triceps – Medial head	(-0.00838, -0.13695, -0.00906)	Humerus
	(-0.02601, -0.15139, -0.0108)	Humerus
Triceps – Distal portion	(-0.03184, -0.22637, -0.01217)	Humerus
	(-0.01743, -0.26757, -0.01208)	Humerus
	(-0.0219, 0.01046, -0.00078)	Ulna

APPENDIX D MUSCULOSKELETAL-EXOSKELETON MULTIBODY MODEL IN ROBOTRAN

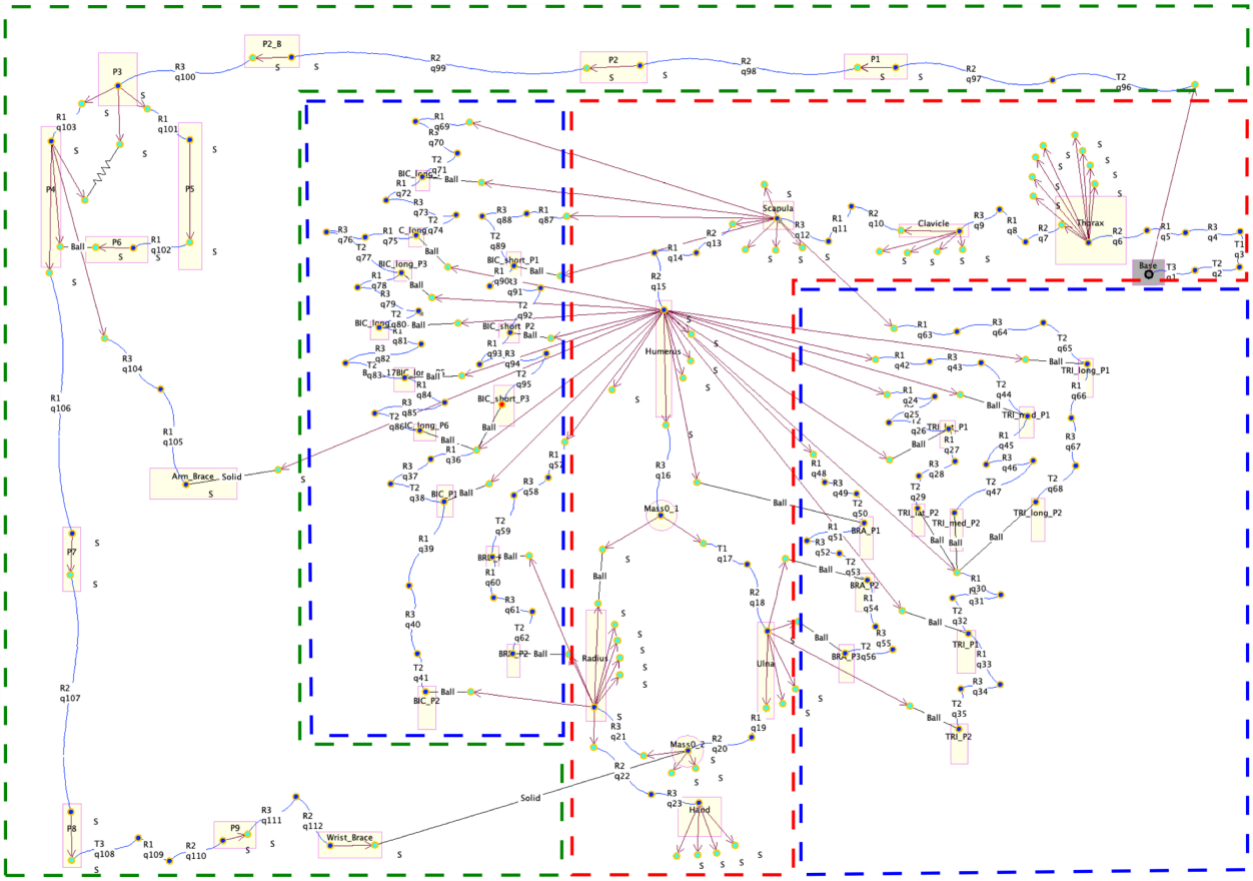

Figure D.1 Complete representation of the musculoskeletal-exoskeleton multibody model in ROBOTRAN graphic pad. The red square denotes the osteoarticular model (AOM) from Laitenberger et al. [27]. The combination of red and blue squares denotes the developed musculoskeletal model in this thesis (AMM). The combination of red, blue, and green squares denotes the complete musculoskeletal-exoskeleton model.